Analysis of Near Relativistic Protons and Electrons in Solar Events

Jorge Bruno Soares de Sousa Morgado

Abril de 2015

Resumo

As medições temporais precisas de Eventos de Partículas Solares (SEP) são cruciais para o estudo dos processos de aceleração envolvidos nos mesmos.

O foco desta pesquisa foi o uso de métodos de Monte Carlo para simular um modelo virtual do Heliosphere Instrument for Spectra, Composition and Anisotropy at Low Energies (HI-SCALE) e do Electron Proton Alpha Monitor (EPAM), dois instrumentos idênticos que fizeram parte de duas missões bastante distintas.

A simulação tomou em conta o ruído electrónico dos electrões permitindo identificar e corrigir significativamente a contaminação de canais de electrões de energia mais baixa por electrões de energias superiores. A simulação permitiu caracterizar protões que entram no instrumento pelo seu revestimento, permitindo extender o alcance nominal dos canais de protões de menos de 5 MeV para mais de 1 GeV.

Analisaram-se dois eventos SEP para validar os métodos propostos na tese para análise de dados do EPAM: Evento de 17/05/2012 onde os dados do Energetic Proton, Electron and Alpha Detector (EPEAD) e da Rede de Monitores de Neutrões (NMN) apresentam uma excelente concordância com os resultados obtidos no EPAM; Evento de 20/01/2005 onde os dados do NMN e o perfil de raios-X moles do flare associado estão também em excelente concordância com os resultados obtidos no EPAM.

Finalmente são discutidos eventos SEP que cumprem com as condições necessárias para poderem ser analisados segundo o método proposto na tese, bem como um instrumento espacial nele baseado capaz de observar protões na gama GeV de energias.

Palavras-chave: Sol: actividade — Sol: coroa solar — Sol: emissão de partículas — detectores: HI-SCALE — detectores: EPAM — detectores: GOES13 — detectores: rede de monitorização de neutrões — detectores: simulações de Monte Carlo — detectores: calibração — emissão de partículas: momento de emissão

Abstract

Accurate timing of Solar Event Particles (SEP) is crucial for understanding the acceleration processes involved in Sun's emission of the charged particles that compose them.

This research focus was to use Monte Carlo methods to simulate a virtual model of the Heliosphere Instrument for Spectra, Composition and Anisotropy at Low Energies (HI-SCALE) and the Electron Proton Alpha Monitor (EPAM), two identical instruments that took part in two vastly distinct missions.

The simulation results with the included electron noise clarified the contamination of the electron lower energy channels by the higher energy ones. Additionally, the simulation results allow for the characterization of protons penetrating trough the instrument casing, increasing the upper nominal energy range of the proton channels from less than 5 MeV to more than 1 GeV.

To validate the methods developed in this work two SEP events were analyzed: The 2012, May 17 event where the data from the Energetic Proton, Electron and Alpha Detector (EPEAD) and the Neutron Monitor Network (NMN) show a close agreement with the results obtained using EPAM data; The 2005, January 20 event where the data from the NMN and the soft X-ray profile for the associated flare also show a close agreement with the results obtained using EPAM data.

Finally were also discussed other SEP events where the conditions are met to use the proposed method as well as discussion of a new space instrument based on this research capable of observing protons in the GeV energy range.

Key words: Sun: activity — Sun: corona — Sun: particle emission — detectors: HI-SCALE — detectors: EPAM — detectors: GOES13 — detectors: neutron monitor network — detectors: Monte Carlo simulations — detectors: calibration — particle emission: onset timing calculation

Acknowledgments

I want to express my gratitude to all the people that have contributed for this work, as well as for those that made it possible for me to achieve this major personal goal. I want to particularly thank the following:

Dr. Patrícia Gonçalves, my thesis supervisor, for getting me started with this project and accompanying me in it.

Dr. Dalmiro Maia, my co-supervisor, for all the help he gave me with the work and with the thesis, for all the invaluable insights he constantly shared about the problem we tried to solve here and for guiding me through the various objectives of this work until it's very final completion. Without him this thesis wouldn't have accomplished its goals.

And finally and foremost to Fernando Morgado and Teresa Morgado, my parents, that were always here for me in every important moment of my life and always supported my aims in life with the utmost patience and the wisest insights.

Contents

Chapter 1

Introduction

Contents

Phenomena associated to solar variability and its effect on Earth are known to mankind since the first humans started to settle at high latitude and were faced with the aurorae. At the time people resorted to mystical explanations of the lights they saw in the night sky. Acknowledgement that the Sun was prone to variability was reached in the early seventeenth century when sunspots were identified as a transient feature on the surface of the Sun, but only much later the eleven year variation in sunspot numbers, the solar cycle, would be discovered (Schwabe, 1843). Correlation between auroral activity and the disruption of electrical equipment was noticed at about the same time (Barlow, 1849). Shortly after, the discovery of solar flares (Carrington, 1863) would mark the beginning of the study of what we now refer to as *space weather*. The link between solar activity, auroral displays and geomagnetism was further developed during the twentieth century with the discovery of the solar wind by the soviet Luna missions (Gringauz et al., 1961) and of coronal mass ejections in observations from OSO-7 (Tousey et al., 1973).

As human technology increases in complexity, accuracy and miniaturization, and in particular with advent of the space age, Earth's space environment plays an ever important role in our daily life. The US National Space Weather Program gives the following definition of Space Weather:

> *"Conditions on the Sun and in the solar wind, magnetosphere, ionosphere and thermosphere that can influence the performance and reliability of space-borne and ground-based technological systems and can endanger human life or health."*

For a very detailed review on space weather and its impact on human technological systems see Lanzerotti (2001).

The range of solar activity and its associated potential space weather effects extends quite far from the Earth orbit. The continuous stream of plasma and magnetic fields flowing from the Sun associated with the solar wind, carves a bubble-like structure in the local interstellar medium, the Heliosphere. On 1977 September 5 NASA started the Voyager program with the objective to study the outer solar system, including the outer reaches of the solar wind. During the last decade the two Voyager probes finally reached the boundaries of the heliosphere and in 2012 August 25 Voyager 1 crossed into interstellar space (Burlaga et al., 2013).

The heliosphere is populated by energetic charged particles of various origins. Among these particles, Galactic Cosmic Radiation (GCR) originating from outside of the solar system and Solar Energetic Particle (SEP) events accelerated at processes near the surface of the Sun, are particularly relevant for the purpose of space weather analysis. Both of these particle populations are affected by solar activity: the intensity of GCR peaks during solar minimum and drops during solar maximum, while SEPs are more common and more intense during the maximum of solar activity and in the drop from solar maximum to solar minimum.

A particular concern addressed in recent times relates to constraints that both GCR and SEP pose to prospective manned missions to Mars. McKenna-Lawlor et al. (2012) using ESA's Mars Energetic Radiation Environment Models were able to compute the radiation doses due to GCR for the cruise phase to and from the planet and for a short surface stay on Mars surface. McKenna-Lawlor et al. (2012) show that the cumulative effects of GCR pose a significant radiation problem during the cruise phase and that career limit values currently adopted by ESA for space personnel would be approached. By using in-flight data from the Earth to Mars, Hassler et al. (2014) show that if conditions measured in the flight a mission to and from Mars could be within limits imposed by NASA. Even if we remain within the confines of the GCR flux levels measured for the last solar cycles, as discussed in McKenna-Lawlor et al. (2012), the real issue is that of solar energetic particle events: a particularly catastrophic SEP could deliver a lethal dose of radiation to the human crew. SEPs of this magnitude are rare but they are not currently predictable: although SEPs are more likely to occur around solar maximum it cannot be assumed that SEPs will not occur under solar minimum conditions. McKenna-Lawlor et al. (2012) end by acknowledging that for a maned mission to mars the health problem posed by energetic particle radiation is presently unresolved.

The radiation environment due to SEPs is thus one of the factors relevant for political deciders addressing the issue if we again start a space-manned program, or if we restrict planetary exploration to robotic probes. Besides this practical aspect, SEP events are an important area of research in Heliophysics because of the insight they provide about the mechanisms behind energy release back at the Sun. This thesis work will center itself on how SEP data can be used to answer the question on how and where the energetic particles of solar origin are accelerated. We will show that the highest energy part of the solar particle spectrum can be analyzed by better understanding the response of radiation detectors to SEP events and that there is a previously unexplored source of valuable high-energy ion data in missions like ACE and Ulysses.

1.1 Basic features of space plasmas

The solar corona is a magnetized plasma characterized by a relatively large temperature (about 10^6 K). The exact nature of the heating process and the details leading to the generation of the magnetic field are still active research subjects. As shown by Parker (1958) hot coronae generate out flowing solar winds, which are the main feature of the space plasma in the solar system. The aim of this section is to outline some of the physical concepts that are relevant for space plasmas, including those in the corona and the interplanetary medium. The associated quantitative theory is somewhat formidable and would require a level of detail that is not needed for the goals of this thesis. So we will emphasize qualitative interpretations.

1.1.1 Continuous approximation for the plasma

When dealing with spatial scales above a few cm in the photosphere, and above a few km in the corona, it is often convenient to use a continuous approximation for the plasma, that can then be described quantitatively by the equations of magnetohydrodynamics (MHD). We will focus only a few points of MHD that allow a characterization of the corona and the interplanetary medium, for a detailed review of MHD in a coronal context see for example Priest (1982).

For our qualitative purposes the most important aspect of MHD arises from to the induction equation, which links the evolution of the magnetic field to the plasma:

$$\frac{\partial \vec{B}}{\partial t} = \nabla \times (\vec{V} \times \vec{B}) + \eta \nabla^2 \vec{B} \tag{1.1}$$

where $\vec{B}$ is the magnetic field, t is the time, $\vec{V}$ is the plasma velocity, and η is the magnetic diffusivity. The two terms on the right side of equation 1.1 have a relatively straightforward interpretation: the first term represents the carrying of field with the plasma (advection) while the second term describes slippage of field through the plasma (diffusion).

The order of magnitude of the terms in equation 1.1 can be inferred from the typical length scales and velocities for the corona:

$$l_0 \approx 10^6 \text{ to } 10^7 \text{m} \tag{1.2}$$

$$\eta \approx 1 \text{ m s}^{-1} \tag{1.3}$$

$$V_0 \approx 10^2 \text{ to } 10^5 \text{m s}^{-1} \tag{1.4}$$

We can thus compute the typical diffusion timescale for the corona by considering only the diffusion term:

$$\frac{\partial \vec{B}}{\partial t} = \eta \nabla^2 \vec{B} \tag{1.5}$$

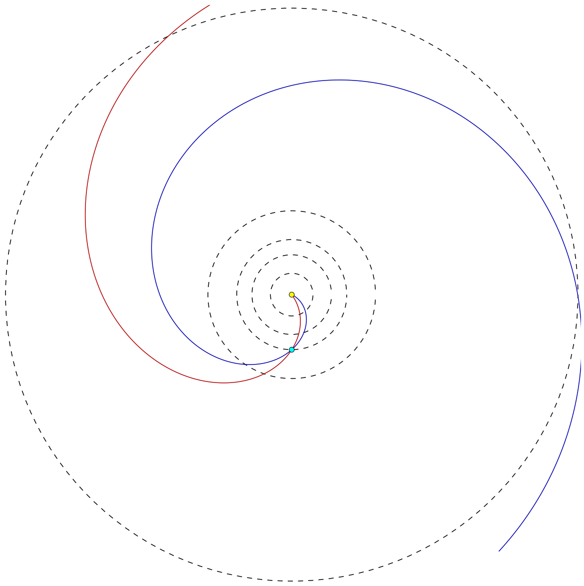

Figure 1.1: Spiral path corresponding to magnetic field lines anchored at the Sun for solar wind speeds of 700 km s^{-1} (red line) and 400 km s^{-1} (blue line). The dashed lines indicate the orbits of the planets (from Mercury to Jupiter); the yellow dot marks the position of the Sun and the cyan dot the position of the Earth.

Approximating the diffusion timescale as $\tau = l^2/\eta$ and using the typical coronal values one retrieves $\tau \approx 32000$ years. This time is obviously much larger than the characteristic times associated to solar activity.

The fact that advection is the relevant term in most of the corona can further be seen by computing the ratio of the advection and diffusion terms. This dimensionless quantity called the magnetic Reynolds number, $R_m = l_0\, V_0/\eta$, is a number somewhere in the range from 10^8 to 10^{12}. This huge number means that the evolution of coronal magnetic fields is clearly linked to the plasma: in the corona advection is clearly dominant and the field is said to be *frozen in the plasma*.

1.1.2 The structure of the interplanetary magnetic field

Why is the assumption of "*field frozen in the plasma*" so important for studying coronal magnetic fields? The very high coronal temperatures, in excess of 10^6 K, mean that the thermal broadening does not allow for the use of the Zeeman effect to retrieve magnetic field information as one does for example in the photosphere. What is traditionally done is to retrieve the shape of the magnetic fields from the shape of the associated plasma structures and model the magnetic field strength by extrapolation of photospheric measures. Reliable magnetic field reconstruction remains a major problem in solar physics. The field frozen in the plasma assumption allows us in particular to infer the structure of the interplanetary magnetic fields.

In the absence of large-scale disturbances, like the sudden expulsion of large volumes of plasma resulting from solar activity and its associated shocks, the plasmas in the interplanetary medium are dominated by the contribution from the steady solar wind flow. Being "frozen" in the plasma, the solar wind magnetic field is thus carried by the solar wind flow. This means that the magnetic field lines connecting to a given source region on the Sun will have a shape which results both from the radial outward motion of the solar wind and from the rotation of the Sun. Assuming a constant speed at the source the expected shape of the magnetic field in the interplanetary medium is that of an archimedian spiral for a source at the equator. The more general shape, when the other latitudes are considered, will be cone-like but in what follows we will still refer to those as spirals.

The length of the spiral at a radial distance R from the Sun center can be computed from the formula:

$$l = \frac{R\varphi\sqrt{1+R^2\varphi^2} + \log(R\varphi + \sqrt{1+R^2\varphi^2})}{2\varphi} \tag{1.6}$$

where $\varphi = \Omega\cos(lat)/v_{sw}$, with lat being the heliographic latitude of the solar wind source, Ω the solar rotation angular velocity and v_{sw} the solar wind speed. The length of the spiral depends thus on the solar wind speed, which varies depending on its source back on the Sun.

There are two characteristic regimes of solar wind: (i) the fast solar wind with speed in excess of 700 km s^{-1}, associated with features known as coronal holes and (ii) the so called slow solar wind with typical velocity about 300-400 km s^{-1}, originating over hotter denser regions in the corona characterized by closed loop systems. Figure 1.1 illustrates two spirals for fast and slow solar wind. At the Earth orbit there is already a significant departure from a radial direction; the spiral length at the Earth is 1.06 AU for the 700 km s^{-1} wind and 1.17 AU for the 400 km s^{-1} wind. Further away from the Sun, for example at Jupiter's orbit (5.2 AU), the effect of solar rotation is much more marked than at Earth's orbit. The length of the field line at a radial distance of 5.2 AU from Sun center is 10.3 AU for the 700 km s^{-1} wind and 16.0 AU for the 400 km s^{-1} wind.

The overall interplanetary magnetic field will result from the interaction between solar wind streams originating from source regions with different characteristics, and the mergers and interactions between streams with different velocities make the overall picture much complex. The 700 km s^{-1} spiral in figure 1.1 originates from a solar source region trailing the source of the 400 km s^{-1} wind, but the spiral from that fast wind stream overcomes the slow wind stream close to the Earth orbit. When such a configuration occurs in the interplanetary medium, the fast wind will interact with the slow wind, forming what is known as a corotating interaction region (CIR). Corotating means that the features corotate with the Sun and reaper periodically, or at least endure for a significant fraction of a solar rotation. CIRs are the dominant large-scale structure in the heliosphere during the minimum phase of solar activity cycle, when coronal holes may extend to near equatorial regions. These features are easily identified in in-situ plasma data: they are bounded by a pair of shocks (forward and reverse) and a stream interface develops within the CIR. Besides their role in the structure of the heliosphere, corotating streams are also important because of their role as drivers of geomagnetic disturbances (Tsurutani et al., 2006). For an exhaustive review on CIRs see the papers in Balogh et al. (1999) and references therein.

1.1.3 Properties of Waves in Plasmas

Although a fluid description for the coronal plasma is suited for many purposes, a major part of modern plasma physics is concerned with the generation of waves and the effects of wave-particle and wave-wave interactions. Turbulence in space plasmas, in particular those in the solar corona and the interplanetary medium, is fundamentally distinct from the familiar macroturbulence of fluids. Space plasmas are tenuous, they are so hot and the density levels are so low that charged particle Coulomb collisions produce negligible thermalization or dissipation on scales less than 0.1 AU. Collisions between particles do not play a central role in the underlying physical processes, hence space plasmas are often described as being collisionless. Despite this fundamental difference processes usually described as collisional in fluids also happen in collisionless plasmas. As an example, shocks still develop in space plasmas but the irreversible plasma heating within these features is accomplished by wave-particle interactions driven by plasma instabilities. A full discussion of turbulence in the solar wind is outside the scope of this thesis, for a detailed discussion see for example Melrose (1980). We will briefly address only a few relevant wave modes and highlight some observational aspects linked to particle propagation.

Central to the concept of wave-particle interaction is the concept of Landau resonance. When particles travel with a velocity v close to the phase velocity of a wave of frequency ω, that is $v \approx w/k$, where k is the wave number, they 'resonate' with the wave. Resonant particles travel along at almost the same speed as the wave and tend to see a relatively static electric field, rather than a rapidly fluctuating one. They can, therefore, exchange energy very effectively with the wave.

When the perturbation is of very small amplitude it can be treated using a set of linear equations, but often the perturbation can increase substantially above its initial value and the linear approximation is not suited since it would predict an increase without limit. This means that some nonlinear effects must arise in the plasma that lead to some sort of saturation of the instability. These nonlinear effects can generally be divided into two categories of mechanisms: (i) quasi-linear theory which studies the interaction between the waves and the electrons and the ions, (ii) mode coupling which involves wave-wave interactions.

Work by Tonks and Langmuir in the 1920s identified three wave modes in an electron ion plasma with Maxwellian velocity distributions and no ambient magnetic field. The first mode is associated with transverse electromagnetic waves. The other two modes are longitudinal (electrostatic).

One of the transverse modes, called the Langmuir mode, is associated with oscillations of the electrons only and the waves associated with it are called Langmuir waves. The important parameter to characterize this mode is the plasma frequency ω_p:

$$\omega_p = \sqrt{\frac{n_e\, e^2}{m_e\, \epsilon_0}} \tag{1.7}$$

where n_e is the number density of electrons, e is the elementary electric charge, m_e is the mass of the electron, and ϵ_0 is the permittivity of free space.

The other electrostatic wave mode identified by Tonks and Langmuir is linked to oscillations of both electrons and ions, it is the ion acoustic mode; the waves associated with it are called ion sound waves. The phase speed of these waves is the sound or 'ion acoustic speed.'

Electromagnetic waves are particularly important since unlike the Langmuir waves

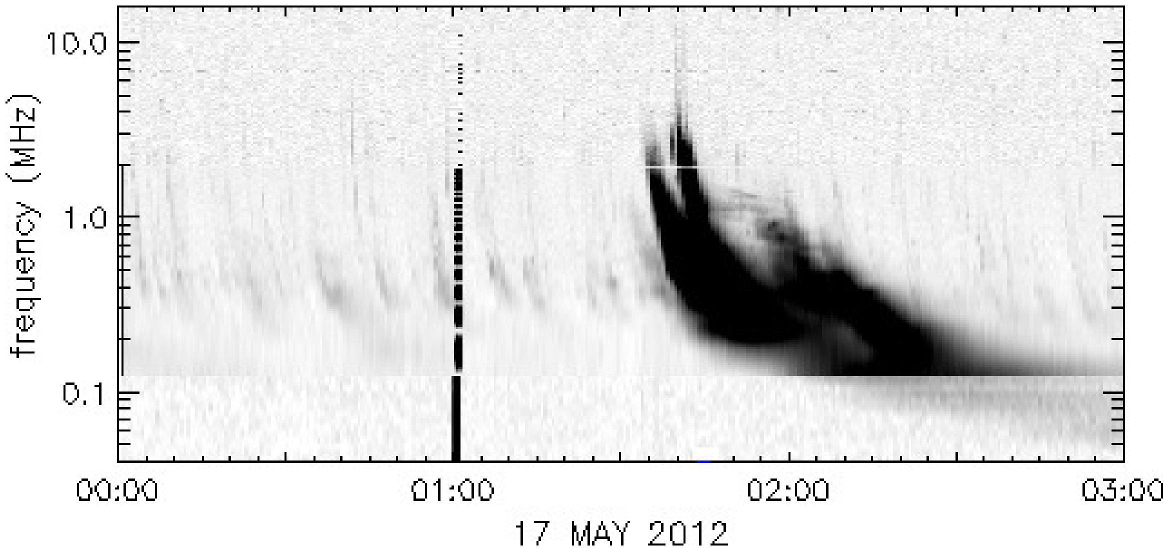

Figure 1.2: Radio dynamical spectra showing the occurrence of type III radio bursts, the signature of an outward moving electron beam.

they can escape from the plasma and be detected by a remote observer. The refractive index n for the transverse mode is given by:

$$n^2 = 1 - \frac{\omega_p^2}{\omega^2} \tag{1.8}$$

From this relation we see that transverse waves in a plasma can only propagate at frequencies above the plasma frequency. The plasma frequency works thus as a cutoff frequency. The fact that the index of refraction depends on the density means also that the trajectory of these waves will bend responding to the density gradients in the plasma; in the corona this is particularly important at radio frequencies below 200 MHz.

Passage of a disturbance, like an electron beam, excites microturbulence at the Langmuir mode. Coalescence of Langmuir waves with ion sound waves through mode coupling can then produce transverse waves with frequencies slightly above the plasma frequency; those waves can they propagate into regions of lower density and reach a remote observer. Since the plasma frequency is proportional to the square root of the density, the progression of a beam leaving the Sun can then be tracked by emission at progressively lower frequencies. Such kind of emissions in the corona and in the interplanetary medium are indeed observed at radio wavelengths and are known as type III radio bursts (Wild and McCready, 1950) being attributed to electron beams with velocities around one third the speed of light. A characteristic spectrum is shown in figure 1.2, observed on 2012 May 17; related to the event that will be the main focus of this thesis. The dynamic spectra in figure 1.2 tracks the progression of electrons accelerated low in the corona as they propagate outward into the interplanetary medium.

The theory of electron beam propagation for a long time concentrated on what is known as Sturrock's Dilemma: on the one hand the predicted evolution of Langmuir turbulence was such that an electron beam in a homogeneous corona should only be able to travel distances on the order of meters (Sturrock, 1964), while on the other hand observations from type III bursts provided clear evidence that the source region propagates at almost constant velocity from the inner corona to several AU, that is, the beam must propagate essentially unaffected. The theories solving this dilemma are somewhat esoteric involving processes like soliton collapse and are outside the scope of this thesis; for an overview see Goldman (1983) and the more recent self consistent type III burst models offering quantitative predictions of Mel'Nik and Kontar (2003). Despite all the complexity of the theory the important feature to retain is that, although electrons do form a plasma-beam structure, and electron motions are indeed perturbed by the Langmuir waves, the electron beam is not significantly decelerated.

The presence of a magnetic field introduces a few more modes and waves; including shear Alfvén waves, magnetosonic waves, and other waves associated with ion cyclotron and lower hybrid resonances. The motion of a particle in a uniform magnetic field will be a cylindrical helix and as such the particle velocity can be described by considering a component parallel to the magnetic field and a component undergoing a circular motion at right angles to the magnetic field. It is the projection of the particle's velocity along the magnetic field direction that is relevant for the progression of the particle along the magnetic field. The important quantity characterizing this component is the angle between the velocity and magnetic field direction, the so called pitch angle of the particle. Interaction of particles with waves in a magnetized medium can be thought of as both a spatial diffusion process (pitch angle scattering) and diffusion in momentum space (stochastic acceleration).

The two relevant magnetohydrodynamic modes leading to pitch angle scattering and momentum diffusion are Alfvén waves and the fast magnetosonic waves. The Alfvénic fluctuations are the most common, do not involve significant variations in the magnitude of the magnetic field strength, propagate only in the direction of the magnetic field and oscillate perpendicular to it, that is, they are shear waves. Magnetosonic waves have a compressive magnetic field component for oblique propagation, present smaller amplitudes and involve significant magnetic field magnitude variations.

For fast magnetosonic waves the Landau resonance discussed above is possible. This mechanism is sometimes known as Fermi second order acceleration, or transit time damping, and its net effect is a significant diffusion in momentum space even in the absence of significant pitch angle scattering. This means that fast magnetosonic waves have considerable acceleration capability.

Interaction between particles and Alvén waves of frequency ω occurs if the gyroresonant condition:

$$\omega - k_{\|} v_{\|} = n\Omega_e \tag{1.9}$$

with the non-zero integer n is fulfilled. In equation 1.9 $v_{\|}$ is the projection of the velocity along the magnetic field direction, $k_{\|}$ is the wave number parallel to the magnetic field, and $\Omega_e = e\,B/m_e\,c$ is the electron cyclotron frequency. The net acceleration from shear Alfvén waves is extremely small and it is unlikely to be important for the acceleration of particles in the inner heliosphere.

1.2 Transient Solar Phenomena

Magnetically closed coronal structures on the Sun, like loops and arcades of loops, are remarkably stable and can persist for long periods of time. Stable does not mean that these structures are static, but that the shear and twisting motions involved in the exchange of energy and mass occur at only a small fraction of the characteristic coronal speeds and thus magnetic structures have the time to adjust to perturbations. But this quasi-static build up of energy can only be maintained up to a certain point, and eventually a state is reached where the corona needs to "*shed*" energy in processes that break the frozen in the field assumption. Although for most of the coronal volume — and also in the heliosphere — conditions are such the field is carried in the plasma, in some very localized regions where the magnetic field changes considerably over very short length scales and where $B \approx 0$ we can have a magnetic Reynolds number $R_m \approx 1$ and those sites are very important for magnetic energy release. Those places are called *current sheets*. Dungey (1953) was the first to propose a scenario where lines of force can be broken and rejoined in current sheets. Dungey also coined the term used to describe the process: *magnetic reconnection* (Dungey, 1958). Magnetic reconnection is widely accepted as being a process which releases magnetic energy

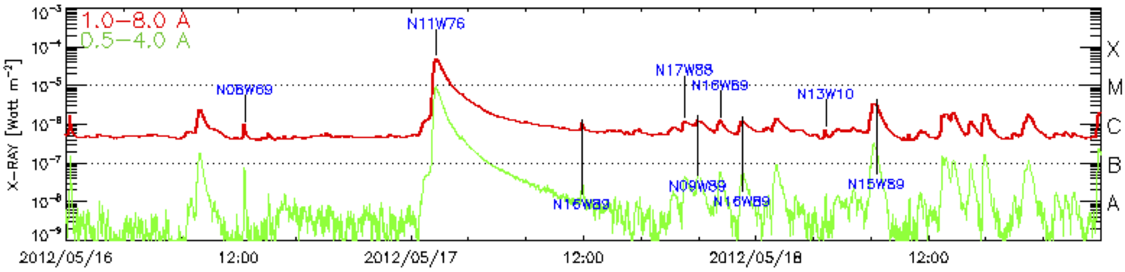

Figure 1.3: GOES soft x-ray plot for the period from 16 to 18 May 2012, showing the occurrence of a series of flarings. The right hand scale shows the flux levels that characterize the so called GOES flare class (from A to X).

heating the plasma, accelerating particles, and generating shock waves.

There are two major eruptive phenomena on the Sun: coronal mass ejections (CMEs) and flares. Although the energy involved in CMEs and flares is of the same order of magnitude, up to 10^{32} erg, they are very different phenomena. Whereas most of the energy in flares is eventually thermalized, the CME produces mainly ordered, macroscopic bulk motions of plasma and magnetic fields. In this section we do not aim at completeness, we just highlight some of the major features of solar transient phenomena.

1.2.1 Flares

Like many other solar phenomena flares are defined mostly by specific observational signatures, there is still no standard model for the physical processes completely in accordance with the observations. A flare is a compact localized brightening of the Sun linked to an explosive release of energy from an active region, with the plasma reaching extremes values in temperature, sometimes about 10^8 K. Flares on the surface of the Sun are a very common occurrence: tens of thousands are observed per solar cycle. Originally flares were studied in the Hα line, which originates in the chromosphere, and they were defined as a sudden localized increase in Hα line brightness linked to magnetic active regions, but for the last three solar cycles solar flares have routinely been observed in hard X-rays and γ-rays and there are classification schemes that take into consideration the flux measured in those bands.

The hard X-ray and γ-ray emissions themselves carry a very small fraction of the total energy involved in the flare (about 10^{-4}), they are nonetheless invaluable since they provide quantitative diagnostics on electron and ion energy spectra, numbers and energy contents.

The GOES soft X-ray flare class from A (less important) to X (more intense), with sub classes from 1 to 9, is a commonly used classification scheme used for flare classification. It is illustrated in Figure 1.3. The change in each rank of importance reflects a change by a factor of 10 in the flux measured in the wavelength interval from 1 to 8 Å.

Modern flare science is also supported by imaging observations in EUV, microwave and radio wavelength bands; nearly the whole spectrum can be sampled during the most recent flare observations. In a way this wealth of observations poses some hurdles for theoretical models: no model has been able to describe all aspects of flare development, nor to explain the energy budget over the broad range of wavelengths where flares can be observed. It is generally assumed the magnetic reconnection of some sort is responsible for the release of magnetic energy, and there is compelling evidence for restructuring of magnetic fields. The exact nature of the trigger mechanism at the origin of the reconnection process and in what way a very significant part of the energy is transferred into non-thermal charged particles present the biggest theoretical challenges. For a recent review of flares in the context of particle acceleration see Vilmer (2012) and references therein.

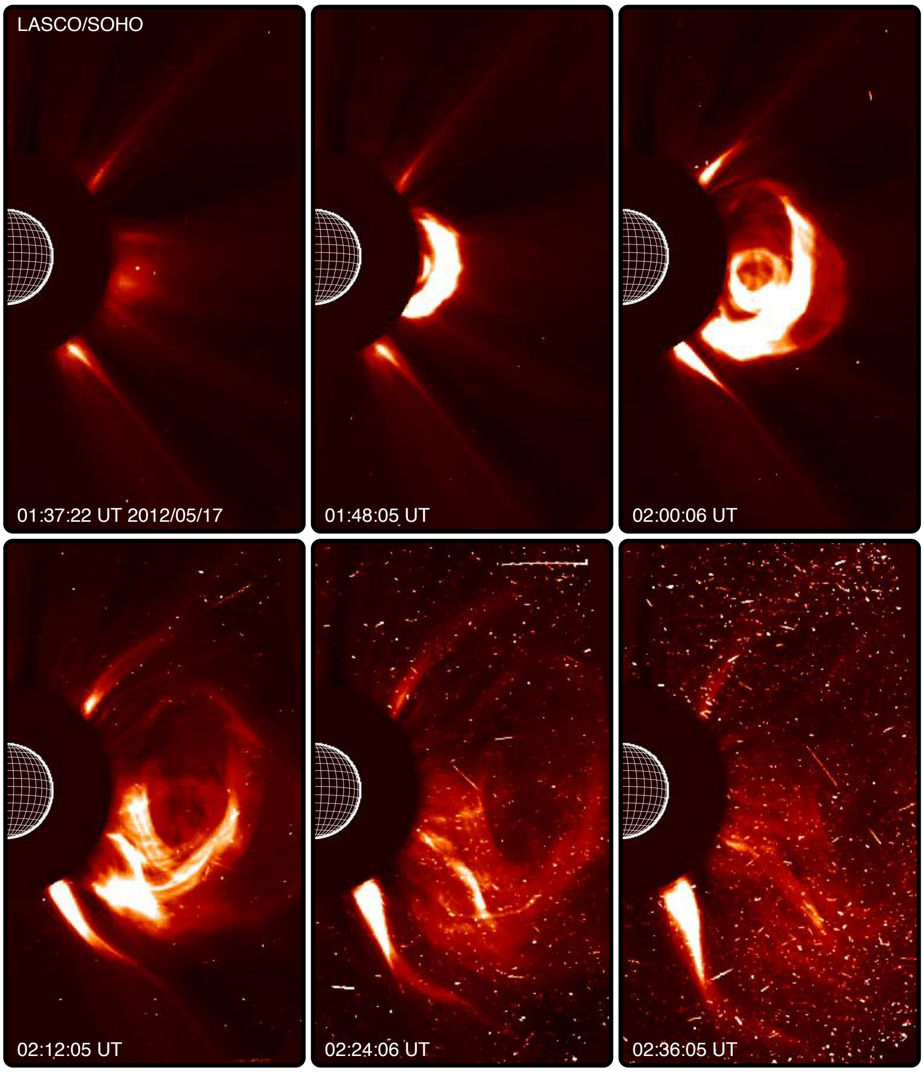

Figure 1.4: LASCO coronagraph images showing the progression of a fast coronal mass ejection on 2012 May 17. The "snow" seen in the latest frames is due to energetic protons impacting the CCD.

1.2.2 Coronal mass ejections

Coronal mass ejections (CMEs) are the white light signatures associated with the release of large volumes of plasma and magnetic fields from the Sun. The average mass of the plasma carried by a CME is about 2×10^{15} g and the velocities of the bulk plasma flow can vary from the events where the CME is slowly accelerated to the solar wind speed to extreme events with velocities that can approach 3000 km per second very low in the corona. White-light coronographic observations show a wealth of different morphologies, with CMEs ranging from amorphous blobs, to simple narrow jet-like features, up to highly structured and complicated entities. CMEs are the most important driver of space weather and during solar maximum they can occur several times per day. For a review of their properties see Schwenn et al. (2006).

There are many phenomena commonly seen in temporal association with CMEs, like flares, filament eruptions, Moreton waves and radio bursts. Understanding the relationship between what is seen from the different observations is not easy, in particular due to the fact that the CME development encompasses a large range of spatial scales, in a relatively short period of time. These phenomena go from the very small as the scales at which magnetic reconnection occurs (current sheet) to the very big as the transient seen in white-light (that can exceed more than 100 degrees over the limb of the Sun in angular extent) in a question of minutes. For an overview of the various phenomena seen in association with CMEs in a wide range of wavelengths see Pick et al. (2006).

The fastest CMEs will plug into the solar wind at speeds which can vastly exceed the characteristic magnetosonic velocities of the wind and as such a fast CME will drive a collisionless shock ahead of it. Although very close to the Sun there is some controversy whether the shock signatures are linked to the CME or to the flare (see

Cliver et al., 1999, and references therein) the density enhancements due to the CME driven shocks were reliably identified in white light images (Vourlidas et al., 2003). In the interplanetary medium the association between shocks and CMEs is well established from both in situ and remote observations (Reiner and Kaiser, 1999). CME driven shocks are particularly relevant for space weather due to their interaction with the Earth magnetosphere originating geomagnetic storms (Gopalswamy et al., 2015, 2007) and also for their role in Galactic Cosmic Ray modulation (Lara et al., 2005).

Fast CMEs are also a "required" companion phenomenon for the most intense SEP events (Gopalswamy et al., 2004, 2003). Quite often the SEP occurrence can be inferred directly from the white light coronographic images. Figure 1.4 shows observations, on 2012 May 17, of a CME made by the Large Angle Spectroscopic Coronagraph (LASCO) experiment (Brueckner et al., 1995) on the Solar and Heliospheric Observatory (SOHO) spacecraft (Domingo et al., 1995). This is a reasonably fast CME, with a velocity in the plane of the sky about 1600 km s^{-1} and the associated SEP event will be the main focus of this thesis. As seen in the latest frames in figure 1.4 the images become noisy and many of the pixels are saturated by bright streaks. This snowy LASCO pictures are in indication that the SOHO spacecraft is crossing a region of space being affected by a SEP event, with energetic ions hitting the CCD detectors in the LASCO coronagraphs.

From the point of view of particle acceleration in association with CMEs there are two aspects worth mentioning. One that is often overlooked is that in the restructuring region behind the CME there are multiple sites of particle acceleration, and their progression tracks very closely the CME development both spatially and temporally (Pohjolainen et al., 2001; Maia et al., 1999, 2003; Klein et al., 2014). The aspect that is highlighted most of the time, to the exclusion of other mechanisms, is the possible role of the CME driven shock. From in-situ measures in the interplanetary space we know that CME-driven shocks accelerate ions to a few MeV energies and electrons to tens of keV and the assumption is that CME driven shocks are much more efficient closer to the Sun, where they are supposed to be able to accelerate electrons to MeV and ions to GeV energies (Reames, 1999).

1.3 Solar energetic particles

Particle telescopes on board spacecraft readily detect sudden enhancements of charged particle fluxes that can last for several hours of even days. With rise times on scales of minutes to an hour, these events present characteristics consistent with a solar origin: (i) the enhancements in particle fluxes often show dispersion in the arrival times with energy (the higher energies are detected first) and (ii) the particle distributions at a given energy tend to be considerably anisotropic close to their onsets, with the particle flux being higher for directions corresponding to the solar direction. These particle enhancements are thus called Solar Energetic Particle (SEP) events and are an indication that there are energetic processes taking place on the Sun capable of accelerating electrons up to hundreds of MeV and ions to more than 10 GeV, and that those particles can escape from their acceleration sites into the interplanetary medium.

Due to their space weather effects high energy protons are of particular interest, and protons from SEP events have been measured in situ with energies up to 100 MeV per nucleon by a fleet of spacecraft (ACE, SOHO, STEREO, Ulysses, Wind, etc.) while the more energetic protons (above 450 MeV) are mostly measured at Earth by neutron monitors on the ground. Despite this wealth of data spanning many decades of active research many basic questions regarding SEPs are still unswered, in particular the aspects relating to source regions and details of the acceleration mechanisms. SEPs are often detected in the aftermath of the two major solar phenomena, solar flares and coronal mass ejections but the exact relation between SEPs, flares and CMEs remains elusive and relies mostly on statisticall associations.

Electromagnetic emissions in radio, X-ray and gamma-ray wavelengths which are produced by particle interaction in the solar atmosphere during flares provide useful diagnostics on the presence of high energy electrons and ions, their composition, spectra and relative abundances; for a detailed review on these processes see (Vilmer, 2012). Assuming an association of SEPS with solar flares might thus seem intuitive and relatively straightforward. Solar Energetic Particle events were initially separated in two types as proposed by Cane et al. (1986): impulsive events of relatively short duration (less than one day) and gradual events of longer duration (days). Figure 1.5 shows a comparison between particle intensities over time for a typical *impulsive* and typical *gradual* SEP event. This nomenclature mimics the classification of flares based on the assciated soft X-ray emissions, but the terminology may be somewhat misleading in particular because it evolved with time. Cane et al. (1986) and later on there was a shift in the definition of impulsive event as a synonymous of ^{3}He-rich event (Reames, 1993, 1999).

Although earlier work, in particular before the discovery of CMEs, assumed a cause and effect relation between flares and SEP events, following the so called "solar flare myth" (Gosling, 1993) this association was essentially abandoned and a cause and effect relation with CME driven shocks became the current paradigm. The association of SEPs with coronal mass ejections is more indirect the the purported association with flares, since the defining signature of a CME is related to bulk motion of plasma, and not the result of energetic particle interaction within the underlying plasma and magnetic field structure. A large scale and fast CME must nonetheless be accompanied by two features relevant for particle association: (i) major restructuring of the corona in the aftermath of the eruption, (ii) a shock wave driven by the outward movement of the CME leading edge plowing through the solar wind at super-alfvenic speeds. Evidence for the former is given for example in radio images of the early phases of the CME (maia et al 1998, maia et al 2003, etc) but it is the later that is the feature that is linked to SEP to the exclusion of all other solar phenomena. The proposed classification scheme of impulsive and gradual SEPs was maintained but the underlying assumption was that there were two differing source regions, one that might be associated with flares and another arising only from CME driven shocks.

Within of the framework of the current paradigm, *Impulsive* SEP are those which exhibit abundances enriched in heavy ions and an isotopically anomaly of highly enriched ^{3}He where the ratio ^{3}He/^{4}He can approach unity, whereas in the solar wind this ratio is ~ 0.0005. (Reames et al., 1994). The standard explanation for *impulsive* SEP events is that the particles from a flare-heated plasma escape after acceleration by the same mechanism that produces the flare. *Gradual* SEP events composition and ionization states resemble that of the corona (from 1×10^6K to 2×10^6K) and that of the solar wind (Reames, 2002). The ratio ^{3}He/^{4}He is very low and also energetic electron abundances are much inferior to those of protons (Ryan et al. (2000)). The standard explanation for *gradual* SEP events is that the CME-driven shock accelerates mainly the particles of the high altitude corona and they manage to retain the same characteristic composition of the corona when observed from 1 AU.

The two class paradigm was shown as too simplified in particular after the launch of the Advanced Composition Explorer (ACE) spacecraft in 1997. ACE observations (Moebius, 1999; Möbius et al., 1999; Mazur et al., 1999; Mason et al., 1999) indicate

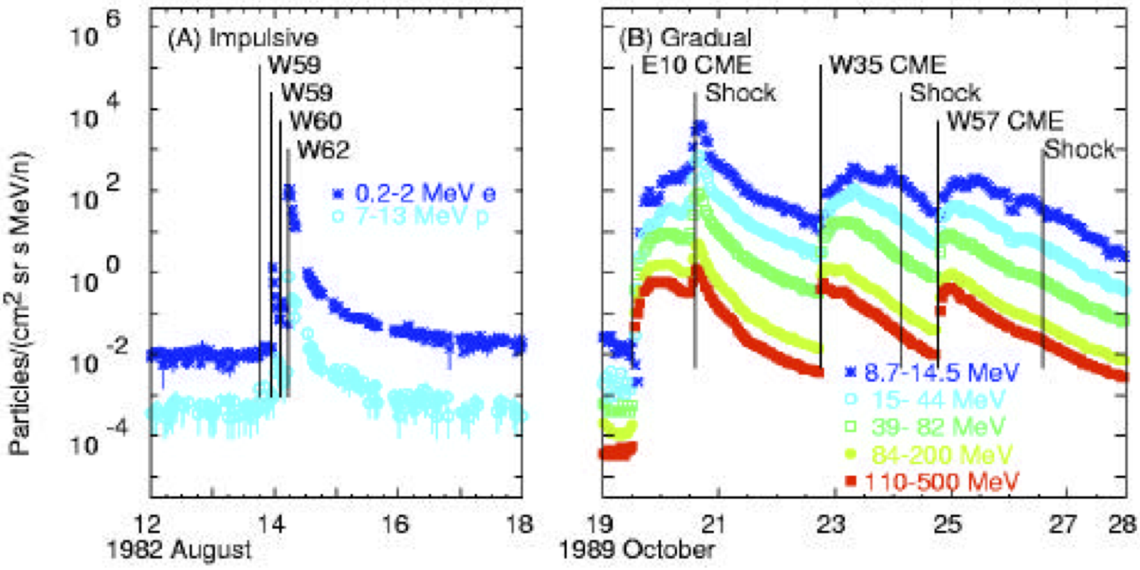

Figure 1.5: SEP event intensity profile in function of time for: (A) flare associated *impulsive* SEP event, (B) *gradual* SEP event.

Source: Reames (2002)

that many events actually show characteristics of both *impulsive* and *gradual* events A tentative explanation is that what were classified as *gradual* events actually having an *impulsive* core as previously proposed by Cliver (1996), and that besides a contribution from particles accelerated by the CME-driven shock *gradual* events show particles accelerated by similar acceleration processes to *impulsive* events.

1.3.1 Basics features of particle propagation in the interplanetary medium

In what follows, when we talk about the energy of a particle we implicitely mean the kinetic energy of that particle, unless otherwise noted. The kinetic energy E_k of a particle is defined as the difference between its relativistic total energy and its rest mass equivalent energy m_0 in a frame of reference where that particle has a velocity v. We typically use eV units for the energy (and thus also the equivalent rest mass) and consider that the velocity is given units of v/c, where c is the speed of light in vacuum. With these conventions, the quantities are related by the special relativity formula:

$$E_k = \frac{m_0}{\sqrt{1 - v^2}} - m_0 \tag{1.10}$$

A related quantity, the rigidity R of a charged particle is often used instead of the kinetic energy, particularly in the neutron monitor community. This quantity is essentially a measure of the particle momentum divided by its electric charge. The rigidity of a particle provides an indication of the resistance to deflection by a magnetic field. If the particle energy is in eV then the rigidity R is given in Volt and is related to the kinetic energy of the particle by the following equation:

$$R^2 = q^2(E_k^2 + 2m_0E_k) \tag{1.11}$$

where q is simply the number of elementary charges of the ion.

1.3.2 Particle propagation in the interplanetary medium

Since the solar wind emanating from a given source may vary its speed as a function of time, the true shape of the magnetic field line may deviate slightly from the spiral estimated from in situ measures of solar wind speed at 1 AU yet one should not expect departures exceeding 0.1 to 0.2 AU under quiet solar wind conditions; the intrinsic uncertainty in the path length at Earth will be on the order of 10%.

For the typical solar wind conditions in the ecliptic plane at 1 AU the average spiral length is about 1.2 AU meaning that a relativistic particle (speed $\sim c$) will take about 10 minutes to travel to Earth's orbit from its source very close to the Sun. Even a 20% uncertainty in the path length travelled means that an in situ event near Earth can still be pinpointed back to the Sun with an accuracy of about 2 minutes.

So for relativistic particles the uncertainty arising from path length uncertainty is not a strong limiting factor for timing studies. For a particle propagating at about $0.1c$ the release time uncertainty due to path length is on the order of 10 to 20 minutes, so definite associations with solar phenomena like a flare or CME will not be as clear as those that can be established for the higher energies. This is an important point that we will explore in this thesis: for timing studies it is very important to register the arrival of the fastest available particles, in particular we should include near relativistic particles. At Jupiter's orbit even relativistic particles can take more than two hours to travel from their source near the Sun, and as such timing associations with accuracy better than tens of minutes are problematic.

After the acceleration of charged particles takes place near the Sun's surface, those particles are injected into the interplanetary medium and as such we need to consider the effects this propagation will have on the properties that will be measured at 1 AU. The approach we will follow throughout the thesis are streamlined for example in Dröge (2003). The major assumption is that when there aren't large scale disturbances in the interplanetary medium, the magnetic field can be described as a smooth average field streaming along an Archimedian spiral to which we impose small scale irregularities. In this scenario we mostly ignore the effects of the plasma microturbulence on particle speed (energy is mostly conserved), but we assume that Alfvén waves, magnetoacustic waves, and waves arising from other modes in the plasma can efficiently scatter the particles in pitch angle. By this approximation, the motion of charged particles trough this interplanetary magnetic field can be described by two major features: (i) the adiabatic motion along a smooth magnetic field and (ii) the pitch angle scattering of the particles by microturbulence in the solar wind plasma. This is called the focus transport approximation and the analytical approach used in dealing with those two terms is based on the classical work of diffusion-convection analysis by Parker (1965). The evolution of the particle phase space density $f\,(z, \mu, t)$, i.e the number of particles per unit length of the magnetic field line and unit momentum, with no solar wind effects included is given by a Fokker-Planck equation (Roelof, 1969)

$$\frac{\partial f}{\partial t} + \mu v \frac{\partial f}{\partial z} + \frac{1-\mu^2}{2L} v \frac{\partial f}{\partial \mu} - \frac{\partial}{\partial} \left(D_{\mu\mu}(\mu) \frac{\partial f}{\partial \mu} \right) = Q\,(z, \mu, t) \tag{1.12}$$

where:

- z is the coordinate of the observer along the magnetic field line, μ is the cosine of pitch angle, t the time, v is the particle velocity
- $f = f(z, \mu, t)$ particles phase space density
- $L(z)$ is the focusing length of the field
- $D_{\mu\mu}(\mu)$ the pitch angle diffusion coefficient
- $Q(z, \mu, t)$ is the source function.

The focusing length in the diverging magnetic field $L\,(z) = B\,(z) \,/\, (-\partial B/\partial z)$ describes the systematic forces caused by magnetic mirroring and adiabatic focusing.

The two major approaches to model propagation effects as seen in particle events are describe in Ruffolo (1994) and Kocharov et al. (1998). Although these works present different methods of solving the transport equations both are in good agreement with other and with observations, although depending on an ad hoc tuning of the injection parameters. In subsequent sections and chapters we will address propagation effects following the kinetic Monte-Carlo approach given in Kocharov et al. (1998).

In simple terms the particles interact with moving magnetic gradients in the magnetic field, which, statistically, either change their pitch angle or increase their parallel speeds. The relative importance of each process will depend on the type of waves interacting with the particles. In general fast magnetosonic waves are responsible for stochastic acceleration whereas shear alfvén waves determine the pitch angle scattering of energetic particles.

1.4 The Ulysses and ACE Missions

The Ulysses spacecraft (Wenzel et al., 1992) was a joint project of ESA & NASA, launched in October 6, 1990 set for a trajectory which would travel on a polar orbit around the Sun after sling shooting through Jupiter gravitational pull. Figure 1.6 shows Ulysses' second orbit around Sun's magnetic poles, which took place from 1999 to 2004. By February 2008 the radioactive power source of the instrument stopped providing enough energy to keep the spacecraft's attitude control hydrazine fuel from freezing, but the mission team came up with a method to keep the fuel liquid by conducting a short thruster burn every two hours, allowing for the mission to continue. The last official day of the mission was then set for the 4th and last time to June 30, 2009.

Ulysses carried on board a great number of space-physics experiments, having as its main mission focus the characterization of the plasma environment in the polar regions of the heliosphere. Before Ulysses, very little was known about Sun's magnetic poles that was validated trough in situ measurements and as such the data gathered by Ulysses is invaluable in the sense that it is the single source of in situ data available about this region of space. This fact alone is enough to give special importance to this probe and to try and get the most out of this data. Part of Ulysses payload was

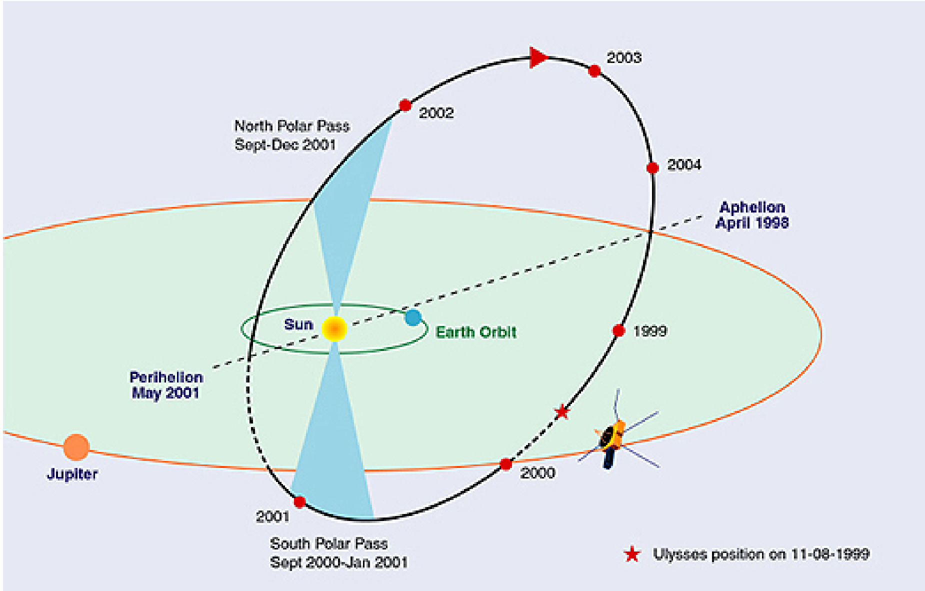

Figure 1.6: Ulysses' second orbit (1999 — 2004).
Source: NASA JPL

the Heliosphere Instrument for Spectra, Composition and Anisotropy at Low Energies, the HI-SCALE experiment (Lanzerotti et al., 1992). HI-SCALE was designed to make measurements of interplanetary ions ($E_i \gtrsim 50$ keV) and electrons ($E_e \gtrsim 30$ keV) as well as determining ion elemental abundances. This leaves us with almost nineteen years worth of in situ measurements from the polar region of heliosphere in an experiment that will not be replicated in the foreseeable future. As such, the detailed study of this instrument was one of the main objectives of this thesis.

On August 25, 1997, the Advanced Composition Explorer (ACE), carrying the Electron Proton Alpha Monitor (EPAM) instrument (Gold et al., 1998) — which was in all similar to HI-SCALE — was launched and set on an orbit around the Lagrangian L1 point (see figure 1.7). Its main objectives were to monitor the elemental, isotropic and ionic charge-state composition in near Earth interplanetary medium.

EPAM was actually a backup of the HI-SCALE to which it was similar in every

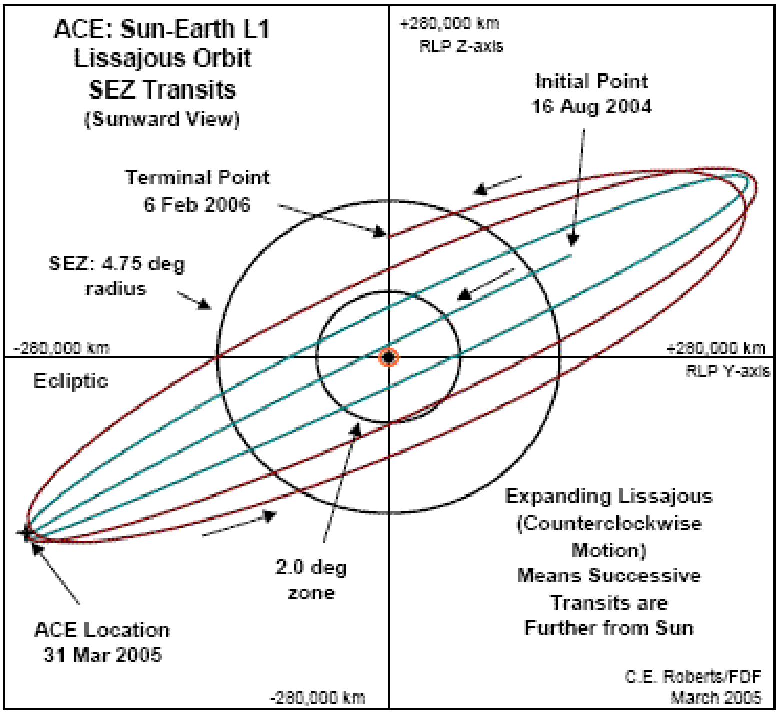

Figure 1.7: ACE orbit around the Lagrangian L1 point.
Source: Caltech

regard except for a slight difference in the angular disposition of the individual telescopes. The only real difference in these instruments when it comes to analyze their data is not in the instrument per se but in their background rates. There are two factors to take into account here. Firstly, that the inter planetary medium around both probes was completely different: Ulysses was set to an orbit that first took it through Jupiter's strong magnetosphere and then to a calm orbit that passed around the Sun's poles, orbiting the Sun in an orbit ranging from 1 to 5 AU; on the other hand, ACE is constantly set near the Earth and as such its background rates remain more or less the same trough all the mission. Secondly, ACE was powered by solar panels that didn't constitute a source of background noise for the probe, while Ulysses was powered by a radio thermal generator (RTG) that due to its radioactive nature presented a constant source of background noise for the instruments it carried. As such, except for this small difference, all the work done on this thesis on the analysis of the HI-SCALE instrument, also applies to EPAM with the added benefit that EPAM is still online and gathering data relevant to the study of Space Weather.

Throughout the work of the thesis, data from EPAM was used to analyze SEP events and to show that the methods developed here, are both in accordance and further constrain the onset timings of SEP events as seen on ground based Neutron Monitors detectors, and on the Energetic Proton, Electron, and Alpha Detector (EPEAD) on board the Geostationary Operational Environmental Satellite (GOES) for the particularly important solar event that took place on 2012, May, 17 and which was the first major SEP to take place solar cycle 24; the current solar cycle taking place during this thesis work.

1.5 Motivation

Although the spectra of SEP events for peak count rates and fluence were quite well constrained in HI-SCALE and EPAM, the effects of spurious response for onset times determination wasn't accurately known. Patterson (2002) had shown that counts due to galactic cosmic rays of energies on the order of hundreds of MeV were high enough to require subtraction from the channel counts in order to get the steady state spectra of low energy ions in the Heliosphere. Patterson (2002) thus prompted us to investigate if ion events with energies up to a GeV ought to be detected by the instrument. The near relativistic energy range for ions is particularly important since the propagation times involved fore the early arriving particles are between 9 and 13 minutes so the release time back at the Sun can be inferred with relatively accuracy and the link between in situ observations and remote observations can be made with some confidence.

Knowing the release time back at the Sun, is of special importance to determine the acceleration mechanisms of charged particles in SEP events and since the HI-SCALE is the only instrument that gathered in situ data of the polar regions of the heliosphere, it was then important to apply complementary analysis methods to the HI-SCALE data in order to be able to better determine these release times back at the Sun for SEP events.

1.6 Structure of the Thesis

This thesis work started by developing a simulation of the HI-SCALE detectors using Geant4 — a toolkit for the simulation of the passage of particles through matter using Monte Carlo methods (Agostinelli et al., 2003; Allison et al., 2006) — based on the engineering data available in the literature about the HI-SCALE (Armstrong and Hunt-Ward, 1999). The results obtained by running the simulation for a variety of input sources were then compared to the calibration results available in the literature as a way of validating the simulation. After this process was completed, the simulation was taken a step further in an effort to quantify the spurious response of the instrument — spurious meaning the response outside the nominal range of the instrument. This step gave a better picture of the profile of the deposited energy versus the input source energy, which would latter allow to better constrain the arrival times of SEP events at the electron side of the picture. The signal from particles with energies much higher than the instrument channel ranges, arriving at the instrument from directions that were previously thought of as having no impact in the readout signal of the detector, namely particles passing trough the instrument steel casing was also investigated. This process is described in Chapter 3.

In Chapter 4, the insights gathered during the processes described in the paragraph above, allowed to greatly extend the energy range for the proton detection, which was then used to further constrain the onset times of SEP events for protons on the EPAM. At the same time the method described in Chapter 3 for constraining the arrival time for electrons was also used to further constrain the onset of SEP events for electrons on the EPAM.

Finally, in Chapter 5 the results obtained by analyzing the data from the EPAM, were compared with the data from the Neutron Monitors and the GOES13 instrument and found to be in close agreement.

1.7 Innovation of the Thesis

This work made for 3 separate publications (Morgado et al., 2015; Maia and Morgado, 2014; Morgado and Maia, 2014) based on its findings. By using Geant4 to fully characterize an instrument already launched into space and still in operation — in the case of the EPAM, and confirming the prelaunch test batches of the instrument using that same model in Geant4, we made it possible to obtain a more complete analysis of the instrument's response and use that response to better characterize the electron channels' response and better constrain the onset of the arrival of electrons at the instrument. This method can be not only directly applied to the HI-SCALE and the EPAM, but with some modifications to other instruments as well. This part of the work is detailed in Morgado and Maia (2014).

Moreover on the proton side of the picture the results of the simulation allowed to quantify data from high energy particles entering trough the instrument casing and use this signal as a way to greatly extend the energy range of the instrument, effectively transforming it in one of the few instruments in orbit capable of detecting protons in an energy range that encompasses the keV to the GeV range. This part of the work is detailed in Morgado et al. (2015).

In Maia and Morgado (2014) we further validate the methods developed in this thesis work for these expanded energy ranges using EPEAD's data.

Bibliography

Agostinelli, S., Allison, J., Amako, K. e., Apostolakis, J., Araujo, H., Arce, P., Asai, M., Axen, D., Banerjee, S., Barrand, G., et al. (2003). Geant4—a simulation toolkit. *Nuclear instruments and methods in physics research section A: Accelerators, Spectrometers, Detectors and Associated Equipment*, 506(3):250–303.

Allison, J., Amako, K., Apostolakis, J., Araujo, H., Dubois, P. A., Asai, M., Barrand, G., Capra, R., Chauvie, S., Chytracek, R., et al. (2006). Geant4 developments and applications. *Nuclear Science, IEEE Transactions on*, 53(1):270–278.

Armstrong, T. and Hunt-Ward, T. (1999). Ulysses hiscale data analysis handbook, internal document. *Fundamental Technologies.*

Balogh, A., Gosling, J. T., Jokipii, J. R., Kallenbach, R., and Kunow, H. (1999). Introduction. *Space Sci. Rev.*, 89:1–3.

Barlow, W. (1849). On the spontaneous electrical currents observed in the wires of the electric telegraph. *Philosophical Transactions of the Royal Society of London*, 139:61–72.

Brueckner, G. E., Howard, R. A., Koomen, M. J., Korendyke, C. M., Michels, D. J., Moses, J. D., Socker, D. G., Dere, K. P., Lamy, P. L., Llebaria, A., Bout, M. V., Schwenn, R., Simnett, G. M., Bedford, D. K., and Eyles, C. J. (1995). The Large Angle Spectroscopic Coronagraph (LASCO). *Sol. Phys.*, 162:357–402.

Burlaga, L. F., Ness, N. F., Gurnett, D. A., and Kurth, W. S. (2013). Evidence for a Shock in Interstellar Plasma: Voyager 1. *ApJ*, 778:L3.

Cane, H. V., McGuire, R. E., and von Rosenvinge, T. T. (1986). Two classes of solar energetic particle events associated with impulsive and long-duration soft X-ray flares. *ApJ*, 301:448–459.

Carrington, R. C. (1863). *Observations of the spots on the sun: from November 9, 1853, to March 24, 1861, made at Redhill*. Williams and Norgate.

Cliver, E. W. (1996). Solar flare gamma-ray emission and energetic particles in space. In Ramaty, R., Mandzhavidze, N., and Hua, X.-M., editors, *American Institute of Physics Conference Series*, volume 374 of *American Institute of Physics Conference Series*, pages 45–60.

Cliver, E. W., Webb, D. F., and Howard, R. A. (1999). On the origin of solar metric type II bursts. *Sol. Phys.*, 187:89–114.

Domingo, V., Fleck, B., and Poland, A. I. (1995). The SOHO Mission: an Overview. *Sol. Phys.*, 162:1–37.

Dröge, W. (2003). Acceleration and propagation of solar energetic particles. In *Energy Conversion and Particle Acceleration in the Solar Corona*, pages 193–212. Springer.

Dungey, J. W. (1953). The motion of magnetic fields. *MNRAS*, 113:679+.

Dungey, J. W. (1958). The neutral point discharge theory of solar flares. a reply to cowling's criticism. In *IAU Symp. 6: Electromagnetic Phenomena in Cosmical Physics*, volume 6, pages 135+.

Gold, R., Krimigis, S., Hawkins III, S., Haggerty, D., Lohr, D., Fiore, E., Armstrong, T., Holland, G., and Lanzerotti, L. (1998). Electron, proton, and alpha monitor on the advanced composition explorer spacecraft. *Space Science Reviews*, 86(1-4):541–562.

Goldman, M. V. (1983). Progress and problems in the theory of type III solar radio emission. *Sol. Phys.*, 89:403–442.

Gopalswamy, N., Yashiro, S., and Akiyama, S. (2007). Geoeffectiveness of halo coronal mass ejections. *Journal of Geophysical Research (Space Physics)*, 112:A06112.

Gopalswamy, N., Yashiro, S., Krucker, S., Stenborg, G., and Howard, R. A. (2004). Intensity variation of large solar energetic particle events associated with coronal mass ejections. *Journal of Geophysical Research (Space Physics)*, 109:A12105.

Gopalswamy, N., Yashiro, S., Lara, A., Kaiser, M. L., Thompson, B. J., Gallagher, P. T., and Howard, R. A. (2003). Large solar energetic particle events of cycle 23: A global view. *Geophys. Res. Lett.*, 30:8015.

Gopalswamy, N., Yashiro, S., Xie, H., Akiyama, S., and Mäkelä, P. (2015). Properties and geoeffectiveness of magnetic clouds during solar cycles 23 and 24. *Journal of Geophysical Research (Space Physics)*, 120:9221–9245.

Gosling, J. T. (1993). The solar flare myth. *J. Geophys. Res.*, 98:18937–18950.

Gringauz, K. I., Kurt, V. G., Moroz, V. I., and Shklovskii, I. S. (1961). Results of Observations of Charged Particles Observed Out to R = 100, 000 km, with the Aid of Charged-Particle Traps on Soviet Space Rockets. *Soviet Ast.*, 4:680.

Hassler, D. M., Zeitlin, C., Wimmer-Schweingruber, R. F., Ehresmann, B., Rafkin, S., Eigenbrode, J. L., Brinza, D. E., Weigle, G., Böttcher, S., Böhm, E., and et al. (2014). Mars' Surface Radiation Environment Measured with the Mars Science Laboratory's Curiosity Rover. *Science*, 343:1244797.

Klein, K.-L., Masson, S., Bouratzis, C., Grechnev, V., Hillaris, A., and Preka-Papadema, P. (2014). The relativistic solar particle event of 2005 january 20: origin of delayed particle acceleration. *Astronomy & Astrophysics*, 572:A4.

Kocharov, L., Vainio, R., Kovaltsov, G., and Torsti, J. (1998). Adiabatic deceleration of solar energetic particles as deduced from monte carlo simulations of interplanetary transport. *Solar Physics*, 182(1):195–215.

Lanzerotti, L., Gold, R., Anderson, K., Armstrong, T., Lin, R., Krimigis, S., Pick, M., Roelof, E., Sarris, E., and Simnett, G. (1992). Heliosphere instrument for spectra, composition and anisotropy at low energies. *Astronomy and Astrophysics Supplement Series*, 92:349–363.

Lanzerotti, L. J. (2001). Space weather effects on communications. In *Space storms and space weather hazards*, pages 313–334. Springer.

Lara, A., Gopalswamy, N., Caballero-López, R. A., Yashiro, S., Xie, H., and Valdés-Galicia, J. F. (2005). Coronal Mass Ejections and Galactic Cosmic-Ray Modulation. *ApJ*, 625:441–450.

Maia, D., Aulanier, G., Wang, S. J., Pick, M., Malherbe, J.-M., and Delaboudinière, J.-P. (2003). Interpretation of a complex CME event: Coupling of scales in multiple flux systems. *A&A*, 405:313–323.

Maia, D. and Morgado, B. (2014). Timing of the 2012 may 17 gle using goes13 epead data. *Astronomy and Astrophysics, in press.*

Maia, D., Vourlidas, A., Pick, M., Howard, R., Schwenn, R., and Magalhães, A. (1999). Radio signatures of a fast coronal mass ejection development on November 6, 1997. *J. Geophys. Res.*, 104:12507–12514.

Mason, G., Mazur, J., and Dwyer, J. (1999). 3he enhancements in large solar energetic particle events. *The Astrophysical Journal Letters*, 525(2):L133.

Mazur, J., Mason, G., Looper, M., Leske, R., and Mewaldt, R. (1999). Charge states of solar energetic particles using the geomagnetic cutoff technique: Sampex measurements in the 6 november 1997 solar particle event. *Geophysical research letters*, 26(2):173–176.

McKenna-Lawlor, S., Gonçalves, P., Keating, A., Reitz, G., and Matthiä, D. (2012). Overview of energetic particle hazards during prospective manned missions to Mars. *Planet. Space Sci.*, 63:123–132.

Mel'Nik, V. N. and Kontar, E. P. (2003). Plasma Radio Emission of Beam-Plasma Structures in the Solar Corona. *Sol. Phys.*, 215:335–341.

Melrose, D. B. (1980). *Plasma astrohysics. Nonthermal processes in diffuse magnetized plasmas - Vol.1: The emission, absorption and transfer of waves in plasmas; Vol.2: Astrophysical applications.*

Möbius, E., Popecki, M., Klecker, B., Kistler, L., Bogdanov, A., Galvin, A., Heirtzler, D., Hovestadt, D., Lund, E., Morris, D., et al. (1999). Energy dependence of the ionic charge state distribution during the november 1997 solar energetic particle event. *Geophysical research letters*, 26(2):145–148.

Moebius, E. (1999). Variation of ionic charge states between solar energetic particle events as observed with ace sepica. In *International Cosmic Ray Conference*, volume 6, page 87.

Morgado, B., Filipe Maia, D. J., Lanzerotti, L., Gonçalves, P., and Patterson, J. D. (2015). The low energy magnetic spectrometer on Ulysses and ACE response to near relativistic protons. *A&A*, 577:A61.

Morgado, B. and Maia, D. (2014). Electron scattering profile of the epam experiment on ace. analysis of the electron event associated with the 2012 may 17 gle. *Astronomy and Astrophysics, in press.*

Parker, E. N. (1958). Dynamics of the Interplanetary Gas and Magnetic Fields. *Astrophysical Journal*, 128:664.

Parker, E. N. (1965). The passage of energetic charged particles through interplanetary space. *Planetary and Space Science*, 13(1):9–49.

Patterson, J. D. (2002). *An analysis of solar energetic particles throughout the inner heliosphere*. PhD thesis, UNIVERSITY OF KANSAS.

Pick, M., Forbes, T. G., Mann, G., Cane, H. V., Chen, J., Ciaravella, A., Cremades, H., Howard, R. A., Hudson, H. S., Klassen, A., Klein, K. L., Lee, M. A., Linker, J. A., Maia, D., Mikic, Z., Raymond, J. C., Reiner, M. J., Simnett, G. M., Srivastava, N., Tripathi, D., Vainio, R., Vourlidas, A., Zhang, J., Zurbuchen, T. H., Sheeley, N. R., and Marqué, C. (2006). Multi-Wavelength Observations of CMEs and Associated Phenomena. Report of Working Group F. *Space Sci. Rev.*, 123:341–382.

Pohjolainen, S., Maia, D., Pick, M., Vilmer, N., Khan, J. I., Otruba, W., Warmuth, A., Benz, A., Alissandrakis, C., and Thompson, B. J. (2001). On-the-Disk Development of the Halo Coronal Mass Ejection on 1998 May 2. *ApJ*, 556:421–431.

Priest, E. R. (1982). *Solar magneto-hydrodynamics*. Dordrecht, Holland ; Boston : D. Reidel Pub. Co. ; Hingham,.

Reames, D. V. (1993). Non-thermal particles in the interplanetary medium. *Advances in Space Research*, 13:331–339.

Reames, D. V. (1999). Particle acceleration at the Sun and in the heliosphere. *Space Sci. Rev.*, 90:413–491.

Reames, D. V. (2002). Solar energetic particles. *Adv. Sp. Res.*

Reames, D. V., Meyer, J., and Von Rosenvinge, T. (1994). Energetic-particle abundances in impulsive solar flare events. *The Astrophysical Journal Supplement Series*, 90:649–667.

Reiner, M. J. and Kaiser, M. L. (1999). High-frequency type ii radio emissions associated with shocks driven by coronal mass ejections. *J. Geophys. Res.*, 104:16979–16992.

Ruffolo, D. (1994). Effect of adiabatic deceleration on the focused transport of solar cosmic rays. *arXiv preprint astro-ph/9408056*.

Ryan, J. M., Lockwood, J. A., and Debrunner, H. (2000). Solar energetic particles. *Space Science Reviews*, 93(1-2):35–53.

Schwabe, M. (1843). Die Sonne. Von Herrn Hofrath Schwabe. *Astronomische Nachrichten*, 20:283.

Schwenn, R., Raymond, J. C., Alexander, D., Ciaravella, A., Gopalswamy, N., Howard, R., Hudson, H., Kaufmann, P., Klassen, A., Maia, D., Munoz-Martinez, G., Pick, M., Reiner, M., Srivastava, N., Tripathi, D., Vourlidas, A., Wang, Y.-M., and Zhang, J. (2006). Coronal Observations of CMEs. Report of Working Group A. *Space Sci. Rev.*, 123:127–176.

Sturrock, P. A. (1964). Type III Solar Radio Bursts. *NASA Special Publication*, 50:357.

Tousey, R., Bartoe, J. D. F., Bohlin, J. D., Brueckner, G. E., Purcell, J. D., Scherrer, V. E., Sheeley, N. R., Schumacher, R. J., and Vanhoosier, M. E. (1973). A preliminary study of the extreme ultraviolet spectroheliograms from skylab. *Sol. Phys.*, 33:265+.

Tsurutani, B. T., Gonzalez, W. D., Gonzalez, A. L. C., Guarnieri, F. L., Gopalswamy, N., Grande, M., Kamide, Y., Kasahara, Y., Lu, G., Mann, I., McPherron, R., Soraas, F., and Vasyliunas, V. (2006). Corotating solar wind streams and recurrent geomagnetic activity: A review. *Journal of Geophysical Research (Space Physics)*, 111:A07S01.

Vilmer, N. (2012). Solar flares and energetic particles. *Philosophical Transactions of the Royal Society of London Series A*, 370:3241–3268.

Vourlidas, A., Wu, S. T., Wang, A. H., Subramanian, P., and Howard, R. A. (2003). Direct Detection of a Coronal Mass Ejection-Associated Shock in Large Angle and Spectrometric Coronagraph Experiment White-Light Images. *ApJ*, 598:1392–1402.

Wenzel, K., Marsden, R., Page, D., and Smith, E. (1992). The ulysses mission. *Astronomy and Astrophysics Supplement Series*, 92:207.

Wild, J. P. and McCready, L. L. (1950). Observations of the Spectrum of High-Intensity Solar Radiation at Metre Wavelengths. I. The Apparatus and Spectral Types of Solar Burst Observed. *Australian Journal of Scientific Research A Physical Sciences*, 3:387.

Chapter 2

The instruments

Contents

2.1 HI-SCALE and EPAM

The HI-SCALE and EPAM instruments are composed of 5 telescopes designed to detect both electrons and ions. These two instruments — HI-SCALE and EPAM — are part of the instrumentation of the Ulysses and ACE satellites respectively. It should be pointed out though, that although HI-SCALE and EPAM are similar in practically every aspect, the Ulysses and ACE satellites are part of two vastly different missions with a different set of instruments and objectives.

The telescopes that constitute HI-SCALE and EPAM have 3 variations according to their specific purpose. The first variation was the Low-Energy Foil Spectrometer (LEFS) used in two telescopes, where the LEFS60 houses the F' detector and LEFS150 the F detector. These were designed to detect electrons with energies ranging from 40 keV to 300 keV and protons with energies in the range 350 keV to 5 MeV, while stopping low energy ions with energies below 350 keV using a parylene foil — hence the

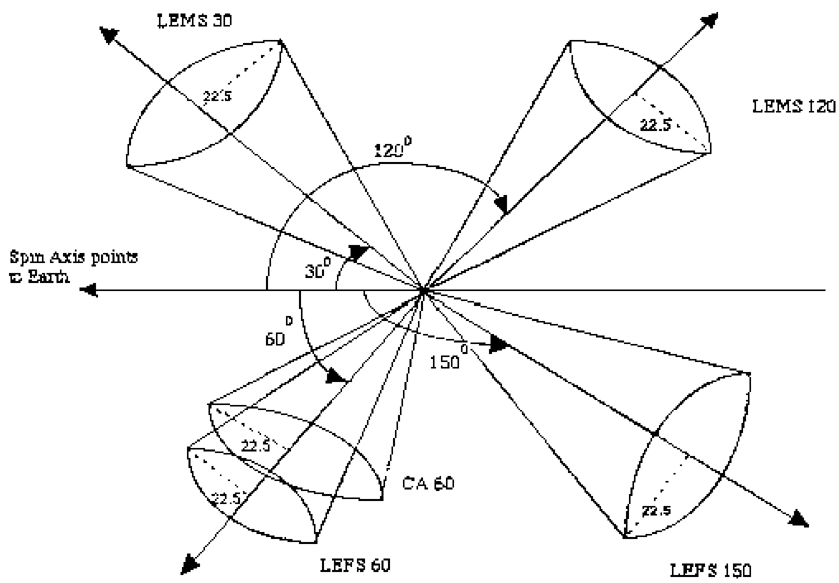

Figure 2.1: HI-SCALE viewing cones with respect to Ulysses spin axis.
Source: Lanzerotti et al. (1992)

name. The second variation was the Low-Energy Magnetic Spectrometer (LEMS) also used in two telescopes, where the LEMS120 houses the M' detector and LEMS30 the M detector. These were designed to detect protons with energies between 50 keV and 5 MeV, while sweeping out electrons with energies below 300 keV using a permanent earth magnet. Finally the third variation is the Composition Aperture (CA) used only in the CA60 telescope that houses the B, C and D detectors. This telescope works as a ΔE vs E telescope using a thin 5 μm front solid state detector element in a three-element telescope designed to detect ions from a minimum of 50 keV up to more than 1 GeV per nucleon while identifying their atomic mass.

All the detectors — F, F', M, M', B and C — except for D, are identical 200 μm thick totally depleted circular silicon surface barrier detectors with 5652 μm radius and all use the same mounts, for ease of pre-flight replacement. The LEFS60 and LEMS120 have a 53 degree full-width look angle, LEFS150 and LEMS30 a 51 degree look angle and the CA60 a 45 degree look angle as seen in figure 2.1.

LEFS60 and LEMS120 were assembled together in the LAN 2A instrument and the LEFS150, LEMS30 and the CA60 in the LAN 2B instrument. The numbers following the detector names, refer to the angle in degrees from the spacecraft spin-axes (figure 2.1) and the F, M and CA refer, respectively to the foils in the LEFS systems, the magnets in the LEMS systems and the composition aperture in CA itself. The overall schematic of the LAN2A and LAN2B can be seen in figure 2.2.

Both the Ulysses and the ACE spacecrafts make a full rotation every 12 seconds, allowing to separate the detected flux in 4 or 8 spatial sectors — depending on the detector (see tables 2.1 and 2.2) — at the electronic level during this 12 second period. As the spacecraft spins the telescopes provide a nearly complete 4π coverage of the unit sphere divided in 4 or 8 equally spaced sectors (see figure 2.3). This in turn, makes it is possible to use the flux measured in each sector to calculate the anisotropy during an event. Unfortunately the LEMS30 and the LEFS150 on the EPAM became erratic following the Halloween ion events in 2003 so we will not use those data (Haggerty et al., 2006).

The energy channels are separated using an anti coincidence logic system — detailed in tables 2.1 and 2.2 — comprising several energy levels — detailed in tables 2.3 and 2.4. Using this anti coincidence system between the F and the M detector pair, the F' and the M' detector pair and the B and C detector pair, particles with energies that surpass the maximum absorbed energy by each one of the 200 μm silicon detectors, would also deposit some energy on the complementary detector right in front of it and — in the case where the energy deposited in the complementary detector, reached the lowest energy threshold for that detector as expressed in tables 2.3 and 2.4 — be discarded by the electronics logic system, when registering a nearly-simultaneous

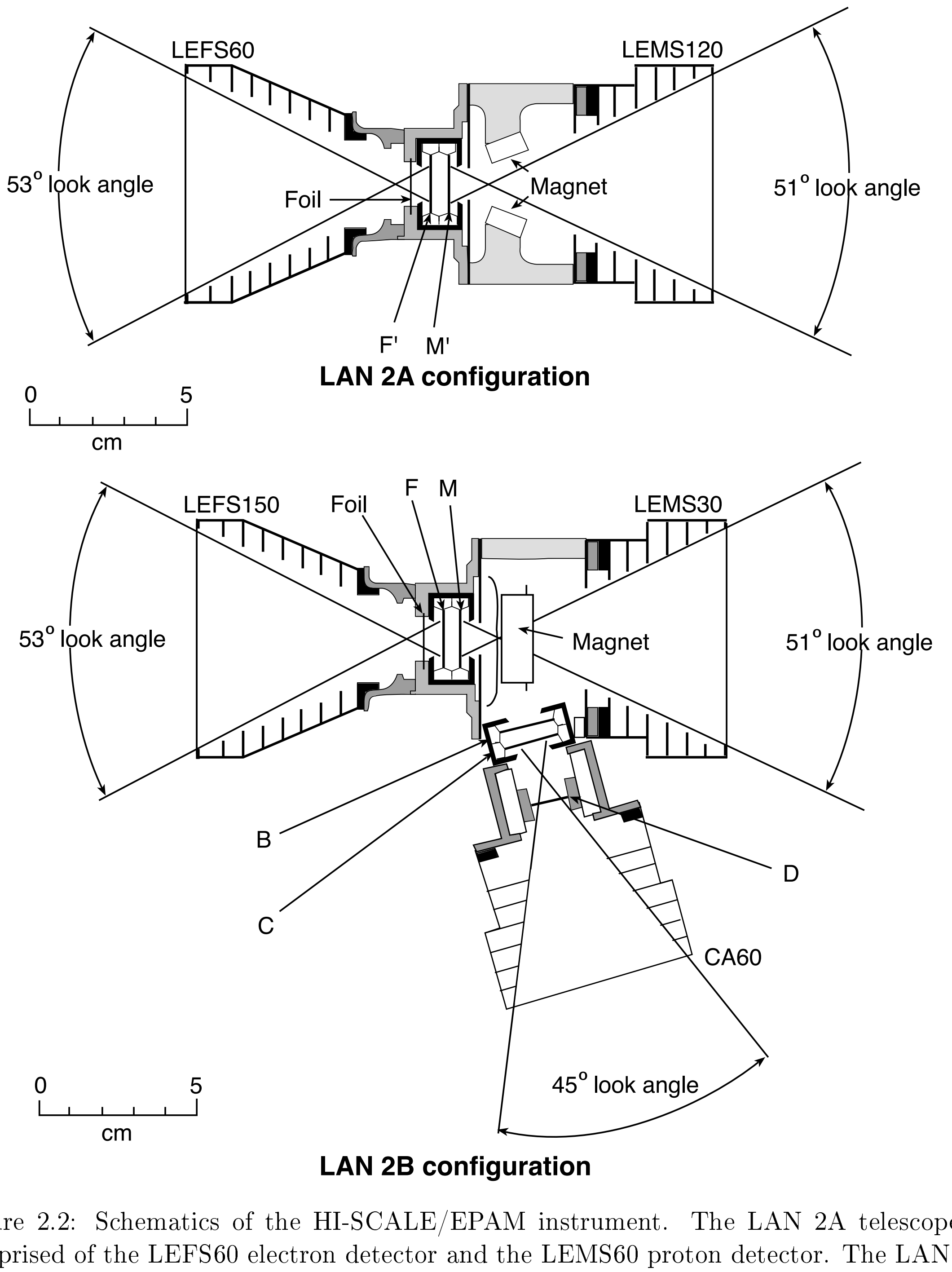

Figure 2.2: Schematics of the HI-SCALE/EPAM instrument. The LAN 2A telescope is comprised of the LEFS60 electron detector and the LEMS60 proton detector. The LAN 2B is comprised of the LEFS150 electron detector and the LEMS30 proton detector and the CA60 composition aperture.

Source: Gold et al. (1998)

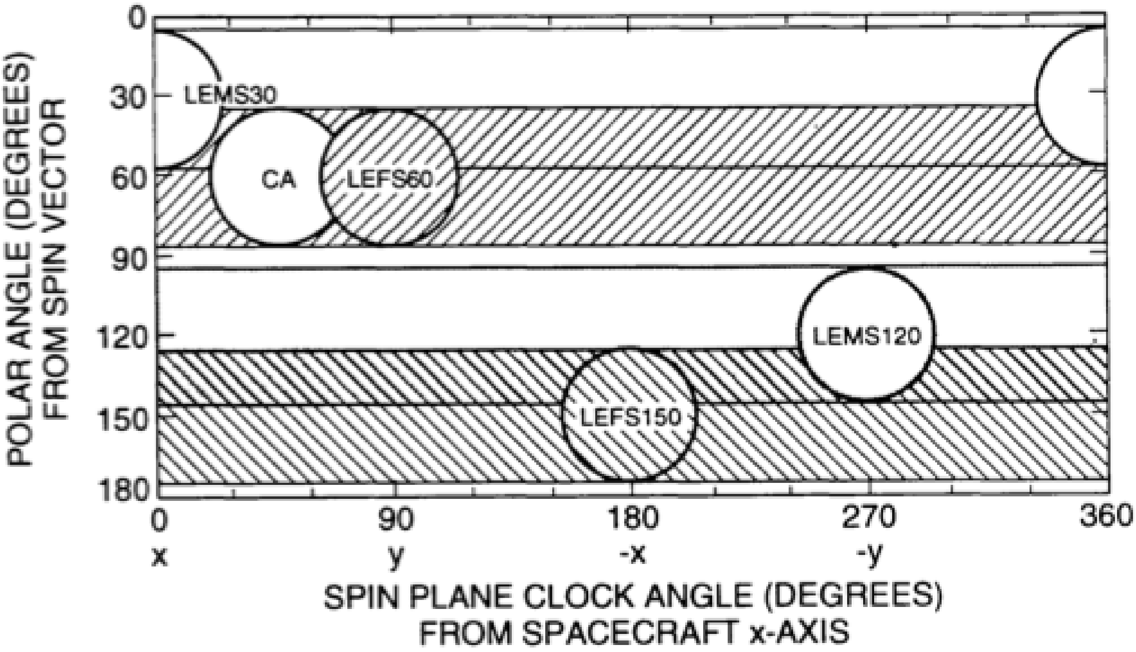

Figure 2.3: Instantaneous look direction of the four LEMS/LEFS telescopes on the 4π steradian sphere. One spacecraft rotation (~ 12) takes each telescope through a 360 degree angle, and thus the entire sphere is covered in each rotation.
Source: Lanzerotti et al. (1992)

pulse on both of the detectors in that particular detector pair.

The exact values for these levels, where obtained pre-flight by calibrating the electronic response of the instrument directly connected to a pulse input source and as such they don't take into account any other instrument characteristics.

As it was found out during this thesis work though, there are scenarios where this anti-coincidence system doesn't show the full picture of the data. Very high energy protons may enter directly trough the instrument steel casing with such an angle, that they pass only trough one detector, leaving a small part of their energy there to be reported by the instrument as a low energy particle. Besides that, the electronic noise of system will also introduce some statistical errors that must be accounted for in the final picture. Refer to Section 3.4 for a detailed analysis of this issue.

The original design of the instrument was slightly different from the one that actually got launched into space. The original design had two CA telescopes and as such two identical pairs of 3 telescopes each, doing away with the need for the parylene foil by using magnets also in the LEFS telescopes. Due to weight constrains though, this design had to be modified and one of the CA telescopes had to be removed as well as the magnets in the LEFS detectors and instead of those the foil was added in order to keep the weight of the instrument down in this final design.

An effect that became apparent during this thesis work, is that a substantial part

Detector	Channel	Logic	Sectors	1024 bit time
LEMS30 (M, F)	P1	M1 $\overline{\text{M2}}$ $\overline{\text{F}}$	4	3
	P2	M2 $\overline{\text{M3}}$ $\overline{\text{F}}$	4	3
	P3	M3 $\overline{\text{M4}}$ $\overline{\text{F}}$	4	3
	P4	M4 $\overline{\text{M5}}$ $\overline{\text{F}}$	4	3
	P5	M5 $\overline{\text{M6}}$ $\overline{\text{F}}$	4	6
	P6	M6 $\overline{\text{M7}}$ $\overline{\text{F}}$	4	6
	P7	M7 $\overline{\text{M8}}$ $\overline{\text{F}}$	4	6
	P8	M8 $\overline{\text{F}}$	4	6
LEMS120 (M', F')	P1'	M1 $\overline{\text{M2}}$ $\overline{\text{F}}$	8	1.5
	P2'	M2 $\overline{\text{M3}}$ $\overline{\text{F}}$	8	1.5
	P3'	M3 $\overline{\text{M4}}$ $\overline{\text{F}}$	8	1.5
	P4'	M4 $\overline{\text{M5}}$ $\overline{\text{F}}$	8	1.5
	P5'	M5 $\overline{\text{M6}}$ $\overline{\text{F}}$	8	1.5
	P6'	M6 $\overline{\text{M7}}$ $\overline{\text{F}}$	8	3
	P7'	M7 $\overline{\text{M8}}$ $\overline{\text{F}}$	8	3
	P8'	M8 $\overline{\text{F}}$	8	3
LEMS30 (B, C)	DE1	B1_A $\overline{\text{B2}}$ $\overline{\text{C}}$	4	6
		B1_B $\overline{\text{B2}}$ $\overline{\text{C}}$	4	6
	DE2	B2 $\overline{\text{B3}}$ $\overline{\text{C}}$	4	6
	DE3	B3 $\overline{\text{B4}}$ $\overline{\text{C}}$	4	6
	DE4	B4 $\overline{\text{B5}}$ $\overline{\text{C}}$	4	6

Table 2.1: LEMS detector system summary. The M' and the M detectors are similar but they average the signal in 8 intervals on the LEMS120 and only in 4 in LEMS30. This meant that LEMS120 has a greater angular resolution but on the downside it has higher noise levels in each sector.

Detector	Channel	Logic	Sectors	1024 bit time
LEFS150 (M, F)	F1	F1 $\overline{F2}$ $\overline{M}$	4	3
	F2	F2 $\overline{F3}$ $\overline{M}$	4	3
	F3	F3 $\overline{F4}$ $\overline{M}$	4	3
	F4	F4 $\overline{F5}$ $\overline{M}$	4	3
	F5	F5 $\overline{F6}$ $\overline{M}$	4	6
	F6	F6 $\overline{F7}$ $\overline{M}$	4	6
	F7	F7 $\overline{M}$	4	6
LEFS60 (M', F')	F1'	F1 $\overline{F2}$ $\overline{M}$	8	1.5
	F2'	F2 $\overline{F3}$ $\overline{M}$	8	1.5
	F3'	F3 $\overline{F4}$ $\overline{M}$	8	1.5
	F4'	F4 $\overline{F5}$ $\overline{M}$	8	1.5
	F5'	F5 $\overline{F6}$ $\overline{M}$	8	3
	F6'	F6 $\overline{F7}$ $\overline{M}$	8	3
	F7'	F7 $\overline{M}$	8	3

Table 2.2: LEFS detector system summary. The F' and F detectors are similar but they average the signal in 8 intervals on the LEFS60 and only in 4 on the LEFS150. This means that the LEFS60 has a greater angular resolution but on the downside it has higher noise levels in each sector.

of the counts due to electrons with energies above 300 keV — which were supposed to be discarded by using the anti coincidence between the F detectors and the M detectors — end up being detected in the FP5 channels, designed to detect only ions.

2.2 GOES13

Studying the data from the Energetic Proton, Electron, and Alpha Detector (EPEAD) onboard the Geostationary Operational Environmental Satellite (GOES) was an important step in order to validate the methods developed during this thesis work for the EPAM. EPEAD is an instrument that detects ions and electrons within an energy range relevant to the analysis of SEP events and complements the energy range of the EPAM, making it and important source of data for this work.

The GOES13 satellite has 2 EPEAD instruments, one of them with a FOV to the

Threshold Level	M (keV)	F (keV)
1	30	36
2	49	49
3	97	98
4	180	164
5	303	278
6	563	560
7	1040	1050
8	1800	—

Table 2.3: Energy threshold levels for logic parameters of the LEMS30 and LEFS150 telescopes obtained by pre-flight calibration using a pulse input source.

east and another to the west, they are similar in every regard but the data analyzed here, came from the west EPEAD. Each of the EPEAD consists of a proton/ion detector and three domes. A schematic of the probe can be seen in figure 2.4.

All the relevant data pertaining to the GOES is readily available in the instrument handbook (Hanser, 2011), which thoroughly details the energy, angular and geometric response of the instrument channels. This means that unlike for the HI-SCALE/EPAM there was no need to build a detailed virtual representation of the instrument and to repeat the same tests carried out for the HI-SCALE/EPAM using Monte Carlo methods in order to more thoroughly ascertain these quantities.

Threshold Level	M' (keV)	F' (keV)
1	34	36
2	48	53
3	94	103
4	172	172
5	302	288
6	568	550
7	1100	1050
8	1850	—

Table 2.4: Energy threshold levels for the logic parameters of the LEMS120 and LEFS60 telescopes obtained by the pre flight calibration using a pulse input source.

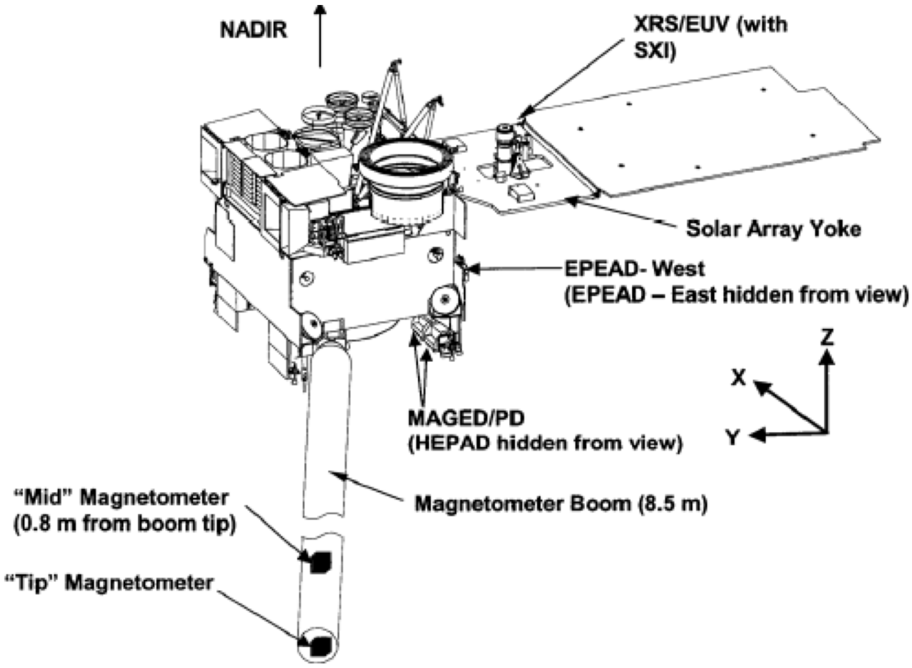

Figure 2.4: GOES13 schematic view showing solar panels and EPEAD-West look direction. *Source: Hanser (2011)*

Table 2.5 shows the proton channels of the EPEAD. When considering the spurious response, we should divide these channels into three categories. The low energy channels, where the nominal energy range is quite below the spurious response, these are the GP1, GP2, and GP3. In these channels given the energies detected, the spurious signal will arrive long before the nominal signal, allowing to clearly distinguish

Channel	Nominal Response (MeV)	Spurious Response (MeV)
GP1	0.74 — 4.2	50 — 100
GP2	4.2 — 8.7	50 — 125
GP3	8.7 — 14.5	60 — 125
GP4	15 — 40	115 — 150
GP5	38 — 82	110 — 190
GP6	—	84 — 300
GP7	—	110 — 900

Table 2.5: Proton channel response of the EPEAD instrument.

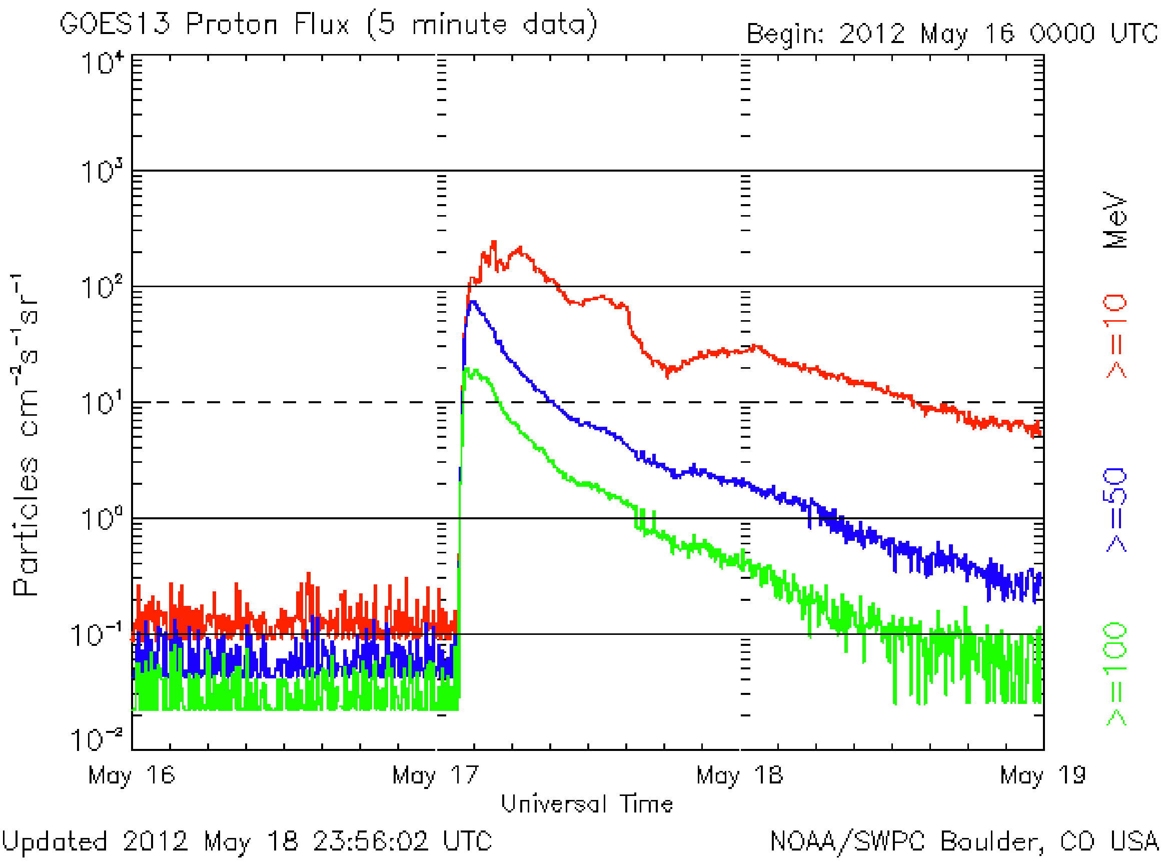

Figure 2.5: Overview of the 2012, May 17 event as seen by the EPEAD instrument onboard GOES13 on the proton channels.

Source: Space Weather Prediction Center

between the spurious and the nominal signals by analyzing the count rate curves. Then we have the medium energy channels, GP4 and GP5. In these channels, taking into account that the we expect the flux to decrease with the energy, and given the fact that the difference between these channels nominal energy and spurious energy is quite small, by the time we have enough counts to rise above the pre-event noise in the spurious channels, we should already be picking the arrival in the nominal channels. As such, a separate peak will become difficult to distinguish in this case. Finally we have the high energy channels, GP6 and GP7 where there is an overlap both in the energy range and in the arrival times, meaning that the spurious response is already included in all the calculations for these channels.

Figure 2.5 shows the 2012, May 17 event as seen on the EPEAD proton channels separated in the way described above.

2.3 The Neutron Monitor Network

The Neutron Monitor Network is comprised of several stations around the world, whose main objective is to detect neutrons produced by galactic cosmic rays interacting with the atmosphere. Besides the detection of these galactic cosmic rays, when a SEP event is strong enough, the stations near the poles — due to the Earth's lower magnetic field at those locations — can detect the presence of secondaries from protons of the event when they reach Earth's atmosphere, and provide a good onset timing method for high energy protons on SEP events.

The work carried out for this thesis with the data provided by these stations was exclusively about data analysis and timing measurements and was accomplished following the data treatment methods also used for EPAM and GOES13 as explained in Morgado et al. (2015); Maia and Morgado (2014). The only difference from the work carried out for EPAM and GOES13 is that for these monitors, one needs to calculate the cutoff rigidity — that depends on the local atmospheric conditions and Earth magnetic field — in order to be able to estimate the proton energies that are being detected in each monitor.

Bibliography

Gold, R., Krimigis, S., Hawkins III, S., Haggerty, D., Lohr, D., Fiore, E., Armstrong, T., Holland, G., and Lanzerotti, L. (1998). Electron, proton, and alpha monitor on the advanced composition explorer spacecraft. *Space Science Reviews*, 86(1-4):541–562.

Haggerty, D., Roelof, E., Ho, G., and Gold, R. (2006). Qualitative comparison of ace/epam data from different detector heads: Implications for noaa rtsw users. *Advances in Space Research*, 38(5):995–1000.

Hanser, F. (2011). Eps/hepad calibration and data handbook. Technical report, Tech. Rep. GOESN-ENG-048D.

Lanzerotti, L., Gold, R., Anderson, K., Armstrong, T., Lin, R., Krimigis, S., Pick, M., Roelof, E., Sarris, E., and Simnett, G. (1992). Heliosphere instrument for spectra, composition and anisotropy at low energies. *Astronomy and Astrophysics Supplement Series*, 92:349–363.

Maia, D. and Morgado, B. (2014). Timing of the 2012 may 17 gle using goes13 epead data. *Astronomy and Astrophysics, in press.*

Morgado, B., Filipe Maia, D. J., Lanzerotti, L., Gonçalves, P., and Patterson, J. D. (2015). The low energy magnetic spectrometer on Ulysses and ACE response to near relativistic protons. *A&A*, 577:A61.

Chapter 3

Simulation of the detectors

Contents

3.1 Overview

The relevant detectors on the HI-SCALE/EPAM are silicon based detectors widely used in solid state telescopes (SSTs) for space observations, due to their low weight and energy requirements as well as for their versatility in detecting the spectra of several types of radiation. This thesis project started by developing a virtual representation of the HI-SCALE instrument in Geant4 (Agostinelli et al., 2003; Allison et al., 2006). Geant4 is a toolkit using Monte Carlo methods to simulate physical interactions of particles with matter. Geant4 simulates a vast array of energy losses that take place inside the detector, as well as the production of secondary particles and their losses, allowing one to determine the energy that is deposited in each element of the detector,

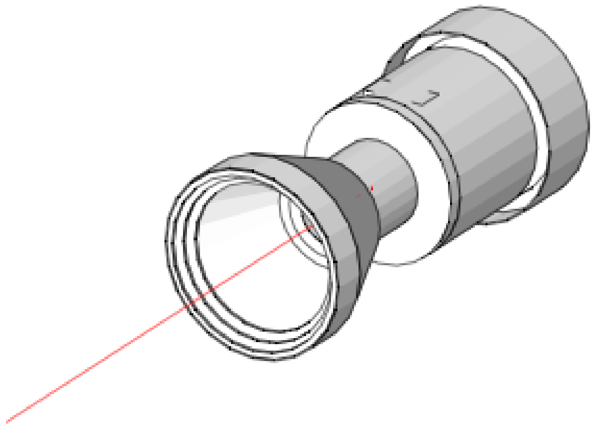

Figure 3.1: LAN 2A simulation model in Geant4. The instrument was simulated using data from the instrument handbook. Most of the effects could be simulated with a simpler setup, but as it was found out later, the geometric factor of both LEFS telescopes, was indeed highly dependent on the geometry and as such this level of detail in the simulation eventually paid off in the end.

which is the main objective for this work.

There were 3 features of HI-SCALE/EPAM that were specially relevant to the simulation and were extracted from the literature (Lanzerotti et al., 1992). The steel casing, built into the simulation using the measures obtained from Armstrong and Hunt-Ward (1999), simulated by a material composed of 73.85% Iron, 18% Chromium, 0.15% Carbon and 8% Nickel. The F and M detectors, both identical with a thickness of 200 μm and made of silicon, simulated using a 100% Silicon material. And the foil, simulated as a central parylene part with 2.35 μm thickness made of an homogeneous mixture of a material composed by a molecule with 6 C atoms and 8 H atoms and a density of 1.11 g/cm^3, supported on both sides by an aluminum film with a thickness of 0.4760 μm composed of a 100% Aluminum material. Figure 3.1 shows the virtual representation of the LAN 2A instrument built using the process depicted above.

With the virtual simulation of the instrument completed, several tests were carried out where the relation between the energy emitted by some specific particle source (namely, electron and proton sources) and the energy which was actually deposited at several places in the instrument (namely on the silicon detectors and on the parylene foils) was studied in order to better understand the behavior of the detectors.

Knowing the geometry and the materials which compose the instrument is just a part of the picture though. Geant4 simulates the relevant physical processes as the particles travel trough the materials inside the telescopes using special physical lists that are optimized for vastly different energy ranges. The physical lists used were the QGSP_BIC_HP lists for the electron simulations and the FTFP_BERT lists for the ion simulations, since they were the relevant ones for the energy ranges used throughout the simulations.

As a side note, some simulations were carried out for very high energy photons (extreme UV to hard X-ray range) that actually wield a detected signal due to secondary production after they hit the surfaces of the instrument. The results obtained from carrying out these simulations may actually be worth exploring in the future, but for now, it was decided to be outside the scope of this thesis and as such they won't be presented in the discussion that follows.

3.2 Silicon based detector degradation due to hadron collisions

One potentially relevant aspect that needs to be taken into account for all the upcoming discussion is that silicon based detectors when subjected to hadronic radiation degradation over time. Lindström (2003) thoroughly discusses this issue and some ways to mitigate it on future detectors — in a research that was mainly directed at the detectors that would be used at the Large Hadron Collider (LHC) at the time his research was carried out.

Lindström (2003) puts forward the value of $\sim 10^{14}\,\mathrm{cm}^{-2}$ protons as a limit for the fluence levels hindering the functioning of SSDs and Wüest et al. (2007) states that damage starts to affect SSDs for an irradiation between $10^{12}\,\mathrm{cm}^{-2}$ to $10^{13}\,\mathrm{cm}^{-2}$ protons and exhibits a significant degradation after a fluence ranging between $10^{14}\,\mathrm{cm}^{-2}$ to $10^{15}\,\mathrm{cm}^{-2}$. When reaching these levels of fluence, Peltola (2014) expects for the efficiency to drop by a factor of two and for the detector noise to be able to reach a substantial level in such a way that the lowest channel discriminators become unusable. This indeed presents a problem for the EPAM on the detectors facing the Sun and are one of the reasons presented in Haggerty et al. (2006) for the failure of the LEMS30 detector from October, 2003 forward. This problem is minimized on the detectors facing away from the Sun since they receive a lower dose of proton radiation.

Historical data from the LEMS120 on EPAM channels gives us a total dose of nearly $\sim 10^{12}\,\mathrm{cm}^{-2}$ — two orders of magnitude bellow the limit suggested in Lindström (2003) — so the performance of the detector should be only slightly degraded. It should be noted nonetheless that Haggerty and Roelof (2006) points out that the noise levels in P'1 on EPAM are indeed rather high and the counts often show a considerable number of spikes. As such using P'1 on EPAM was generally avoided during the data analysis part of this work.

3.3 The LEFS electron detectors

The main complication on a silicon based detector when it comes to measure electron counting rates, is that part of the high energy electrons reaching the detector get detected in lower energy channels due to the nature by which they interact with mater. In order to assess this effect, was simulated an electron beam ranging from 1 keV to 1 MeV directed along the normal direction at the centre of the F' detector

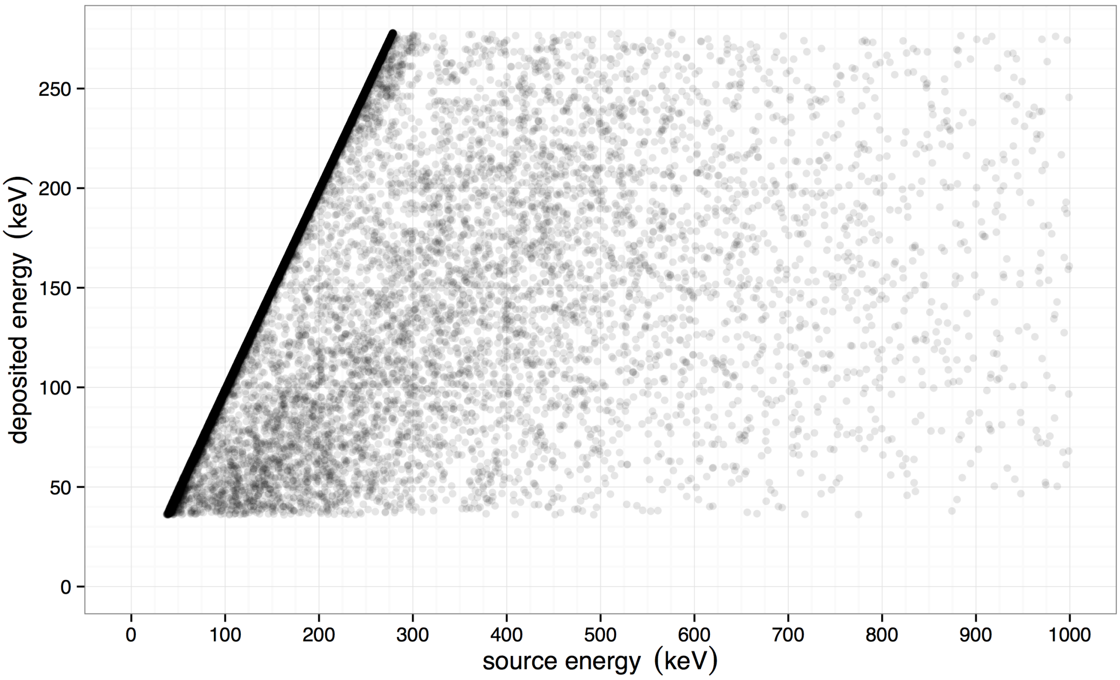

Figure 3.2: Detector response in the E1 to E5 range, from the Geant4 simulation with no electronic noise added.

and determined the energy that got deposited onto it. In figure 3.2 we see that the electrons with energies below 30 keV are, like expected in the instrument literature, stopped by the parylene foil that sits in front of the F and F' detectors, but, although the average deposited energy closely follows the source energy for energies above 30 keV, there is a great amount of particles that are detected with a much lower energy.

The charge built up at the silicon detector when a particle is absorbed, passes trough a charge-sensitive pre amplifier that produces an output signal proportional to it. If this value is higher than a discriminator threshold set by the electronics then a count is made. The whole process is affected by noise and the discriminator response function $D_R(E)$ can be approximated by the complementary error function (Nikitin et al., 1997):

channel	σ (keV)
1	6.1
2	8.0
3	10.0
4	10.0
5*	10.0

Table 3.1: Pre-amplifier noise (σ) and discriminator threshold levels (ξ) for the E, E' channels on the F, F' detectors (assumed to by identical since there is no separate data for both) obtained by fitting the complementary error function (eq. 3.1) to the pre-flight calibration data.

$$D_R(E) = \frac{1}{2}\,\mathrm{erfc}\left(\frac{\xi - E}{\sigma\sqrt{2}}\right), \tag{3.1}$$

where σ is the pre-amplifier noise and ξ the discriminator threshold level.

The manufacturer instrument details gives — ratter conservatively — a value for σ of 10 keV for every channel, but by fitting eq. 3.1 to the pre fight calibration data of the discriminator levels presented in tables 2.1 and 2.2 for the F detector and using Nikitin et al. (1997) findings, is possible to get lower values for F1, F1' and F2, F2' (the calibration was made for the detector F and B only, so it was assumed for F' to have the same noise values as F). These findings are presented in table 3.1 and figure 3.3.

After carrying out these calculation, the electronic effects can be taken into account simply by applying the statistical error of the pre-amplifier noise into the previously obtained data from the simulation. Using the σ parameter from table 3.1 as noise added to the energy deposit of every detected particle following a normal distribution the results presented in figure 3.4 are then obtained and as can be seen, there is a spreading of the deposited energy.

With these values in hand and using the threshold levels from tables 2.3 and 2.4

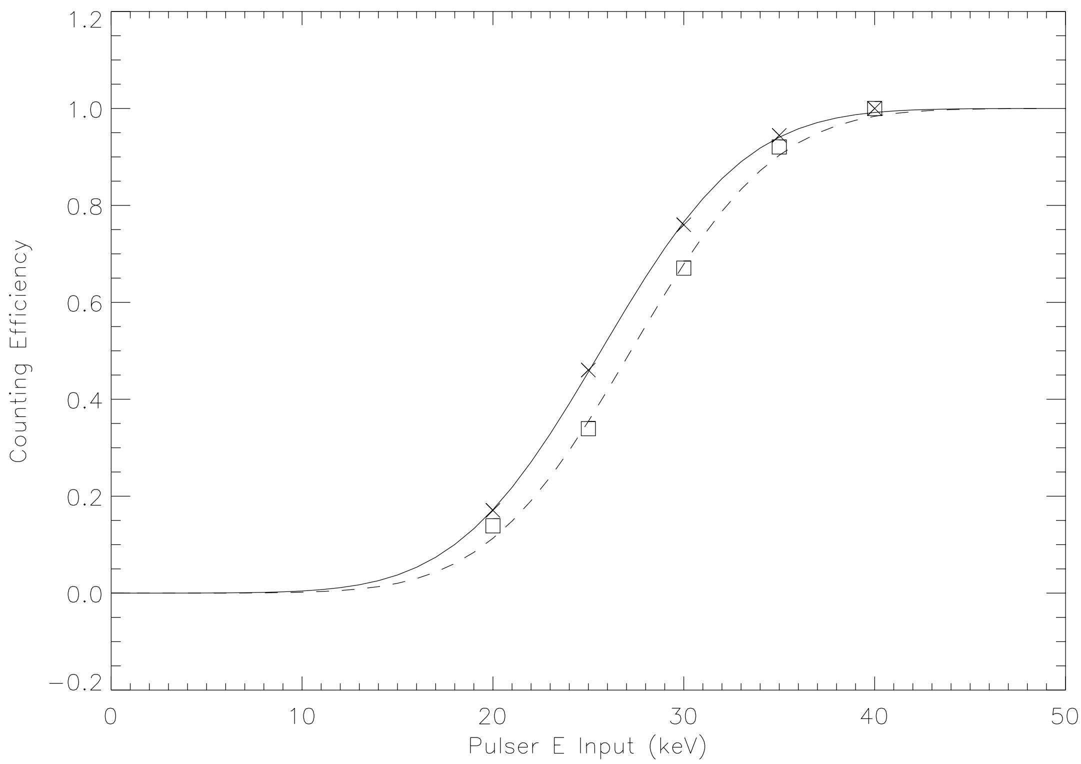

Figure 3.3: Fit of the complementary error function (eq. 3.1) to the pre-flight calibration data. Squares are for detector B, crosses for detector F.

is then possible to determine which channel a given particle would trigger on the detector.

One could think that since for most electrons nearly the whole energy is deposited in the detector, a few percent of outliers wouldn't have a big impact on the overall picture of the event. But, while it is indeed true that these effects don't affect the spectral profile of the event when one thinks in terms of fluence or close to the peak count rates, when it comes to calculate the onset of the event, these small variations actually have an important impact. As discussed in Haggerty and Roelof (2003), these few particles that get detected on the lower energy channels will give false onset timings at the instrument since — due to their higher energy — they are arriving

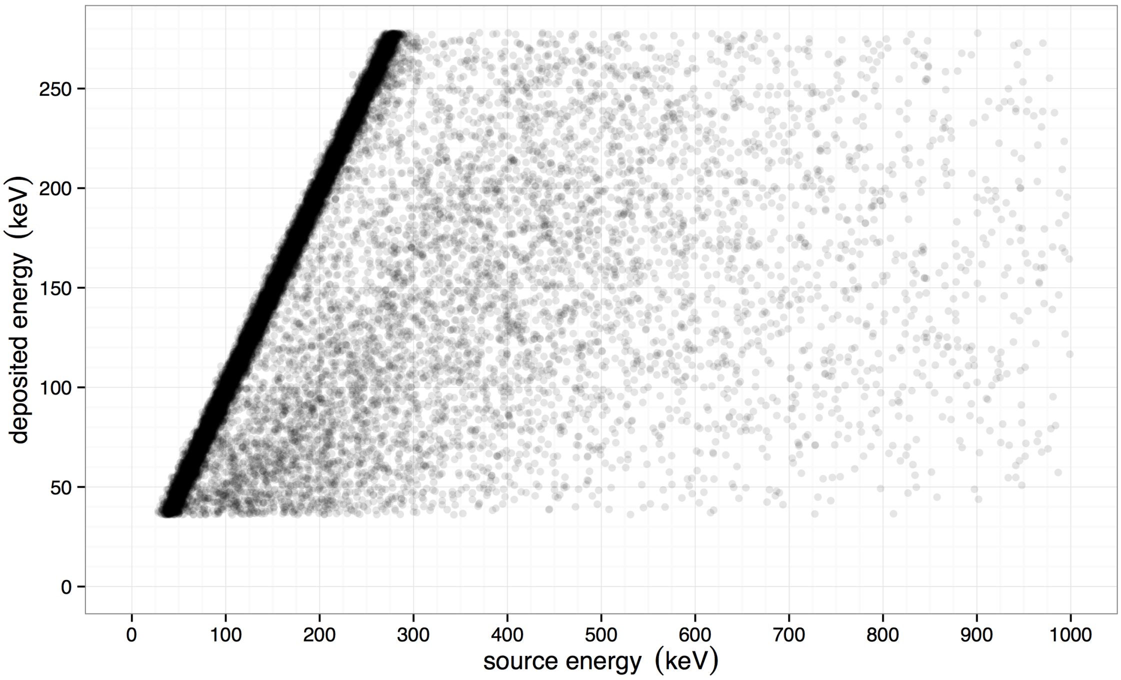

Figure 3.4: Detector response in the E1 to E5 range, obtained by applying the electronic effects to the Geant4 simulation.

before the rest of the event and triggering counts in the lower energy channels before those were expected to arrive. These spurious counts noise are not easy to remove given the poor statistics typical at most event onsets.

Another factor that has influence in the results, is that the effective collecting area of the detector, the geometrical factor, when it comes to the electron spectra, is not a fixed quantity but one that depends on the energy of the source. The geometrical factor (GF) is a quantity, traditionally used in the analysis of telescopes, that gives the theoretical efficiency of the instrument. But, being a purely geometric calculation, it does not take into account the properties of the propagation medium and the deflection it may exert in the kind of radiation we are trying to measure. Since we can use the virtual representation of the instrument in Geant4, a more interesting quantity to evaluate, is the efficiency of the response of the instrument, since it allows to immediately extrapolate the number of particles emitted from the number of detected particles, for an isotropic source that completely surrounds the instrument. In a perfect telescope that lets pass some kind of radiation in exactly the same way at all energies for given energy range, this should be equivalent to the GF, but as it was found out, in the LEFS channels of the HI-SCALE/EPAM the reality is different.

For an ideal telescope — whose efficiency for detecting particles of a given type is 1 in a given energy interval and 0 otherwise and where the detectors are mathematical surfaces with no thickness — the factor of proportionality relating the counting rate C to the intensity I is defined as the gathering power Γ of the telescope. When the source intensity is isotropic, i.e., $I = I_0$, the factor of proportionality G is called geometrical factor (Sullivan, 1972). That is:

$$C = G\, I_0 \tag{3.2}$$

In order to calculate the GF, the most direct — although computationally intensive — method to do so, consists in fully enveloping the instrument in a spherical shell, uniformly choose points across all its surface and in each of these points generate particles in each direction at uniform angles towards its interior (figure 3.5).

Excluding any time dependence on the source the counting rate will simply be the number of particles arriving at the detector N_C, while the intensity of the source also drops the time dependence and becomes the number of emitted particles N_E, divided by the surface area S, and the emission source solid angle Ω. Let S be the area of a sphere with radius R,

$$S = 4\,\pi\, R^2 \tag{3.3}$$

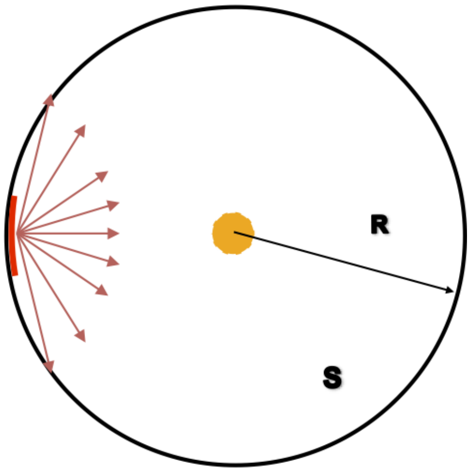

Figure 3.5: Computing the GF consists in surrounding the instrument with a spherical shell and then, in each point, generate particles in every direction, accounting for those that reach the detector.

while the solid angle comprised by the emission source is given by,

$$\Omega = \int_0^{2\pi} \int_0^{\pi/2} \cos\theta \; \sin\theta \, \mathrm{d}\,\theta \, \mathrm{d}\,\varphi = \pi \tag{3.4}$$

and as such the intensity becomes,

$$I_0 = \frac{N_E}{4\,\pi^2\,R^2} \tag{3.5}$$

and finally one obtains a simple expression that relates the particles arriving at detector vs the particles emitted by the source with geometrical factor:

$$G = \frac{N_C}{N_E}\,4\,\pi^2\,R^2 \tag{3.6}$$

The results for the GF relation with the energy of the source on the LEFS detectors, is shown in figure 3.6 where it can be seen that the GF is indeed dependent on the energy of the source.

By analyzing the direction of the electrons inside the detector and their deflection, this effect was found to be a side product of the aluminized parylene foil, placed

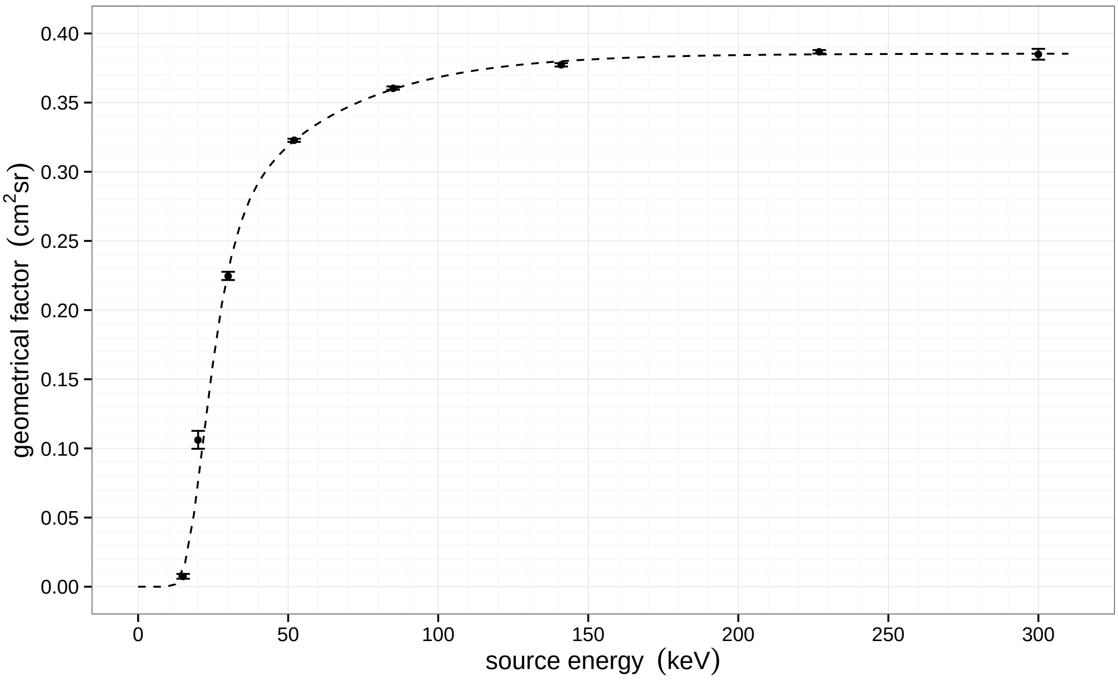

Figure 3.6: The Geometric Factor (GF) for electrons in the LEFS detectors, varies with the energy due to the presence of the parylene foil. For energies above 100 keV, the constant value for all energies of 0.397 $\mathrm{cm}^2\,\mathrm{sr}$ given by the literature is accurate, but for lower energies the GF quickly drops to very low values. See text for details on the simulation.

in front of the detector to stop the low energy ions while letting the electrons with energies above 30 keV pass freely. Although the electrons with energies above 30 keV did indeed pass trough the foil like it was expected, their trajectory was slightly altered depending on their energy, and a part of them would end up missing the detector, hence, the energy dependence on the GF. The values given for the GF by the instrument handbook are 0.397 $\mathrm{cm}^2\,\mathrm{sr}$ and are in perfect accordance with the value obtained by this simulation for energies greater than 100 keV, but, as can be seen it drops sharply for lower energies, well inside the nominal energy ranges of channels E1 and E2 thus having a great impact in the signal detected by them.

The GF results obtained, were then applied to the previous simulation results from

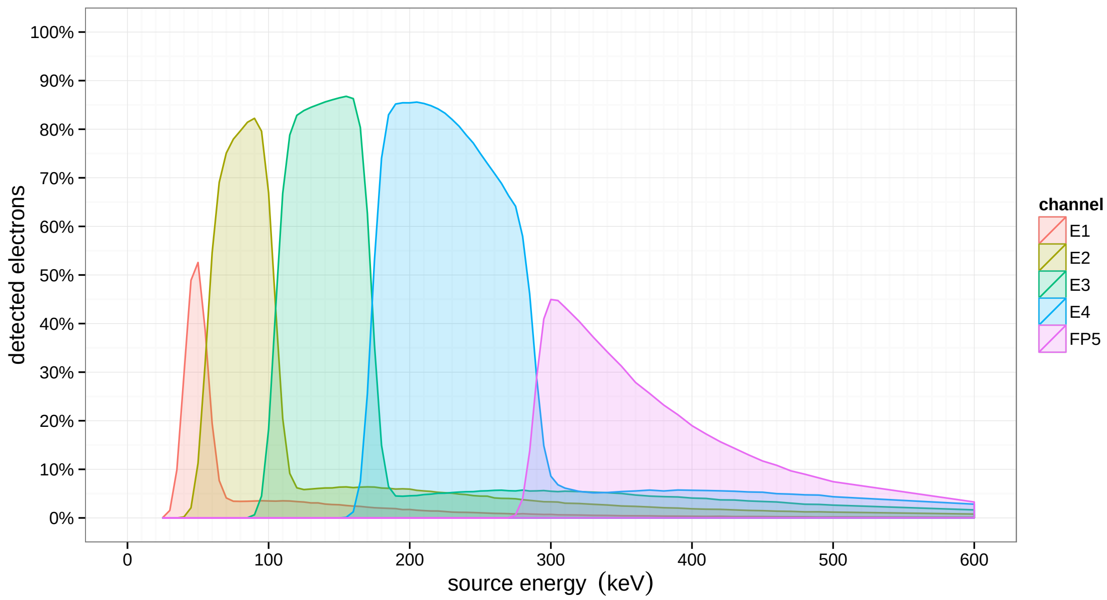

Figure 3.7: Rate of electrons detected per channel for the LEFS detectors. The lower energy channels are particularly sensitive to high energy electrons when compared to their energy ranges. This will introduce errors when calculating the onset times since the first particles arriving at the channel will actually come from particles belonging to the higher energy channels.

the energy beam directed normally at the F detector, by fitting the GF simulation results with a curve and applying them to that simulation data in post processing.

With these three effect accounted for (the scattering in the foil, the scattering in the detector and the electronics noise), is now possible to present a probabilistic model of the deposited energy in function of the energy of the source for each channel (figure 3.7). This gave a better perception about what was going on inside the detector, as it could finally be seen that there were big contributions from high energy electrons to lower energy channels. The channel E1', having a smaller energy range, was clearly affected by these issues, although not as greatly as E2', which actually explains why E2' is the first one signaling the arrival of SEP events in the LEFS60 detector. The detector scattering effects were already qualitatively discussed using

Monte Carlo methods in Haggerty and Roelof (2003) and Haggerty and Roelof (2006) where the nominal channels values were described. With more powerful computation methods available today it was possible for this thesis work to build upon that of Haggerty and Roelof (2003, 2006) and go a step further by using the noise effects together with the discriminator levels and by introducing the presence of the foil in the simulation. These new insights are specially important for the E1' channel where the energy dependence of the GF plays an important role in the energy deposition. After looking into these results, it cannot be assumed anymore that the instrument simply has a linear response to the input signal and — as it will be shown in Section 4.3 — this had a strong effect on determining the onset timings of SEP events on the electron channels.

3.3.1 Using the simulation results to estimate onset times using the average energy of the particles in the channel

In a timing study, one needs to be able to relate the time when the flux reaches a certain threshold — normally given as function of the signal to noise ratio or the particle detection rate at the peak of the event — with the time when the flux starts to rise above the pre-event value — the onset time. If there is a statistically significant amount of particles triggering each channel, then the time when the flux reaches that certain threshold and the time when the flux rises above the pre-event values will have very close values. But in the cases where the signal to noise ratio is poor, some corrections will be needed.

For a given event the shape of the flux versus time curve at a given energy will be determined by several factors: the injection function of the particles being detected — short pulse versus long duration and complex injection at the source; the propagation of the particles from the Sun to the spacecraft — pitch angle scattering, adiabatic focusing, presence of magnetic bottlenecks; and finally the ones intrinsic to the detector itself: width of the energy response, response factors related to the energy, angular directions being scanned.

For a very short delta-like injection function at the Sun, models using using a focus-transport approximation based on a scattering term from Kocharov et al. (1998), the rise of the flux curve for a mono energetic beam should be approximately linear from 1% up to 50% of the peak (Maia et al., 2007). Using this assumption, the onset calculation becomes quite simple since one needs only to calculate the time when the count rates subtracted from the background, reach a certain threshold t_1, the time when they reach exactly twice that value t_2, then calculate the time elapsed between them $\Delta t = t_2 - t_1$ and subtract that time from the lower threshold time in order to find the onset time $t_{onset} = t_1 - \Delta t$. It should pointed though, that this method introduces a bias in the timing calculations that must be taken into account in the final result. In Morgado et al. (2015); Morgado and Maia (2014) we present the method for estimating the value of this bias using Monte Carlo methods.

In the analysis of the 2012, May 17, SEP event as observed on the EPAM in Chapter 4, it shall be seen that the results, obtained by using the approach described in the paragraph above directly with the data obtained for the electron channels, are heavily influenced by particles with energies above the nominal values being detected in the lower energy channels. This, as expected will give similar onset times in every channel, thus defeating the purpose of the method which is to constrain the onset of the event at the Sun. By using the results obtained in the HI-SCALE/EPAM simulation summarized in figure 3.7, it is possible to calculate the expected average energy of the particles detected in any channel and as such identify the periods when counts are dominated by the spurious component.

This alternate analysis method needs a starting assumption, since it depends on an estimate of the flux coming from high energy particles to infer the spurious fraction in the readings of the low energy channels. Hence, the approach used was to use the highest energy electron channel as the starting point. Another aspect making this the most logical approach is that the geometrical factor is almost constant at higher energies. We describe in what follows the iterative process used to determine the average energy at any given particular instant for any given channel.

From the Geant4 simulation results described above, let the number of particles that for a given source energy E get detected in a given channel N, be given by $C_N(E)$. By using a power law expression of the form $P_\gamma(E) \propto E^{-\gamma}$ as an approximation to fit the spectra, the ratio R between the detected electrons emitted according to a simulated energy spectra with spectral index γ_N for a channel N and the channel $N+1$ is given by:

$$R = \int \frac{P_{\gamma_N}(E)\, C_{N+1}(E)}{P_{\gamma_N}(E)\, C_N(E)}\, \mathrm{d}E \tag{3.7}$$

Using a table constructed with eq. 3.7 and the real detected electron rates $O_N(t)$, as measured by the instrument for a channel N at any given time t, we now find the closest value for γ_N, so that:

$$\frac{O_{N+1}}{O_N} = R \tag{3.8}$$

Referring the expected number of detected electrons in channel N_a that comes from channel N_b energy range as $D_{N_b \to N_a}$, the contribution of detected electrons from channel N and higher energies to the channel with lower energy $N-1$ will be expressed as $D_{N \to N-1}$ and is calculated by constructing the approximate spectra for channel N by a power law with spectral index γ_N and by using C_N to calculate what part of it is indeed detected in channel $N-1$:

$$D_{N\to N-1} = \int\limits_{m_{N-1}}^{m_N} P_{\gamma_N}(E)\, C_N(E)\, \mathrm{d}E \tag{3.9}$$

where m_N is defined by the minimum energy at which 1% of the particles get detected in channel N.

We then obtain the number of electrons detected in channel $N-1$ coming from channel $N-1$ energy range expressed as $D_{N-1\to N-1}$, by subtracting the number of detected electrons in channel $N-1$ coming from channel N energy range expressed as $D_{N\to N-1}$, from the actual number of deposited electrons in channel $N-1$ expressed as O_{N-1}, that is reported by the instrument readings:

$$D_{N-1\to N-1} = O_{N-1} - D_{N\to N-1} \tag{3.10}$$

Calculating once again the spectral output for several spectral factors, in order to find γ_{N-1} using the energy range of channel $N-1$ and applying a normalization factor β such that:

$$P_{\gamma_{N-1}}(m_{N-1}) = \beta\, P_{\gamma_N}(m_N) \tag{3.11}$$

and choosing γ_{N-1} such that:

$$\int\limits_{m_{N-1}}^{m_N} P_{\gamma_{N-1}}(E)\, C_{N-1}(E)\, \mathrm{d}E = D_{N-1\to N-1} \tag{3.12}$$

it becomes possible to build a spectral curve S_{N-1} for the all range of the spectra and for any given channel $N-1$:

$$\begin{cases} S_{N-1}(E) = P_{\gamma_{N-1}}(E), & m_{N-1} \leq E < m_N \\ S_{N-1}(E) = P_{\gamma_N}(E), & m_N \leq E < m_{N+1} \end{cases} \tag{3.13}$$

and it becomes finally possible to calculate the average energy of a channel $N-1$ at any given time t expressed as $\overline{E_{N-1}}$:

$$\overline{E_{N-1}} = \frac{\int\limits_{m_{N-1}}^{m_{N+1}} S_{N-1}\, E \,\mathrm{d}\, E}{\int\limits_{m_{N-1}}^{m_{N+1}} S_{N-1} \,\mathrm{d}\, E} \tag{3.14}$$

In order to have an estimate for the error of the calculations, the all process described above was repeated by adding some noise to the input values according to a Poisson distribution with the degrees of freedom equaling the observed counts. From a large number of such determinations an average and a standard deviation were computed. From these any possible bias in the method and errors values were determined.

From these average energies one can then determine the periods when the counts in a given channel are dominated by the spurious contribution and when the counts begin to be dominated by electrons in the nominal energy range for the channel. Estimates for the onset times of the nominal electrons can then be computed easily. It is only needed to find the instant t_1 at which the $\overline{E_N}$ is inside the channel nominal range, as given by table 3.1, and the instant t_2 in which the number of counts in that channel is double of those in t_1 and then linearly fit those two points to obtain the onset time. As it will be seen, this approach offers a much clearer trend of the event progression, allowing for a better estimate of the onset timings.

3.4 The LEMS120 telescope

We focus on opening angles and spin-axis orientations of the LAN2A assembly, which are illustrated in the schematic in figure 3.8. In subsequent sections, we follow the notation from figure 3.8, using M' and F' to indicate the detector pair in LAN2A. This

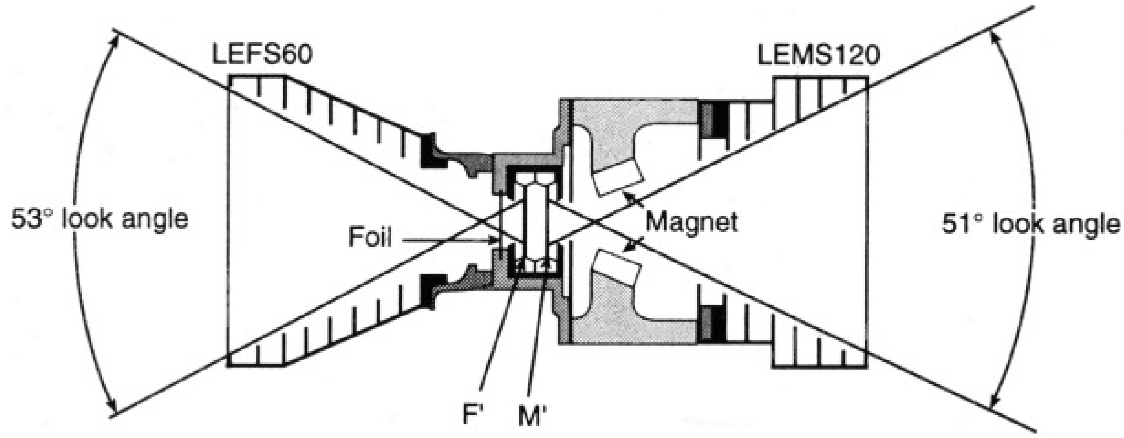

Figure 3.8: LAN2A assembly of the EPAM instrument, formed by the LEMS120 and LEFS60 telescopes.

Source: Gold et al. (1998)

detector pair consists of two equal 200 μm thick totally depleted circular silicon surface barrier detectors with 5652 μm radius. LEMS30 and LEFS150 form a similar assembly, but the behavior from LAN2B became erratic on EPAM following the Halloween ion events in 2003 (Haggerty et al., 2006) so we do not use those data. The LEMS120 telescope contains magnets designed to deflect electrons with energies higher than 300 keV away from the detector M'; ions are not deflected and are thus able to hit the M' detector. LEMS120 is thus essentially an ion detector with eight nominal energy channels designated from P'1 to P'8. We concentrate on only three of those channels P'2 (68–115 keV nominal energy range), P'3 (115–195 keV), and P'8 (1.9–4.8 MeV).

Discriminator	Energy (keV)	Noise (keV)
M'0	30	6
M'1	50	8
M'2	100	10
M3	180	10
M'7	1895	10

Table 3.2: Relevant EPAM LEMS120 discriminator levels.

LEMS120			LEFS60		
	Energy (keV)			Energy (keV)	
Channel	Lower	Higher	Channel	Lower	Higher
P1'	47	68	FP1'	362	375
P2'	68	115	FP2'	375	412
P3'	115	195	FP3'	412	460
P4'	195	321	FP4'	460	546
P5'	310	580			
P6'	587	1060			
P7'	1060	1900			
P8'	1900	4800			

Table 3.3: LEMS120, M' detector and LEFS60, F' detector, nominal energy channels for ions.

As discussed in Section 3.3 the LEMS/LEFS systems provide pulse-height-analyzed single-detector measurements with active anti-coincidence where energies deposited in the active silicon volume are assigned to a given channel according to discriminator levels set by the electronics. We refer to the discriminator levels for the M' detector as M'0 to M'7, ordered from low to high. Documentation available for HISCALE refers a value of 10 keV for the noise levels and this value is accurate enough for our purposes. The discriminator levels for LEMS120 on EPAM and associated noise are reported in reported in table 3.2; we determined values for the noise in M'0 and M'1 based on pre-flight calibration. Values for HISCALE discriminator levels differ only slightly.

The LEMS120 detector has 8 channels with nominal energies as given by the instrument handbook (Armstrong and Hunt-Ward, 1999) presented in table 3.3. These are complemented by the FP' ions channels from the F' detector for ions above 362 keV that are able to pass trough the foil, working in a similar way and for which the nominal energies are presented in table 3.3.[1]

[1]The M detector stopped working properly on the EPAM some time after it was launched, so for all

Still, the nominal energy range for the LEMS120 channels does not correspond to the actual energy deposited in the active silicon volume. Before reaching the silicon, particles need to cross a 184 nm thick aluminum contact. The energy lost in that contact is accounted for when defining the nominal energy range and as such the discriminator levels set by the electronics correspond to a deposition of energy in the detector slightly lower than the nominal energy values. The deposited energy value is important for the simulations we discuss later, rather than the nominal energy range.

The anti-coincidence implemented by the electronics is of paramount importance in understanding the counts given by EPAM and HISCALE (for a discussion applied to the electron channels see Haggerty and Roelof (2006)). The anti-coincidence defines the energy channel to which a given particle is assigned. As an example, a particle gives a count on P'1 if its energy deposited is enough to trigger M'0 but not M'1. This anti-coincidence also includes the response from the F' detector sitting in front of M'. A proton incident on M' in a near-perpendicular direction with energy above 4.8 MeV does not deposit the totality of its energy when traveling 200 μm of silicon so that it will give a nearly simultaneous response in F'; this anti-coincidence with F' is used to reject field of view ions with energies higher than 4.8 MeV.

3.4.1 Response to penetrating ions

From the LAN2A engineering drawings, we know that the lowest thickness of the stainless steel enveloping the detector chamber and the adjacent magnet chamber is about 0.09 inches, being substantially larger in the projections supporting the magnet. This means that protons of energies lower than about 35 MeV can only hit the detector if they are "field of view protons". Substantially higher energy protons should be able

purposes I'll just refer to the M' detector although the methodology would be exactly the same for the M detector.

to cross some of the thicker portions of the shielding, and even the material providing support and connecting LEMS120 to the rest of the instrument and to the spacecraft body.

The simplest case is to consider what happens at energies substantially higher than the cutoff given by the frame enveloping the detectors. When considering protons of sufficiently high energy, as will be that case for those in the GeV range, one can mostly ignore the energy loss in the iron frame and support structure and address only what will happen in the silicon; we take this approach here. We did the simulations of proton interaction with silicon using the Geant4 toolkit (Agostinelli et al., 2003). Although the average energy loss can be computed reasonably well using the Bethe-Bloch equation, a Monte-Carlo approach as that given by Geant4 allows us to look at the shape of the distribution of deposited energies.

We show in figure 3.9 the distribution of deposited energies for primaries of 5.3 GeV and 384 MeV for normal incidence on a 200 μm thick silicon waffle; the gray band marks the energy range corresponding to P'2. The shape of the responses illustrated in figure 3.9 shows a very prompt rise with increasing deposited energy followed by a long a tail. Channels P'2 and P'3 respond to high energy protons, overlapping substantially in their response to hundred MeV to GeV incident protons, while P'8 is essentially insensitive to that energy range.

Of course, for normal incidence, penetrating protons of large energy would hit both M' and F' and thus would be rejected by the active anti-coincidence mechanism implemented in LAN2A. As such, to be counted, high energy ions will need to reach the detector at oblique angles, thus traveling substantially more than for normal incidence. Since the deposited energy is roughly proportionally to the silicon distance traveled, the likelihood of being counted in a given channel will strongly depend on the direction that the proton comes from. We have included this effect in the simulations and discuss it next in Chapter 4 when presenting the 2012 May 17 event.

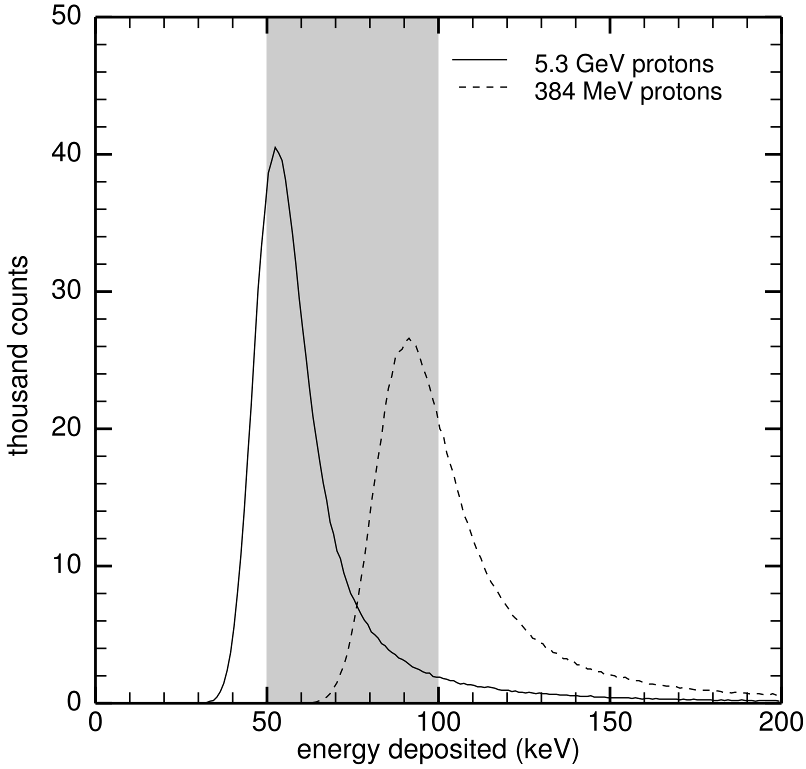

Figure 3.9: Results from Monte Carlo simulations showing number of particles versus deposited energy for two incident proton energies. A million protons were simulated at each energy, propagating parallel to the detector normal and impacting the center of the detector; the gray band marks the energy range corresponding to P'2.

Bibliography

Agostinelli, S., Allison, J., Amako, K. e., Apostolakis, J., Araujo, H., Arce, P., Asai, M., Axen, D., Banerjee, S., Barrand, G., et al. (2003). Geant4—a simulation toolkit. *Nuclear instruments and methods in physics research section A: Accelerators, Spectrometers, Detectors and Associated Equipment*, 506(3):250–303.

Allison, J., Amako, K., Apostolakis, J., Araujo, H., Dubois, P. A., Asai, M., Barrand, G., Capra, R., Chauvie, S., Chytracek, R., et al. (2006). Geant4 developments and applications. *Nuclear Science, IEEE Transactions on*, 53(1):270–278.

Armstrong, T. and Hunt-Ward, T. (1999). Ulysses hiscale data analysis handbook, internal document. *Fundamental Technologies*.

Gold, R., Krimigis, S., Hawkins III, S., Haggerty, D., Lohr, D., Fiore, E., Armstrong, T., Holland, G., and Lanzerotti, L. (1998). Electron, proton, and alpha monitor on the advanced composition explorer spacecraft. *Space Science Reviews*, 86(1-4):541–562.

Haggerty, D. and Roelof, E. (2003). Electron scattering in solid state detectors: Geant 4 simulations. *Advances in Space Research*, 32(3):423–428.

Haggerty, D., Roelof, E., Ho, G., and Gold, R. (2006). Qualitative comparison of ace/epam data from different detector heads: Implications for noaa rtsw users. *Advances in Space Research*, 38(5):995–1000.

Haggerty, D. K. and Roelof, E. C. (2006). Effectiveness of anti-coincidence in electron detectors: Implications for beam-like electron events. *Advances in Space Research*, 38(5):990–994.

Kocharov, L., Vainio, R., Kovaltsov, G., and Torsti, J. (1998). Adiabatic deceleration of solar energetic particles as deduced from monte carlo simulations of interplanetary transport. *Solar Physics*, 182(1):195–215.

Lanzerotti, L., Gold, R., Anderson, K., Armstrong, T., Lin, R., Krimigis, S., Pick, M., Roelof, E., Sarris, E., and Simnett, G. (1992). Heliosphere instrument for spectra, composition and anisotropy at low energies. *Astronomy and Astrophysics Supplement Series*, 92:349–363.

Lindström, G. (2003). Radiation damage in silicon detectors. *Nuclear Instruments and Methods in Physics Research Section A: Accelerators, Spectrometers, Detectors and Associated Equipment*, 512(1):30–43.

Maia, D. J. F., Gama, R., Mercier, C., Pick, M., Kerdraon, A., and Karlickỳ, M. (2007). The radio-coronal mass ejection event on 2001 april 15. *The Astrophysical Journal*, 660(1):874.

Morgado, B., Filipe Maia, D. J., Lanzerotti, L., Gonçalves, P., and Patterson, J. D. (2015). The low energy magnetic spectrometer on Ulysses and ACE response to near relativistic protons. *A&A*, 577:A61.

Morgado, B. and Maia, D. (2014). Electron scattering profile of the epam experiment on ace. analysis of the electron event associated with the 2012 may 17 gle. *Astronomy and Astrophysics, in press.*

Nikitin, A. V., Davidchack, R. L., and Armstrong, T. P. (1997). Many-fold coincidence pileup in silicon detectors: Solar x-ray response of charged particle detector systems for space. *Nuclear Instruments and Methods in Physics Research Section A: Accelerators, Spectrometers, Detectors and Associated Equipment*, 386(2):431–438.

Peltola, T. (2014). Charge collection efficiency simulations of irradiated silicon strip detectors. *Journal of Instrumentation*, 9(12):C12010.

Sullivan, J. (1972). Erratum: Geometrical factor and directional response of single and multi-element particle telescopes, nucl. instr. and meth. 95 (1971) 5-11. *Nuclear Instruments and Methods*, 98:187.

Wüest, M., Evans, D. S., and von Steiger, R. (2007). *Calibration of particle instruments in space physics.* ISSI, The International Space Science Institute.

Chapter 4

EPAM's near relativistic proton & electron response

Contents

In this chapter we will make a detailed analysis of the response of the LEMS spectrometer onboard ACE to relativistic protons during the ground level solar cosmic ray event which took place on 2012 May 17. This was a Ground Level Enhancement (GLE) event, which represent the most energetic class of Solar Energetic Particle (SEP) events.

The event was observed in a wide range of wavelengths and detectors. NOAA reported a long-duration M5.1 X-ray flare at 01:25–02:14 UT with an active region located at (N11, W86) (see figure 4.1).

Li et al. (2013) reports on the electron and proton timings of the event putting forward the release time of 01:29 ± 00:01 UT for electrons and a release time of about

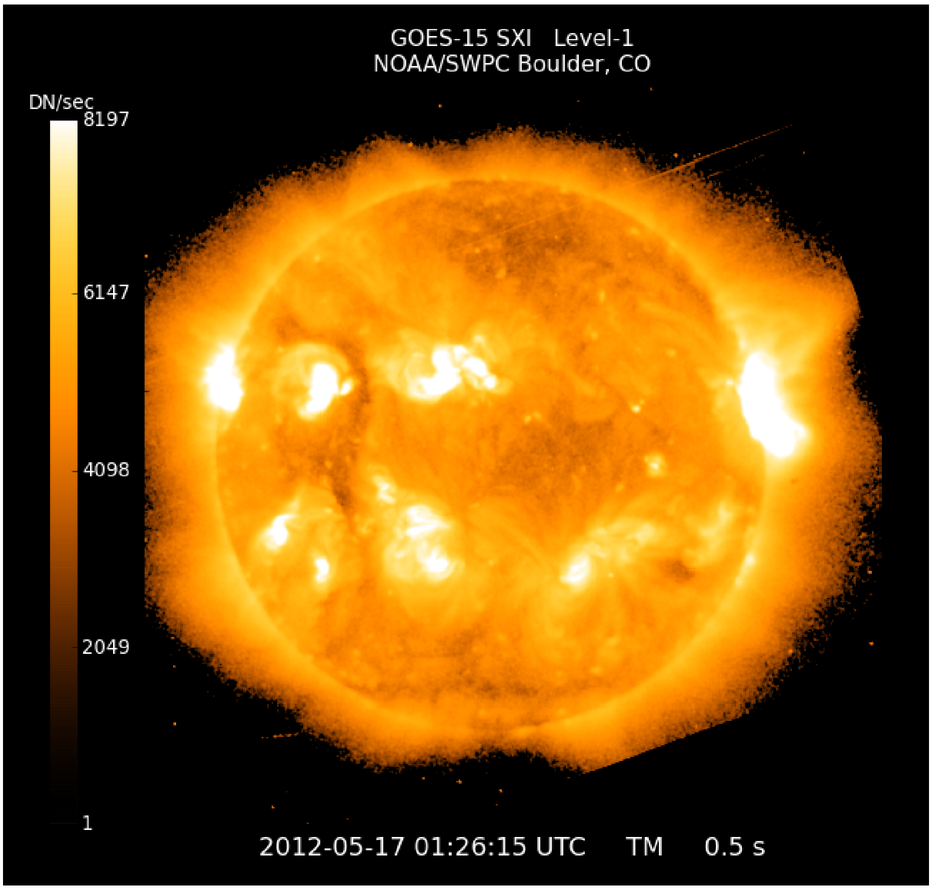

Figure 4.1: The flare as seen in GOES Solar X-ray Imager taking place in the western limbo of the Sun.
Source: National Centers for Environmental Information (NOAA)

10 minutes later for protons. Mishev et al. (2014) reports on the GLE associated event and its spectra and anisotropy dependence with time. In figure 4.2 it can be seen the increase relative to the background rates caused by the event, as detected by several neutron monitor stations. Shen et al. (2013) uses coronagraph observations by SOHO/LASCO, STEREO-A/COR1, and STEREO-B/COR1 identifying two eruptions resulting in two coronal mass ejections (CMEs) that occurred in the same active region and close in time and proposing a "*twin CME*" scenario for the SEP's origin.

By applying new data treatment methods allowing the use of "*out of nominal*

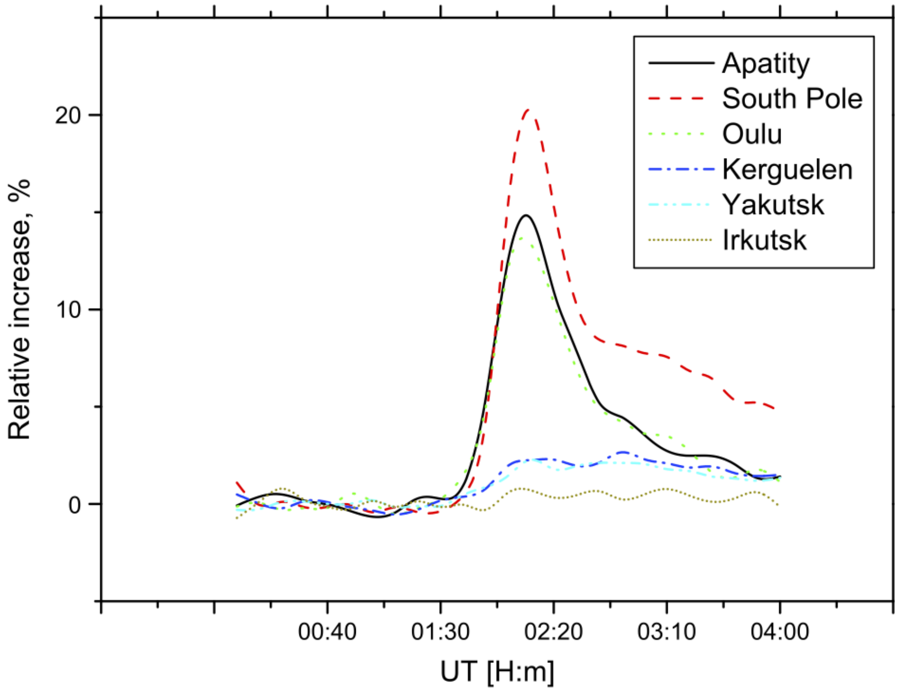

Figure 4.2: NM count rate enhancement for several NM stations during GLE 71 on 17 May 2012.

Source: Mishev et al. (2014)

passband" response of the telescopes that comprise the EPAM — an effect that's due to high energy particles penetrating through the instrument frame and giving "*spurious*" counts — we were able to further expand the data about this GLE event into the hundreds of MeV when it comes to the detection of protons, something no other instrument was able to do. For that purpose, we first characterized the instrument out of nominal passband response using Monte Carlo techniques and a model of the EPAM and HISCALE particle telescopes, and then we analyzed the GLE of solar cycle 24, on 2012 May 17, to show that EPAM's response is consistent with the detection of protons of solar origin with energies about 1 GeV. This kind of information generally has only been available from ground instruments like neutron radiation monitors.

4.1 Modeling the response for 2012 May 17 event

To illustrate LEMS120 response, including effects of directivity, we consider a very strongly anisotropic case, assuming that all particles are aligned with the magnetic field direction. This is close to the situation expected at the onset of an event of solar origin. We chose the direction the interplanetary magnetic field had relative to EPAM on 2014 May 17 at 02:00 UT — the results would have changed change very little if we had taken the magnetic field direction an hour before or later. We then simulated the rotation of the spacecraft and divided the spin period into eight identical intervals (sectors), mimicking the way data are gathered for LEMS120. We then simulated the instrumental response to protons of energies from 50 MeV to 5 GeV released uniformly in time; the same number of protons were modeled at each energy.

The simulation details very closely follow the procedure that is used to determine geometrical factors for particle telescopes. We generate proton coordinates randomly following a distribution uniform on the surface of a sphere. The dimensions of the sphere chosen were big enough to encompass both F' and M'. Each test proton was then followed assuming they were initially propagating along a linear trajectory following the interplanetary magnetic field direction. We did simulations of proton interaction with silicon using the Geant4 toolkit. We then computed the deposited energy for each particle, and we attributed a channel to the particle using the values for the discriminator levels and noise given in table 3.2 we included the effects of anti-coincidence with F'. The results from the simulation allow the computation of a geometrical factor. To do so, we merely take the number of "test particles" that are assigned to the channel, on the basis of deposited energy, and divide that by the number of test particles that were emitted, multiply by the area of the sphere they

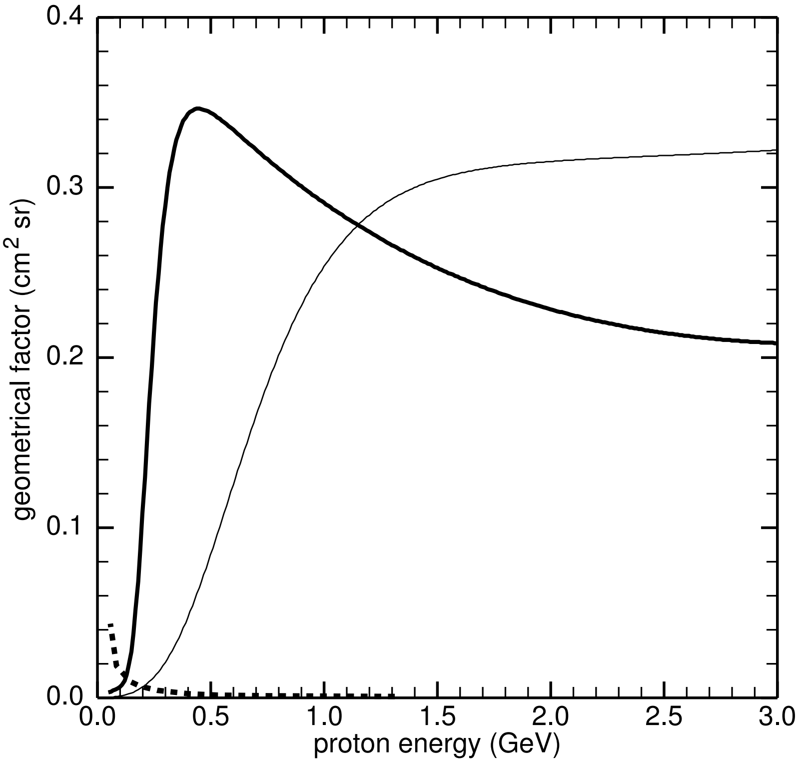

Figure 4.3: Results from Monte Carlo simulations of protons hitting M', showing the relative response, under the form of geometrical factors, of channels P'2 (thin full line), P'3 (thick full line), and P'8 (dashed line).

were emitted from and finally multiply by 2 (since half of the emitted particles would move outward from the sphere).

The results of the Monte Carlo simulations are shown in figure 4.3. While P'8 has a response to incident proton energies dropping sharply with increasing energy, with only residual sensitivity below 100 MeV, channels P'2 and P'3 show increased response at much higher energies. One of the important features in figure 4.3 is that P'2 response exceeds P'3 only for energies higher than $\sim$1 GeV. Penetrating protons with primary energies sufficiently close to the cutoff provided by the instrument frame have a much wider range of directions available for positive detection since they might end up with energies low enough to enable full deposition in M'. This is a considerably more complex problem, since the geometry of the full assembly, including part of the spacecraft, needs to be considered. We do not pursue this further, although we note that 35 to 100 MeV protons should be very important for defining the P'8 response.

We did not try to compensate for the question of instrument degradation with time, which can be a serious problem for particle telescopes based on solid state detectors as discussed by Wüest et al. (2007). Irradiation by 10^{12} to 10^{13} protons per centimeter square already cause damage to silicon detectors, and there is significant degradation after fluences of 10^{14} to 10^{15} protons per centimeter square: the detector efficiency may drop by a factor of 2 (Peltola, 2014), and the noise levels may increase in such a way that the lowest channels discriminators become unusable. Total fluence in LEMS120 on EPAM since the mission start is about 10^{12}, so the level of degradation should be relatively minor. We note nonetheless that — as discussed in Haggerty et al. (2006) — the noise levels in P'1 on EPAM are indeed rather high and the counts often show a considerable number of spikes; we avoid using P'1 in the analysis that follows.

4.2 EPAM proton observations of the 2014 May 17 event

A very thorough paper describing neutron monitor observations for the 2012 May 17 GLE is presented in Mishev et al. (2014) and we used results from that work extensively. In particular, Mishev et al. (2014) provide rigidity spectra for several periods during the event. We use the earliest time interval provided (from 02:00 to 02:10 UT) since at that time the pitch angle distribution should show the strongest anisotropy. For particles propagating close to the magnetic field direction we can then use the relative response of channel P'2 given in figure 4.3 to infer the expected count rates for that particular channel. We choose P'2 since it only shows a significant response for protons above 500 MeV, so that it is less affected by energy loss in the detector frame, something that we have not modeled. Neutron monitor data and the geometrical factor obtained from the model response of P'2 suggest that we should observe an average of 10 counts per second in P'2 from 02:00 to 02:10 UT — and half of those counts should be due to protons with energy above 1 GeV. Data from EPAM LEMS120 for the period 00:00 to 01:30 UT, which is before the GLE is seen by neutron monitors, show about 5 counts per second, and as such the expected 10 counts per second associated with the GLE should show in P'2 data.

Figure 4.4 shows the observed counts in P'2 integrated 144 seconds versus the observed counts in P'3 and P'8 (scaled so that they peak at about the same value). We subtracted the pre-event data. The fact that P'2 and P'3 very nearly show the same behavior is quite striking, as shown in figure 4.4. A simultaneous rise in the flux would not be enough to support the assumption of penetrating protons, since that could be explained by the spacecraft suddenly entering a region in space with higher pre-event fluxes. The different behavior in P'8, rising later than the channels that we know are more sensitive to higher energy penetrating ions (P'2, P'3), is a much stronger hint at the possibility that those counts are due to high energy protons. The value observed for P'2 (average of 10 counts per second between 02:00 and 02:10 UT) is consistent with that expected from NM data. Finally, the relative normalization, with P'2 counts roughly 1.5 times higher than those seen for P'3, is exactly what we would expect if those counts were dominated by protons with energies exceeding 1 GeV. We thus have strong evidence that P'2 and P'3 response extends to GeV energies and that those energies contribute significantly to the observed count rates.

The LAN2A telescopes use the spacecraft rotation to define eight look angles (sectors). For "*field of view particles*" entering through the aperture, the angle between the magnetic field and the detector normal corresponds to the pitch angle of arriving

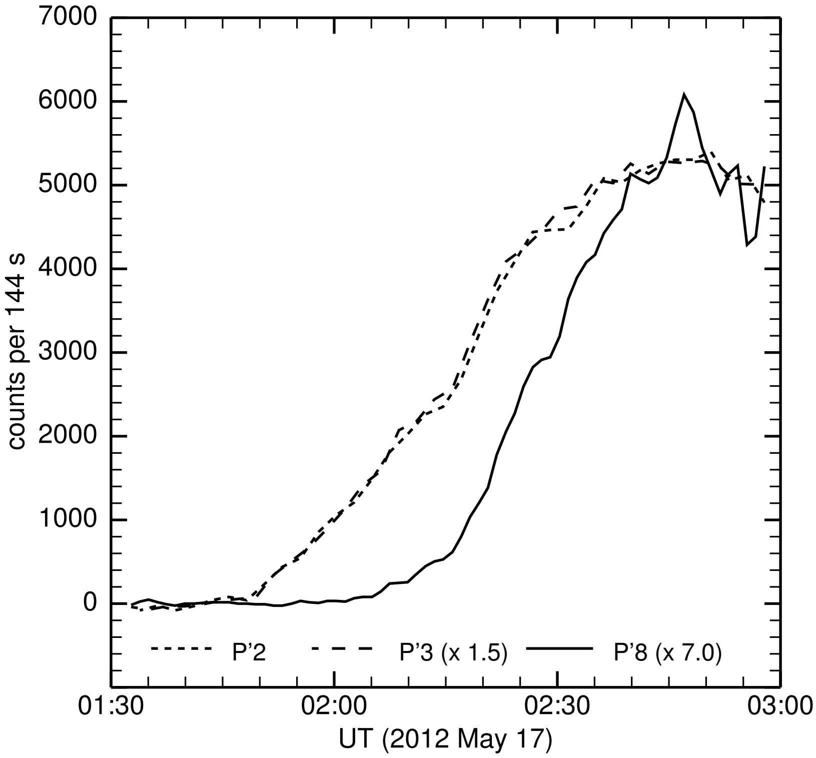

Figure 4.4: Comparison of the counts from the LEMS120 P'2, P'3, and P'8 counts for a 144 second integration. Counts from P'3 and P'8 have been scaled so that the peak counts for all channels are at equivalent levels.

particles in each sector. Figure 4.5 (left) shows the pitch angle distributions measured for 300 keV electrons in LEFS60. The flux is strongly anisotropic and clearly peaks at the look angles corresponding to particles coming from Sun along a Parker spiral. A similar process is also seen for ions in LEMS120 after 04:00 UT, the time at which we expect the arrival of solar ions traveling from 6 to 10% of the speed of light (1874 to 4752 keV protons). As seen in figure 4.5 (right), the P'8 energy channel at 04:42 UT time shows very marked anisotropy consistent with a beam-like solar event. So we do see the signature of the solar event, as expected for nominal channel energies.

As shown in figure 4.6, things are very different for the early rise seen in the LEMS120 data. From the 02:10 UT flux versus direction plots in figure 4.6, one can

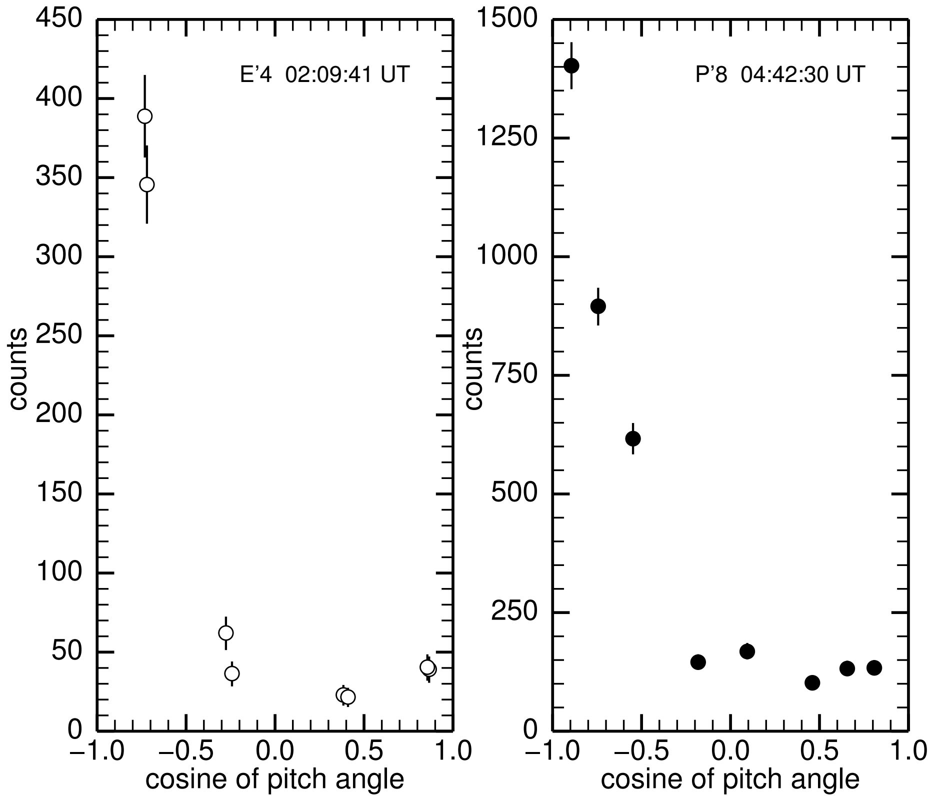

Figure 4.5: Pitch angle distributions for the event. (left) Electrons with energies about 300 keV show very marked beam-like pitch angle distributions. (right) At a time consistent with the arrival of protons in the nominal energy range, P'8 shows also a very marked excess in count numbers from the sector corresponding to particles coming from the solar direction.

see that the angular distribution of counts in both P'2 and P'8, although anisotropic, is nearly symmetric. Since we know the magnetic field, we can model the angular response from the detector expected for penetrating protons of different energies and compare it directly with EPAM data. This is shown by the dashed lines in figure 4.6. We assume that the protons are fully field aligned, as expected for the onset of a solar event, and we normalize the model to equal the total of the observed counts. To match the simulation results to observations, we had to assume that counts are dominated by particles higher than 1 GeV for P'2 and by less than 50 MeV for P'8; the agreement is then remarkable. Considering energies below 1 GeV for P'2 and above 50 MeV for P'8

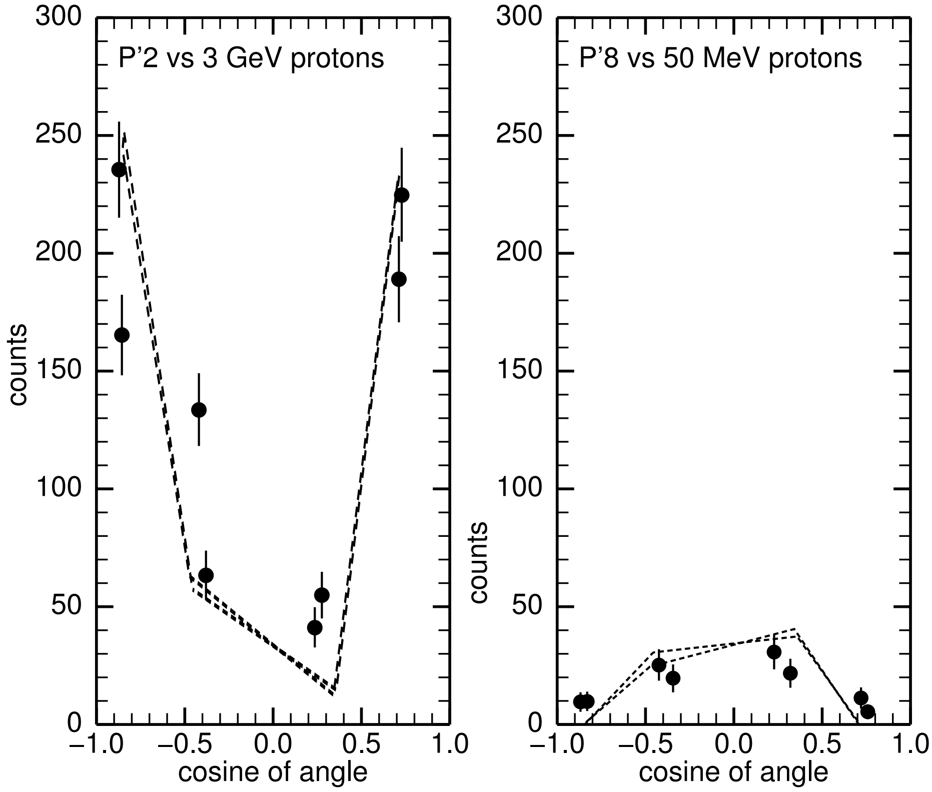

Figure 4.6: Counts as a function of the angle between the magnetic field and the normal to the M'. The dashed line joins adjacent sectors, that is, marks the progression in time from sector to sector and is a model curve obtained from Monte Carlo simulations of the detector response for field aligned protons. (left) Model versus observation for P'2 measures, 2 minute integration around 02:09:41 UT. (right) Model versus observation for P'8 measures, 10 minute integration after 02:09:41 UT.

significantly reduces the agreement between model response and observed directional counts. Figure 4.6 is again direct evidence that we are seeing penetrating protons, and the counts in P'2 are in great part due to protons with kinetic energies higher than 1 GeV. We note also that figure 4.6 being strikingly different from figure 4.5 discards one possibility that we had not yet addressed: the counts in LEMS120 might simply be due to contamination from high energy electrons that suffer less deflection at the magnets, and thus are able to reach M'.

4.3 EPAM electron observations of the 2014 May 17 event

Figure 4.7 shows a view of the 2012 May 17 event as seen by the electron channels of the LEFS. As can be seen, specially in channel E1' and E2' the first particles arriving at the detector have energies much higher than the channel nominal energy range. If one were to use these nominal ranges as the real energy of the electrons it would give different onset times and in fact all the channels would appear to have an onset occurring at very similar times. This effect is only relevant in the early rise of an event that has a very hard spectra. For most purposes the instrument performs rather well according to its energy channel range, is only when it comes to calculate the onset timings of hard SEP events like the one in 2012, May 17 that we need to take our analysis further.

By applying eq. 3.14 to the event data in order to estimate the average energy of the particles arriving at a channel N at any given time, we get a picture on how the average energy on each channel progresses with the event as shown in figure 4.8.

If we now apply the same method described in Subsection 3.3.1 to find the onset of the event using the average energy presented in figure 4.8 and finding the best fit for a curve with a slope given by the expected Parker spiral path length for this event, it is now possible to get an estimate of the event onset at the Sun as presented in figure 4.9. As discussed in Morgado and Maia (2014) the method wields results that follows the expected electron onset times in every channel by calculating their path length from the Sun and it is in very close accordance both with neutron data (Gopalswamy et al., 2013) gathered by the OULU observatory and with ion data collected by the EPAM, WIND and GOES (Morgado et al., 2015; Shen et al., 2013; Maia and Morgado, 2014).

In figure 4.9 we can see the results from applying basically the same method, with

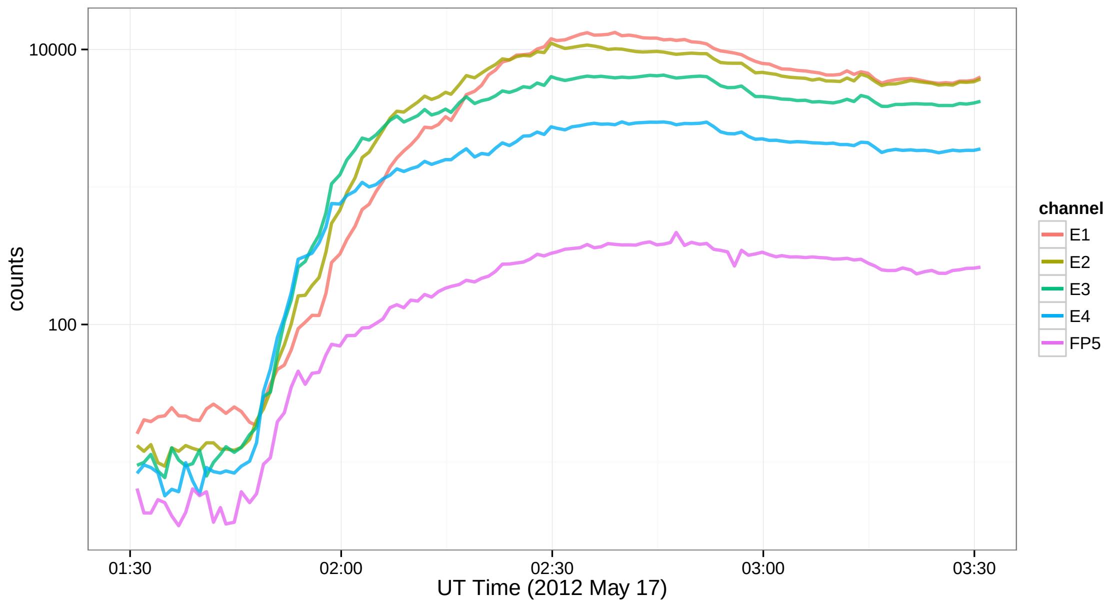

Figure 4.7: Original event as detected by the EPAM. The 12 second data was used and then integrated over a period of 1 minute in order to minimize the noise. As can be seen, it is difficult to find a clear distinction between the onset of the 3 lower energy channels since their flux rises above the background noise practically at the same time and even before channel E4 which was supposed to arrive earlier. This will make it impossible to correctly calculate the onset time of the event at the Sun.

the difference that in this case we assume the average energy of the particles within a channel to be a fixed quantity, assumed as the centre of the channel. As can be seen, we have very similar arrival times in all the channels, which makes it impossible to constrain the release back at the Sun time of the event, and to determine the possible source region of the event, being the motives, the ones already discussed in Subsection 3.3.1.

Another way to further validate the method is to analyze as the onset timing in each channel changes as the event progresses. Like it was said before, in the beginning of an event a channel is detecting electrons with energies above that channel nominal range, but as the time progresses it is expected for the calculated onset to be consistent with

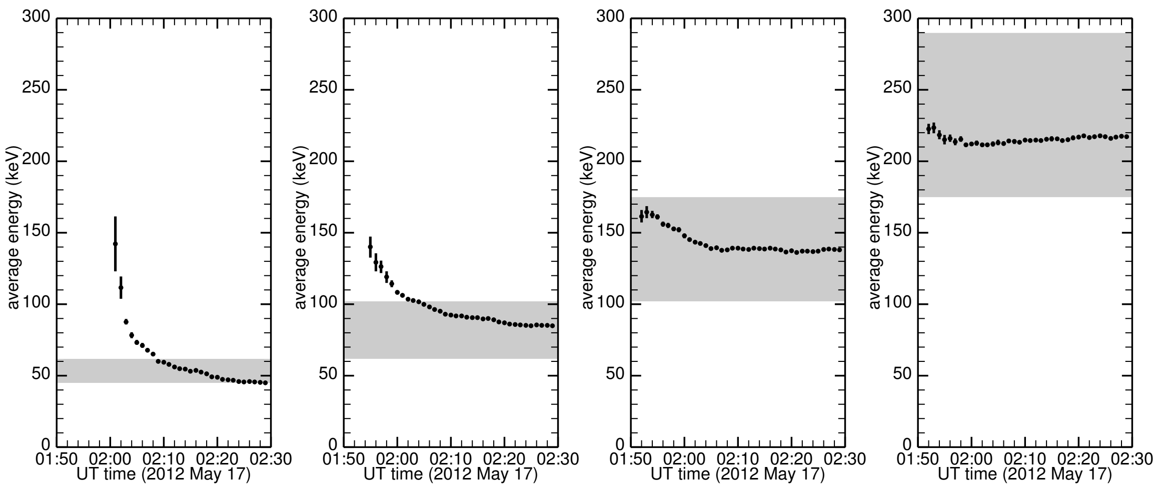

Figure 4.8: Reconstructed average energy of the particles during the event progression from the E'1 channel (leftmost) to the E'4 channel (rightmost). We can see that in the beginning of the event the lower energy channels are detecting energies much higher than their nominal energy range. There is an uncertainty on the actual energies they are detecting, but, by using this method the timings can be pinpointed more accurately by finding the actually time in which the energies of the particles from the event are actually inside a given channel nominal energy range. The higher energy channels are only slightly affected by this effect.

the extremes of the channel nominal values, since the particles with energies higher than the channel nominal range already passed beyond the telescope and after that moment the errors introduced by the energy degradation of the electrons are no longer present.

In figure 4.10 and figure 4.11 it becomes apparent that the onset timings calculated by this method are indeed consistent with a period of the event when the particles above the channel nominal energy already passed trough and when the particles with nominal energies within the range of the channel are actually arriving. As expected, channel E1' due to its very narrow energy range and channel E2' due to the being the most affected by the contamination of the low energy electron channels from high energy electrons, are the channels showing a greater impact from this effect. Channels E3' and E4' are almost impervious to this since their contamination effects are quite

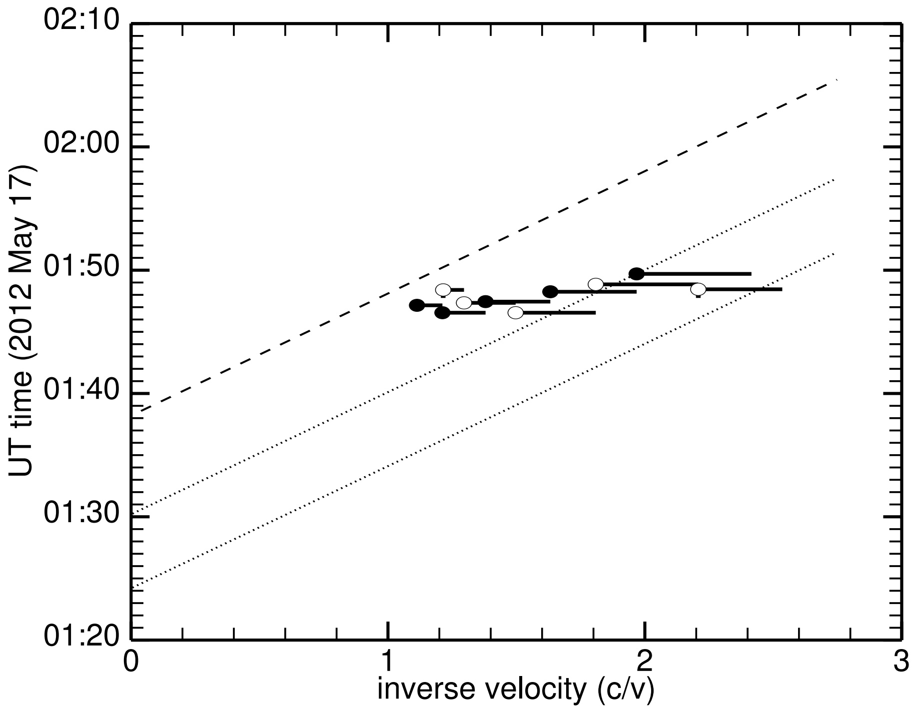

Figure 4.9: Onset time determinations of the 2017 May 17 event for the 5 LEFS60 channels (empty) and also for the 5 highest energies of the electron channels of the WIND/3DP experiment (full). The three lines show the arrival times expected for nearly scatter-free particles propagating from the Sun if they left the Sun at the same times as the ions, or if they left the Sun at the time when solar type III bursts are observed in the hectometric wavelength range. The solar wind velocity for this period was taken from the ACE SWE experiment data and found to be on average 362.40 km/s, giving us a spiral length path of 1.20 AU.

low and using this method to reconstruct the arrival c/v curve for the LEFS60 electron channels gives us the result presented in figure 4.12 which contrast with the values obtained by the method used in figure 4.9.

4.4 Threshold times and onset times

When looking into the timing of an in situ particle event one needs to distinguish between the time at which the event reaches a given threshold in the count rates, which are typically given as a function of signal-to-noise ratio or percentage of peak

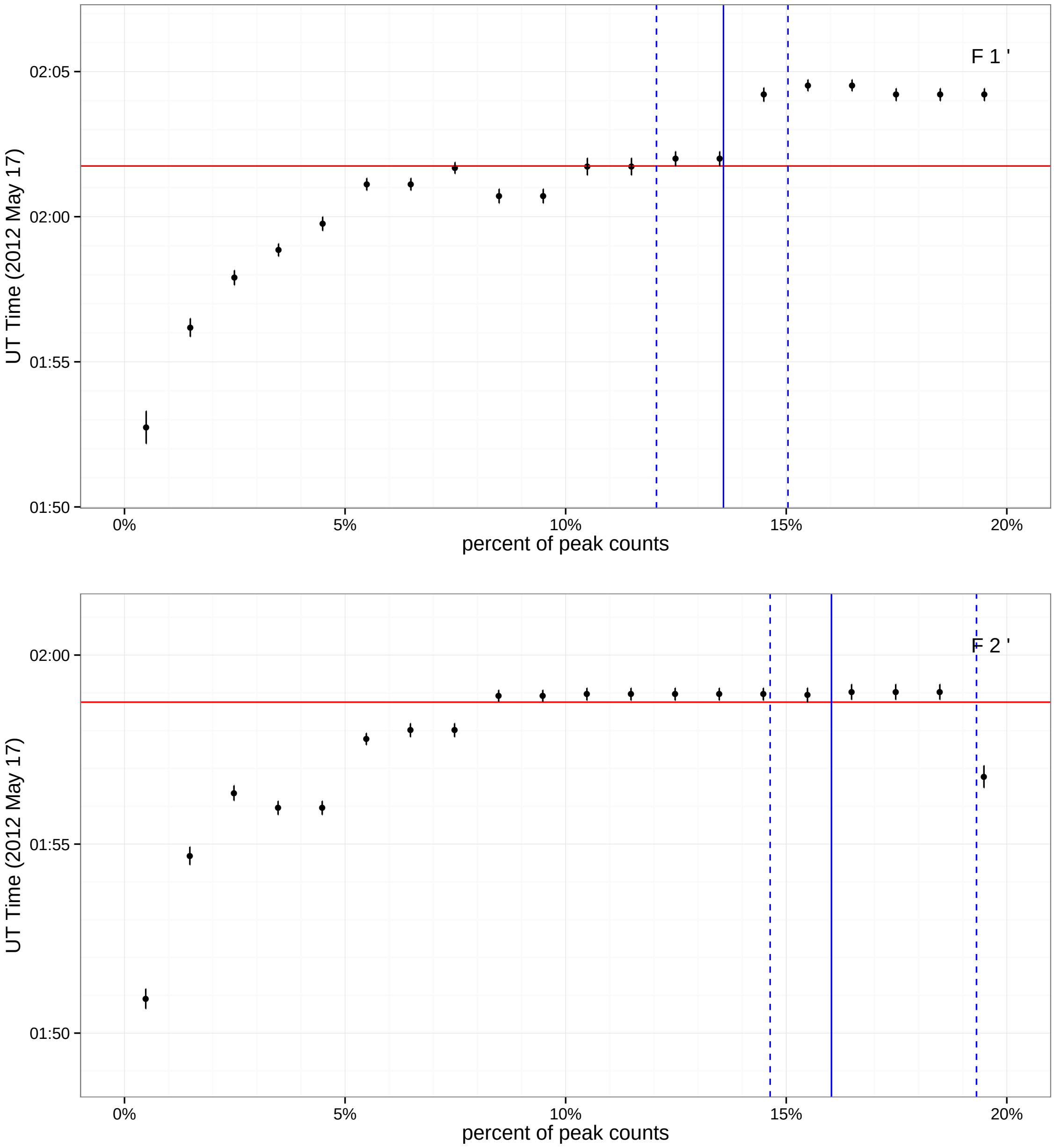

Figure 4.10: Onset timing progression for F1' (top) and F2' (bottom) according to the point chosen to calculate it linearly fitting the flux. In red we have the onset obtained with the average energies method presented in this thesis. In blue, the instant at witch the calculated average energy enters the nominal energy of the channel with an interval of 1 min given by the dashed blue lines.

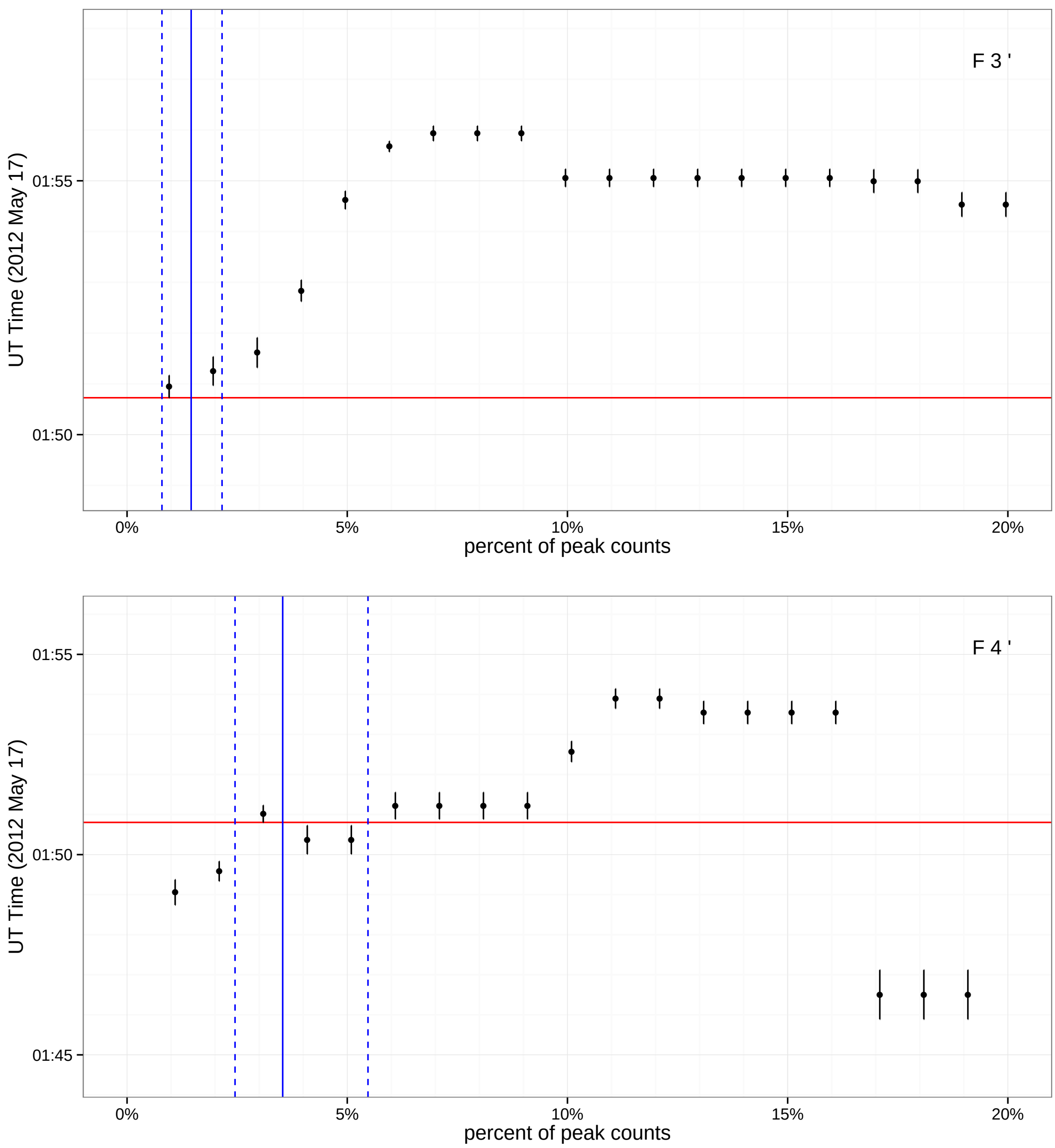

Figure 4.11: Onset timing progression for F3' (top) and F4' (bottom) according to the point chosen to calculate it linearly fitting the flux. In red we have the onset obtained with the average energies method presented in this thesis. In blue, the instant at witch the calculated average energy enters the nominal energy of the channel with an interval of 1 min given by the dashed blue lines.

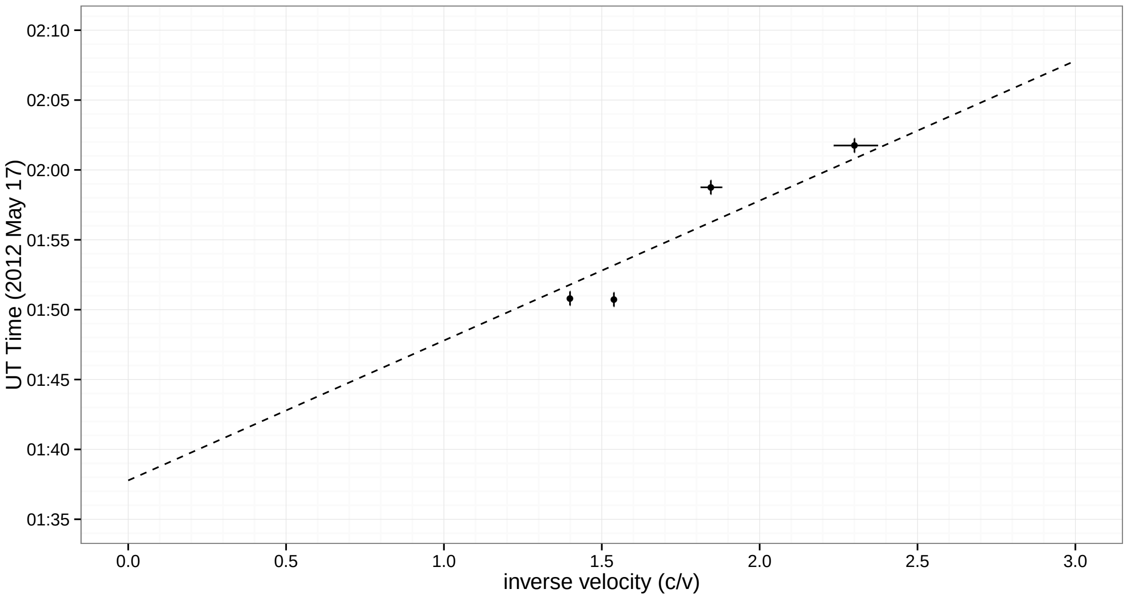

Figure 4.12: Inverse velocity (c/v) curves for the 2012 May 17 event calculated by using the average energy of each reconstructed channel. The dashed line indicates the expected slope taking into account the Parker spiral path length of the electrons, which can be seen to follow closely the results obtained by the method presented in this thesis. Moreover as explained in the text, the calculated onset time at the Sun by this method is further validated by the onset time found for neutrons and ions of the same event as seen by other instruments.

counts, and the time when the flux would have been seen starting to rise above the pre-event value in the absence of noise (the onset time). For "*strong*" events, when the threshold is a small fraction of maximum (less than 1%), corrections generally are not very relevant and the onset time can be assumed to be equal to the threshold time.

For many events, threshold times can only be readily computed from the available data at significant fractions of peak counts (10 to 20%) and inferring onset times require some assumptions regarding the shape of the rise in the count rates. Many factors affect this shape. Some of these factors relate to the acceleration and release of particles (short pulse versus complex injection at the source), others to propagation effects (pitch angle scattering prolongs the arrival of particles), and some are intrinsic to the instrument making the detection (look angles being sampled, range of energies being included in the same channel).

Propagation effects from the Sun to the Earth can be modeled using a focused transport approximation (Roelof, 1969). For a very short injection (delta-function like) with the methods described in Maia et al. (2007), based on a scattering term from Kocharov et al. (1998), we have verified that the rise should be approximately linear from 1% up to 50% of the peak. A linear rise allows for a straightforward way to relate the onset time with the threshold time: one needs only to determine the time when the count rates (pre-event subtracted) reach a given (first) threshold and the time when they reach exactly twice that value. That length of time should then be subtracted from the first threshold time to obtain the onset time. The general case is not as straightforward. A complex injection with duration of minutes, and a broad response in energy surely complicates the picture, but the relevance of those two issues can be assessed by considering onset times inferred from consecutively higher thresholds.

4.4.1 Onset times at neutron monitor stations

Neutron monitor data do not give the omnidirectional flux, rather they give essentially the flux from a particular look angle. Ideally, the omnidirectional flux should be reconstructed using the available stations, but NMS located at sites sampling the small pitch angles should reasonably well reproduce the flux curve near the onset of the event. For 2012 May 17, Mishev et al. (2014) GLE show that the onset of the event is strongly anisotropic and it is clearly seen at Oulu, Apatity, and the South Pole, the stations corresponding to look directions with small pitch angles, and is rather weak at the other stations we studied. Even for the sites showing the strongest signal, data are quite noisy and require integration from 2 to 4 minutes to achieve a smooth rise.

The first step to determine an onset is to determine the optimal integration time. This requires both knowledge of the average slope of the event during the rise phase, and the noise at any given instant. To compute an average slope, we first determined the time to half-rise t_h, which is the time it took the event to rise from 20 to 70% of its peak value. For stations under consideration, t_h is below 10 minutes. For 2012 May 17, the rise from pre-event values is rather modest and the noise in the count rates can be assumed as constant. We note that NMS data needs to be pressure corrected, or there can be very large variations and underlying trends even at timescales of only a few hours. We used data from the day before the event to determine the noise levels and verified that the pre-event is reasonably stable and that a 4σ threshold is adequate to compute onset times.

To chose an integration time, we have used t_h to infer an average slope and then determined the time interval it would take an event for this kind of a slope to reach four times the pre-event noise levels. Apatity and Oulu thus required four-minute integration times; South Pole stations require integration times below 2.5 minutes. We then did a sliding average integration of the NMS data, subtracted the pre-event average values, and determined the time at which we first see a significant rise above the pre-event and the time at which we see the counts at twice that value. To determine biases that could be arising from the integration method used, and to assign error bars to the onsets thus computed, we ran 10000 Monte Carlo simulations of onset determinations assuming a linear rise (same slope as the average computed for that particular NMS), the same pre-event noise function, and the same integration methods. The values obtained from those Monte Carlo simulations were then ordered and the median used as a correction (mostly negligible) for the onset time and percentiles corresponding to a standard variation for a normal distribution (approximately 16 and 84%) used to determine the uncertainty time ranges.

For Oulu data, the first threshold used for the linear approximation was 01:54.0 UT, corresponding to 4.1 times over pre-event background error and 25.2% of peak counts. The event took nearly four minutes to double the counts and as such the inferred onset time for Oulu data, using the linear approximation with correction for underlying biases, is 01:50.2 UT. The uncertainty interval is from 01:48.4 to 01:51.3 UT. The first threshold used for Apatity was at 19.8% of maximum, corresponding to 4.3 times over pre-event background error. The inferred onset time for Apatity, using the linear approximation with correction for underlying biases, is 01:49.6 UT. The uncertainty interval is from 01:47.9 to 01:50.6 UT. For South Pole and South Pole bare, we obtain statistically significant later times, 01:53.7 and 01:58.2 UT with uncertainties about $\pm$ 1 mn from those values. The times we obtained are consistent with the values found in the literature. Li et al. (2013) using Oulu, Apatity, and the two South Pole stations determine an average onset time of 01:51 UT ($\pm$ 2 mn). Our average for the same four stations is 01:53 UT ($\pm$ 2 mn). Gopalswamy et al. (2013) used Oulu neutron monitor to determine that the onset at Earth took place between 01:38 to 01:45 UT. This is lower than our estimates for the same station although it can be accommodated at the 2σ level, particularly since the authors do not disclose how much smoothing was applied to the data. A variation such as the one encountered between different authors is not surprising given the reasonably large integration times required; all values are consistent within what we have found to be the optimal integration time (4 mn).

Apatity and Oulu are asymptotically close to each other and, as expected, the times we have obtained are consistent. South Pole values are clearly distinct and this could be because of a series of factors. There could be a slight difference in the pitch angles being sampled, but it is also possible that the South Pole detectors are recording a meaningful contribution of ions with lower energies than those sampled by Oulu and Apatity. For these four stations the effective cutoff rigidity is not determined by the geomagnetic cutoff but from atmospheric absorption. While Oulu is essentially at sea level (15 m altitude) and Apatity is not much higher (181 m altitude), South Pole stations are at 2820 m elevation above sea level. The response threshold of the neutron monitors to primary particles is about 430 MeV/nucleon for close to sea level stations, while for South Pole stations the reduced atmospheric mass lowers the threshold to $\approx$ 300 MeV/nucleon.

4.4.2 Onset times at EPAM

We determined the onset times for all LEMS120 channels although we only present the values for P'2 and P'8, since they define the extremes in instrumental temporal response. For the onset determinations, we removed the pre-event by detrending. The whole process of integration, biases and error assessment was similar to the one described for NMS data. Values for times to half-rise are about 27 minutes and optimal integration time was found to be 144s. The fluctuations in the pre-event subtracted counts were slightly bigger than would be expected from count statistics alone, thus we determined the maximum and minimum values observed in detrended pre-event count values for the 90 minutes before 01:30 UT, and used the difference between those values as a limit to be exceeded by the threshold to be used. That is, we only considered times after the event crossed both the amplitude of fluctuations and had a signal-to-noise level of at least four. We used the first instance this condition was met

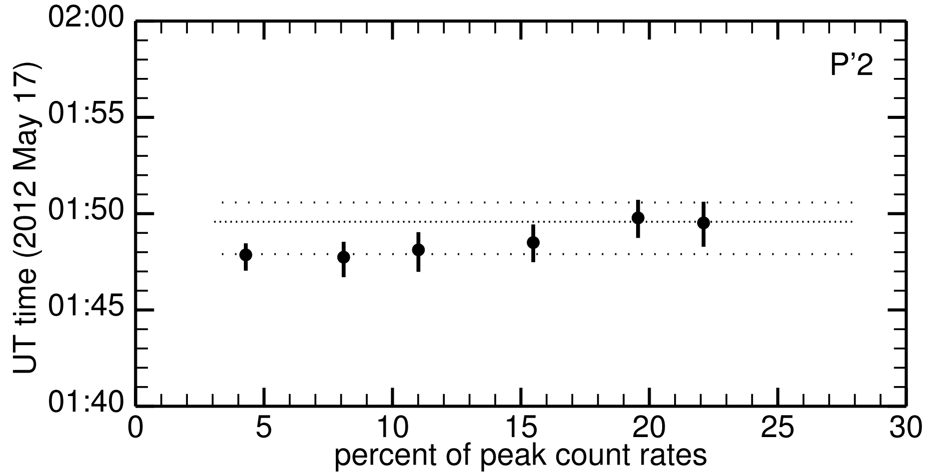

Figure 4.13: Onset times versus percentage of peak for the P'2 channel. The dotted lines correspond to average (very close dots) and uncertainty range (more widely spaced dots) of onset times determined for the Apatity neutron monitor.

and the time when that number of counts was doubled to compute the onset time, similar to our analysis of the NMS data. Since at this time we were only at a few percent of the peak in the counts, we were able to consider subsequent points and use each of those points as threshold for onset determination at different fractions of the peak in the counts.

Figure 4.13 shows how the inferred onset times in the linear approximation vary with the point used as the lower threshold for P'2. The rather short range of times seen for P'2 is quite striking; P'3 is not shown here but is very similar to the P'2 plot. The onset time computed for P'2 using 22 and 44% of peak flux as threshold levels are within the error bars of the value obtained for 4 and 8% of peak flux. This is consistent with a nearly linear rise. Figure 4.13 also compares the EPAM times with the value found for Apatity neutron monitor. The agreement is remarkable. The first determination for P'2 gives 01:47.9 UT as onset time, with an uncertainty time interval from 01:47.1 to 01:48.5 UT.

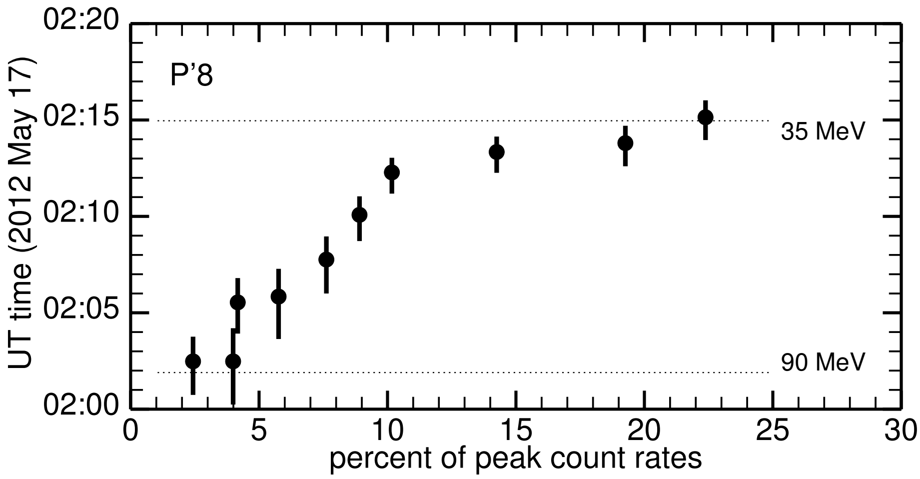

Figure 4.14: Onset times versus percentage of peak for the P'8 channel. The dotted lines correspond to times when energies of 35 and 90 MeV would reach the Earth orbit assuming that the onset times measured for P'2 reflect the arrival of 3 GeV protons.

Mishev et al. (2014) determined the energy spectra from the NMS data as the event progresses, and from their analysis we can infer that, during the GLE, fluxes from solar particles of rigidity higher than about 4 GeV are not seen above Galactic cosmic ray values. For protons, this corresponds to a kinetic energy of about 3.1 GeV. From the spectra presented in Mishev et al. (2014) and from our model results we also verified that we still expect a small but significant number of counts at energies higher than 3.1 GeV, so we assign that energy as being the limit for detectability in P'2. Since counts numbers are higher in P'2 than P'3, we can then bound the response in P'2 as being due to at least 1 GeV protons. From the solar wind for this day we compute a spiral magnetic field length from the sun to the earth of 1.20 AU, and from that we infer that 3.1 GeV protons left the Sun at about 01:37.7 UT, and that the uncertainty in the exact energy range does not lower this value by more than one minute.

As shown in figure 4.14 for P'8 the values for the onset computed from different fractions of the peak count rates span about 15 minutes in time. The dotted lines in figure 4.14 show the arrival times expected for protons of 35 and 90 MeV, assuming they left the Sun at 01:37.7 UT. Although the channel count rates rise in a way that clearly is not linear, the computed onset times determined using different thresholds of the peak in the counts are bound by what we expect to be the likely energy range for the channel. For P'8, we were also able to determine the onset of ions in the nominal energy range identifying the onset from its signature in flux angular signatures (illustrated in figure 4.5).

4.5 Discussion and conclusions

Progress was made in the treatment of the electron data from the LEFS instruments onboard the EPAM and the Ulysses, specially when it comes to the dependence of the Geometric Factor with the energy and also in the subject of more accurate onset timing calculation for the electrons with energies in the nominal ranges of the instrument. Still, due to their relatively low energy, these particles are not of extreme importance when it comes to analyze the release times at the Sun for GLE events. In Morgado and Maia (2014) the onset times obtained by this method are shown to be in accordance with the observed by the WIND, but these findings are not as important to determine the release time back at the Sun as are the ones that were possible to obtain by using proton data.

For proton data we identified a signature in the LEMS120 ion telescopes in EPAM, which can be attributed to penetrating high energy protons entering the detector chamber and being counted in the nominal low energy channels. The inferred energies and onset times agree very well with neutron monitor stations close to sea level like Apatity and Oulu and are consistent with the first arriving particles having energies

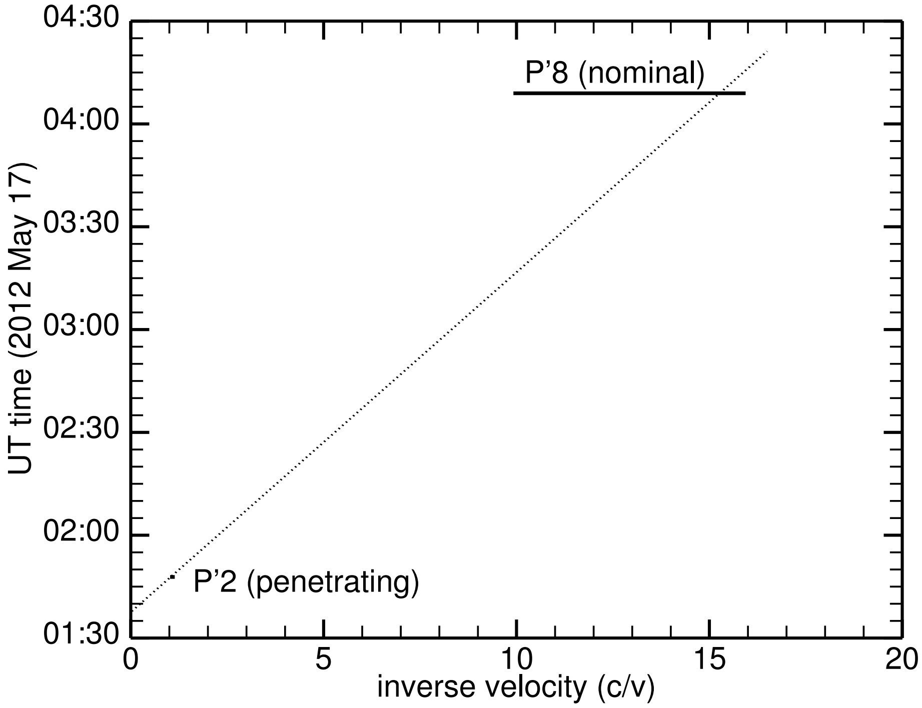

Figure 4.15: Arrival times for P’2 penetrating ions, whose counts are dominated by higher than 1 GeV protons, and for P’8 field of view 1.9 to 4.8 MeV per nucleon ions. The dashed line marks the expected arrival time at 1 AU as a function of inverse velocity for particles released back at the Sun at 01:37.7 UT and following the archimedian spiral corresponding to the observed solar wind conditions.

from 1 to 3 GeV. The high energy signatures detected in the EPAM data are relatively easy to identify: onset at ion channels almost at the same time as the onset for the electron channels, with the onset at P’2 and P’3 earlier than for P’8, marked anisotropy in the pitch angle distribution with shapes differing strongly between P’2 and P’8. This development offers another valuable source of information for many other ion events that occurred after the launch of EPAM. We verified that other GLEs, including the particularly strong event on 2005 January 20, show the same type of signatures. Being able to study near relativistic proton events offers also a reason to reexamine HISCALE data to look for GLE like events that might have missed the Earth.

The 2012 May 17 GLE is particularly interesting for two main reasons: (i) it is only the first of solar cycle 24, while in the same period of solar cycle 23 five had already been seen; and (ii) it is related to a rather mild flare, only M class. There are already a few articles published on the timing of the electrons and ions seen in association with the 2012 May 17 GLE and how those relate to the flare and CME activity (Gopalswamy et al., 2013; Li et al., 2013). We were able to significantly constrain the inferred release time for the ions back at the Sun because P'2 is dominated by a relatively narrow range in propagation times (protons with velocities between 0.9 and 0.97c). Figure 4.15 compares the onset times determined for P'2 (penetrating protons) and P'8 (1.9 to 4.8 MeV nominal energy ions). The determined onset times are consistent when one considers the full range of energy for the channels, so that the first arriving 2–5 MeV and higher than 1 GeV ions could have been accelerated in related processes. The P'2 onset timing implies a release back at the Sun of about 01:37.7 UT for the ions; the corresponding electromagnetic emissions that could help identify the source region of those particles would arrive at the Earth at 01:46 UT.

The GLE was associated with an M5.1 flare starting, peaking, and ending at 01:25, 01:47, and 02:14 UT, respectively. Gopalswamy et al. (2013) report also a metric type II burst at 01:32 UT by directly examining the dynamic spectra from Hiraiso, Culgoora, and Learmonth observatories. These times should be compared with 01:46 UT, when we would expect to see electromagnetic signatures from the Sun at 1 AU associated temporally with the ion release. Both the flare start and the type II onset occur well before the time inferred for the ion release. Gopalswamy et al. (2013) present a thorough analysis of the timing of the fast CME associated with the GLE event, using coronagraphic data and from that analysis we can infer that the ions were released after the CME initiation when the CME leading edge was about

3 solar radii from Sun center. Gopalswamy et al. (2013) attribute the ion event to acceleration by a CME driven shock, developing low in the corona. However, the fact that the time we infer for the ion release nearly coincides with the peak in soft X-ray emission, which can be used, although with some caution, as a proxy for the end of hard X-ray emission, is intriguing. We can not thus completely exclude that the origin of GeV ions could be related to a magnetic restructuring process back at Sun such that the (weak) emission from precipitating particles confined inside closed structures suddenly ceased when particles gained access to open field lines, thus being able to reach 1 AU.

Bibliography

Gopalswamy, N., Xie, H., Akiyama, S., Yashiro, S., Usoskin, I., and Davila, J. (2013). The first ground level enhancement event of solar cycle 24: Direct observation of shock formation and particle release heights. *The Astrophysical Journal Letters*, 765(2):L30.

Haggerty, D., Roelof, E., Ho, G., and Gold, R. (2006). Qualitative comparison of ace/epam data from different detector heads: Implications for noaa rtsw users. *Advances in Space Research*, 38(5):995–1000.

Kocharov, L., Vainio, R., Kovaltsov, G., and Torsti, J. (1998). Adiabatic deceleration of solar energetic particles as deduced from monte carlo simulations of interplanetary transport. *Solar Physics*, 182(1):195–215.

Li, C., Firoz, K. A., Sun, L., and Miroshnichenko, L. (2013). Electron and proton acceleration during the first ground level enhancement event of solar cycle 24. *The Astrophysical Journal*, 770(1):34.

Maia, D. and Morgado, B. (2014). Timing of the 2012 may 17 gle using goes13 epead data. *Astronomy and Astrophysics, in press.*

Maia, D. J. F., Gama, R., Mercier, C., Pick, M., Kerdraon, A., and Karlickỳ, M. (2007). The radio-coronal mass ejection event on 2001 april 15. *The Astrophysical Journal*, 660(1):874.

Mishev, A., Kocharov, L., and Usoskin, I. (2014). Analysis of the ground level enhancement on 17 may 2012 using data from the global neutron monitor network. *Journal of Geophysical Research: Space Physics*, 119(2):670–679.

Morgado, B., Filipe Maia, D. J., Lanzerotti, L., Gonçalves, P., and Patterson, J. D. (2015). The low energy magnetic spectrometer on Ulysses and ACE response to near relativistic protons. *A&A*, 577:A61.

Morgado, B. and Maia, D. (2014). Electron scattering profile of the epam experiment on ace. analysis of the electron event associated with the 2012 may 17 gle. *Astronomy and Astrophysics, in press.*

Peltola, T. (2014). Charge collection efficiency simulations of irradiated silicon strip detectors. *Journal of Instrumentation*, 9(12):C12010.

Roelof, E. (1969). Propagation of solar cosmic rays in the interplanetary magnetic field. In *Lectures in High-Energy Astrophysics*, volume 1, page 111.

Shen, C., Li, G., Kong, X., Hu, J., Sun, X., Ding, L., Chen, Y., Wang, Y., and Xia, L. (2013). Compound twin coronal mass ejections in the 2012 may 17 gle event. *The Astrophysical Journal*, 763(2):114.

Wüest, M., Evans, D. S., and von Steiger, R. (2007). *Calibration of particle instruments in space physics.* ISSI, The International Space Science Institute.

Chapter 5

Solar release time for the 2012 May 17 SEP event

Contents

The methods developed for the analysis of the data from the low energy magnetic spectrometer on Ulysses and ACE response to near relativistic protons in Chapter 4 can also be passed on to other instruments. The issue is once again that near relativistic protons may cross the material shielding the particle detectors aboard spacecraft, lose some of their energy in that material, and be counted as particles of substantially lower energy. This is a phenomena of particular relevance close to the onset of the event, the period that is crucial to infer the release time back at the Sun of the particles reaching Earth orbit. Although newer instruments often take into account this effect and successfully remove most of these particle effects when treating the data, the purpose shown in Chapter 4 was not only to successfully identify the arrival of these particles, but also to take a step further and to use this untapped data to our advantage to further constraining the release times of particles back at the Sun. As such, we want to address with particular emphasis the instrument performance outside of nominal behavior due to particles entering from outside of the field of view of the detectors, and the ways in which this contamination affects timing analyses.

Also, by using further instruments and applying the technique described in Chapter 4 we are able to show that the method is consistent across other instruments, providing in one hand further validation for the method and on another level a better constrain of the release timing of the proton event side of the picture back at the Sun. The present analysis will be show to be consistent not only with the timing results by Morgado et al. (2015) and presented in Chapter 4 but also with the timings of Mishev et al. (2014) using the Neutron Monitor Network and the timings presented by other authors Kühl et al. (2015); Li et al. (2013) taking into account the presented considerations that will follow below.

5.1 The EPEAD instrument

The Energetic Proton, Electron, and Alpha Detector (EPEAD), part of the overall SEM (Space Environment Monitor) mounted to GOES14 satellite is a dual instrument: there are two EPEADs in the same spacecraft, one with a field-of-view (FOV) to the east, and the other with an FOV to the west. Each EPEAD consists of a proton telescope and three domes. We concentrate our attention on the P1 to P3 energy channels from the telescope and the P4 to P7 energy channels from the domes. We also address the proton response of the E3 dome electron channel. There is a very detailed EPEAD documentation Hanser (2011) available from the Space Environment

Monitor web-pages freely available for download. For published references on the EPEAD equivalent, then called EPS, on GOES 8–12 see Onsager et al. (1996); Sellers and Hanser (1996). The GOES 8–12 EPS and GOES 13–15 EPEADs share the same design.

When dealing with EPEAD proton data from periods when considerable proton fluxes at energies in excess of 50 MeV are present one needs to consider two contributions for the count rates recorded in different EPEAD channels. The value of 50 MeV is not because that is an energy of particular importance for the transport of solar protons, but it is defined by the instrument characteristics, in particular the amount of shielding material around the detectors. One contribution for the counts is what we refer to as the FOV, or nominal energy range contribution, corresponding to particles entering through the apertures defined by the collimators. There also is what in EPEAD documentation is referred to as the spurious contribution, resulting from out-of-aperture responses to high energy protons. The GOES/EPEAD data products include both the raw data, which we hereafter refer to as uncorrected, and processed (corrected) data; the later is obtained from the former using a set of algorithms to subtract spurious response from nominal response.

5.1.1 Proton channels

To illustrate how obvious the presence of the spurious component can be for events whose spectra extends to the highest energy channels, we show in figure 5.1 the uncorrected count rates from P1 and P6 for the 2012 May 17 GLE. The P1 curve rises only a few minutes later than the curve for P6 despite the fact that nominal energy ranges for the two channels are quite different (0.74 to 4.5 MeV for P1, 84 to 300 MeV for P6). This is indicative of the fact that the first particles seen at

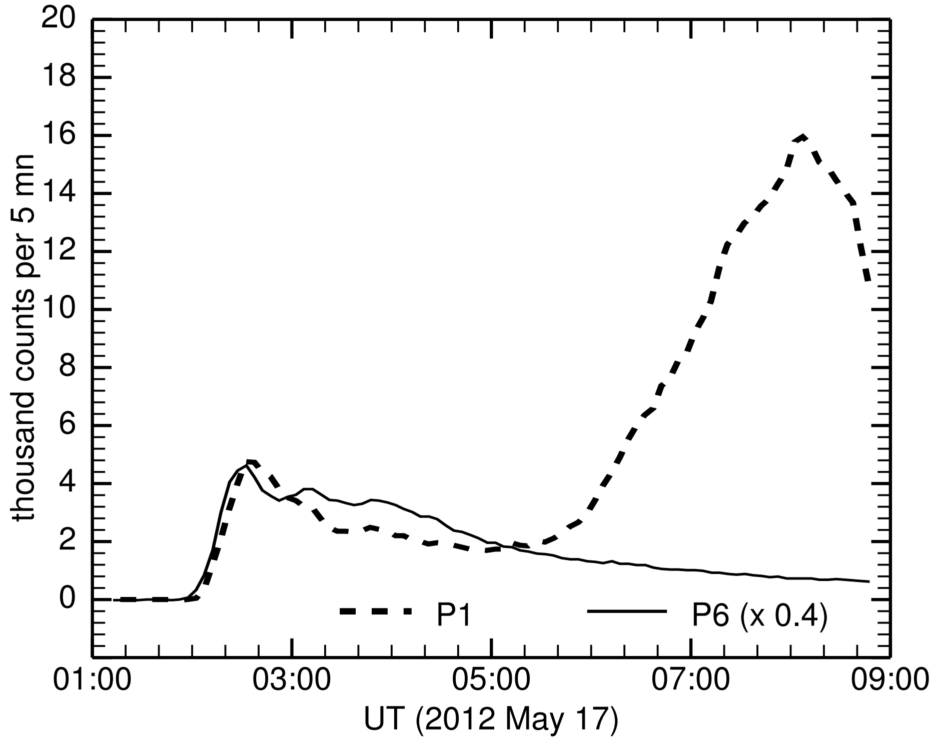

Figure 5.1: Uncorrected counts from the P1 (dashed line) and P6 (solid line) channels on EPEAD scaled so that they show comparable peak values following the onset.

P1 are penetrators with energies on the order of 50–100 MeV, and not part of the population characterized by nominal energy range for P1, that we can see arriving a few hours later. When considering the spurious response it is useful to divide the proton channels in three categories that we address briefly.

The first category includes the channels with nominal responses that are well below 50 MeV: P1 (0.74 to 4.2 MeV), P2 (4.2 to 8.7 MeV) and P3 (8.5 to 14.5 MeV). Those channels show spurious responses to 50–100 MeV protons for P1, 50–125 MeV for P2 and 60–125 MeV for P3. There is considerable difference in propagation time, from the Sun to 1 AU, for a 50 MeV proton (31 mn) and a 14.5 MeV proton (57 mn) so that when a spurious response is present it can be distinguished from nominal response from a simple visual inspection of the count rate curves, in particular by comparing

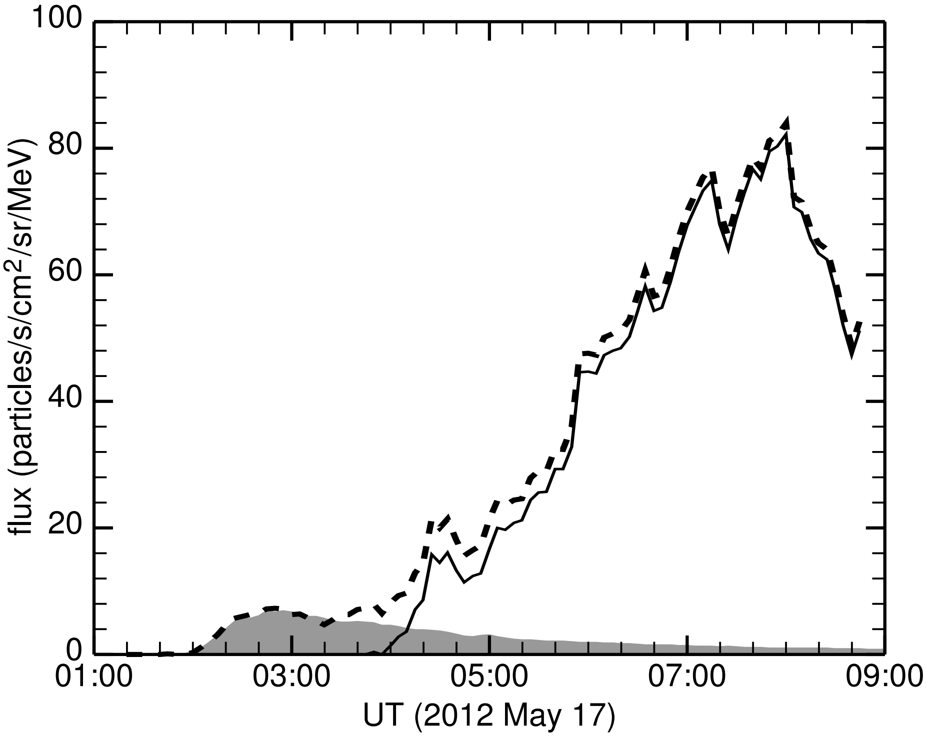

Figure 5.2: Comparison between different data products from EPEAD illustrating the contribution of spurious protons. The dashed line corresponds to uncorrected flux from the P2 channel on EPEAD while the solid line corresponds to the corrected flux for the same channel. The gray area corresponds to the estimated flux for protons with energies higher than 50 MeV, scaled to be comparable to the uncorrected flux.

different GOES data products. We show in figure 5.2 the response of P2 for the 2012 May 17 event, including the raw data and two corrected products. The first two hours of the event in P2 are dominated by the arrival of the spurious component, and the shape of the uncorrected curve at the onset matches rather well the flux of protons with energy above 50 MeV. The rise of the spurious component is for this channel well separated from the rise of the nominal component. This also is the case for the P1 and P3 channels (data not shown here).

For P4 (15–40 MeV nominal response) and P5 (38–82 MeV nominal response) the spurious contribution extends the response from P4 to 150 MeV and from P5 to 190

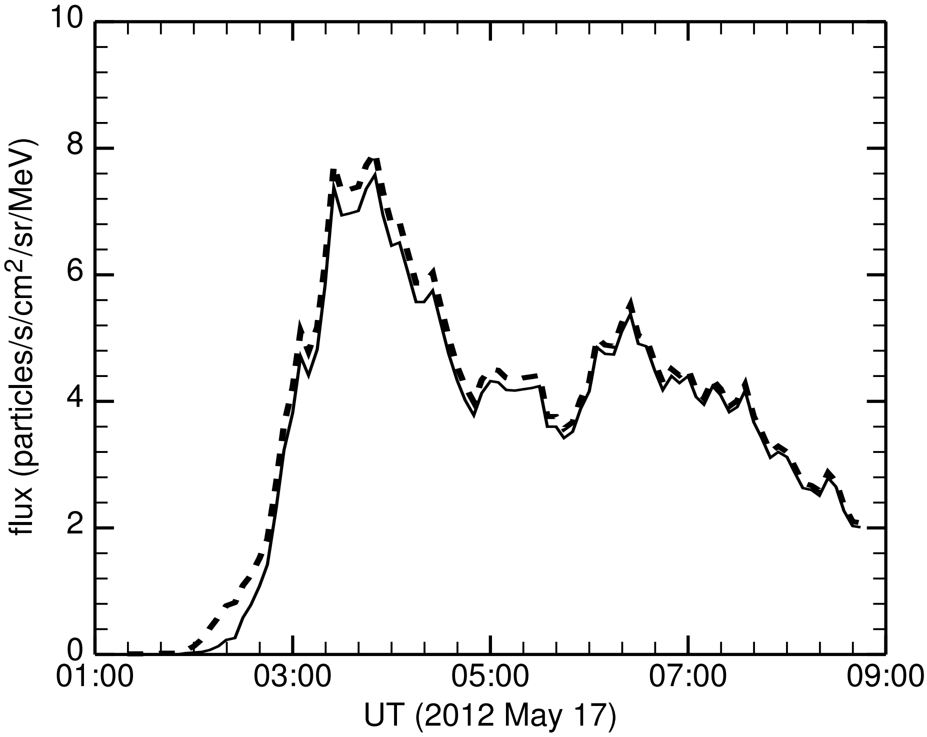

Figure 5.3: Comparison between different data products from EPEAD illustrating the contribution of spurious protons. The dashed line corresponds to uncorrected flux from the P4 channel on EPEAD while the solid line corresponds to the corrected flux for the same channel.

MeV. Counts corresponding to the arrival of spurious protons for P4 and P5 will be so close temporally to nominal response that a separate rise is not identified in the uncorrected data. This is illustrated in figure 5.3, where the response of P4 for the 2012 May 17 event is shown. At the onset the response is clearly dominated by the spurious component, even though it merges smoothly with the rise of the nominal component.

Finally, the higher energy channels, P6 (84 to 300 MeV) and P7 (110 to 900 MeV) have a nominal energy range which substantially overlaps the spurious response. The spurious response is included by default in P6 and P7 geometrical factors.

5.1.2 Electron channels

EPEAD domes include three channels, E1 to E3, designed to measure electron fluxes. The E1 channel count rate from the ambient electron population normally largely exceeds the response to protons so the E1 channel is of little use for solar proton analysis. The E2 channel may also have a significant count rate from the ambient electron population. The E3 electron channel measures the greater than 4 MeV electron flux at geosynchronous orbit and also responds to protons above 40 MeV. The response to cosmic ray background protons greater than 40 MeV generally already dominates over the electrons counts in channel E3, and the solar proton contribution should become strongly dominant during GLE related SEP events. Hence the E3 channel can provide complementary information on proton fluxes, with the estimated response to protons extending up to 800 MeV in kinetic energy. The spurious response from the E3 channel significantly overlaps the P7 proton channel.

5.2 Threshold times and onset times

Our major concern is determining the release time t_S, close to the Sun, of the particles that GOES/EPEAD measures in situ for a given energy channel. This time is then related to the onset time at the spacecraft t_{on} by the relation

$$t_{on} = t_S + \Delta t_p \tag{5.1}$$

where Δt_p is the propagation time for the particles.

Being charged particles, protons in SEPs mostly follow the interplanetary magnetic field. In the absence of major irregularities in the solar wind the path traveled by the protons thus should by given by the spiral length L_B of the interplanetary magnetic field, a length that can be computed from the solar wind speed. The solar wind speed also affects propagation due to effects such as convection and adiabatic deceleration (Ruffolo, 1994), that can change the speed of the particle, however those are mostly irrelevant for proton energies above a few MeV. As such we consider the particle speed as constant. This means that the major contribution affecting the particle propagation is the evolution of its pitch angle, the angle between the velocity and the mean field. The pitch angle is not a conserved quantity along the particle motion, it is changed by different processes acting on the particles from their release until the time of detection, processes that can be modeled in the framework of focused transport with pitch angle scattering (Roelof, 1969). The transit time Δt_p for a proton of speed v is then be given by:

$$\Delta t_p = \frac{L_B}{c\,\overline{\mu}}\,\frac{c}{v} \tag{5.2}$$

where c is the speed of light in vacuum and the $\overline{\mu}$ term can be understood as a sort of average cosine of pitch angle.

A straightforward and popular simplification is to assume that the first arriving particles suffer very little pitch angle scatter, so that $\overline{\mu} \sim 1$ implying that for particle fluxes measured at different energies we would expect that the onset times as a function of c/v should follow a straight line. For the typical spiral length of 1.2 AU the slope L_B/c of that straight line should be about 10 minutes. Results from this method, named the inverse velocity method or time shifting analysis, often contradict the expectations, in particular the path lengths obtained from the linear fits are frequently substantially larger than the actual path length along the local interplanetary magnetic field line (Tan et al., 2013; Mewaldt et al., 2003). To interpret this discrepancy one needs to consider several issues intrinsic to the analysis of particle fluxes.

What we can directly compute is the time when the count rates surpass a certain threshold value, given as a function of signal to noise ratio or as a fraction of the peak count rates. The onset time, what we really want, corresponds to the time at which the first arriving particles would be detected in the absence of noise. If the first arriving particles do so in large numbers compared to the pre-event background then the onset time and the threshold time will be close. However for events with poor signal to noise ratios we will not be seeing the arrival of the first particles and the threshold time thus corresponds to the arrival of particles for which propagation effects need to be accounted for, so that some correction needs to be made. If such a correction is not possible then one should regard the threshold time as an upper limit to the onset time. This is true even for what could be regarded as a strong event: as discussed in Sáiz et al. (2005), the actual path length can already be severely overestimated using threshold times computed at about 2% of peak.

The nature of the threshold to onset correction depends on a series of factors. The particles are released with a finite duration of injection at the Sun, however the injection profile gets smeared by propagation effects in such a way that even a delta-like injection at the sun may originate a SEP event lasting for tens of minutes or even hours at the Earth. We verified, using the models delineated in Maia et al. (2007) that, for an instantaneous release of mono-kinetic particles at the Sun, the flux profile at 1 AU is essentially linear from 1 to about 40% of peak. This means that for an instrument with a narrow response in energy, and if the count rates closely reflect the omnidirectional particle flux, propagation effects could be compensated by a simple linear extrapolation of the count rate curve.

Assumption of linearity provides a simple way to compute onset times from threshold times, however many factors other than propagation affect the shape of the flux curve measured by a particle detector. For GOES/EPEAD data those intrinsic to the detector (width of the energy response, response factors as a function of energy, angular directions being sampled) are particularly important. There is enough transit time difference between the highest and lowest energy for each of the given EPEAD channels that, as the event progresses, the counts in the channel are dominated by the arrival of progressively lower energies, so that the early part of the rise of the channel is not exactly linear. This effect (and also effects associated with a prolonged injection back at the Sun) can be tested by comparing the onset times computed from distinct thresholds.

5.3 Integration times

Intimately linked to threshold time determinations is the integration interval chosen. A meaningful way to chose an integration interval is to compute an average slope for the rise of the count rates observed in the channel and estimate the time needed to produce counts (pre-event subtracted) with a signal to noise ratio of at least four. We did so, for the 2012 May 17 event, using the instants when the count rates of the high-time resolution data reach 25% and 75% of peak to define the average slope. The optimal values for integration were then chosen as multiples of the high-time resolution data cadence. For E3 and P1 data were integrated 49 seconds, 65 seconds for P4, P6 and P7, 131 seconds for P2 and P3, and 98 seconds for the P5 channel. After this integration we verified that the early part of the rise curves for the P6, P7 and E3 channels, below 1 to 2% of the peak, shows evidence for a tail with a slower rise. The corresponding integration times were 192 seconds for those three dome channels.

While increasing the integration time enables better signal to noise ratio it also shifts the response of each time bin to lower energies. Let us consider as an example the

P7 energy channel (110 to 900 MeV) for which we determined an optimal integration value of 192 seconds for thresholds below 2% of the peak count rates. Since we will be making a linear correction to this threshold time, we need at least two integration intervals of 192 seconds, that is, we consider a time window of 384 seconds. A 190 MeV proton traveling 1.2 AU takes roughly 380 more seconds than a 900 MeV proton does, thus we need to consider that the time bins include protons from 900 to 190 MeV (or lower).

The 2012 May 17 GLE is a considerably hard event. From the ratio of peak counts at different channels, assuming that the peak flux as function of energy follows a power-law, we compute a spectral index in energy harder than 2.5 for the P1 to P6 channel energy range, that should be representative of the spectrum at the source. At the energies sampled by P7, neutron monitor data suggests that the spectrum is somewhat softer (Mishev et al., 2014). Assuming that during the 384 second time window used to compute the onset time at P7 this spectral index is a reasonable approximation of the proton spectra then the average energy of the particles sampled in P7 is on the order of 300 MeV or lower. To reach this value one needs to take into consideration that the geometrical factors for the dome channels show a very marked dependency on energy, so that the use of the response curves given in the documentation is a major requirement to address the determination of quantities like average energy and spectra from EPEAD data. For the P1 to P5 energy channels there is typically only a factor of 2 in the response in energy to spurious protons, so the integration bias is not as marked as it is for the P7 energy channel. The average energy for the P1 channel at onset will be lower than 90 MeV, for P4 the average will be lower than 115 MeV, for P5 lower than 125 MeV, for P6 lower than 220 MeV and for E3 lower than 280 MeV. These are approximate values for the average behavior of the particles sampled by each channel and although they can be refined using the time from estimated onset instead of simply the length of two integration bins, the difference is not significant for the 2012 May 17 event.

There also is another bias related to integration, a tendency for underestimating the onset time when doing the linear approximation. We checked for this effect in all energy channels by doing Monte Carlo simulations; corrections were small when compared to the integration times.

5.4 Timing of the 2012 May 17 event

Data (uncorrected) for channels P1 to P7 and E3 were downloaded from the EPEAD archive at the highest available time cadence (16.4 for E3, 8.2 seconds for P1, 32.8 seconds for the other channels) and were integrated for a time length determined according to the optimal procedure described above. The integration was performed as a sliding average, thus we kept the time steps of the original high resolution data. We verified that using either east or west data did not change the results concerning the spurious component so we averaged east and west data. We subtracted the pre-event background and identified the peak in the counts for each channel.

We chose the initial threshold time so that, at all subsequent times up to the time of the peak, the signal to noise ratio at the considered time bin would be higher than four. From this first threshold we then progressed one integration interval at a time, setting a set of threshold times up to 20% of the peak. For each threshold in the series we then determined the time interval needed for the counts to increase by a factor of two. The onset time associated with each threshold was then simply the threshold time minus the doubling time. The results are shown in figures 5.4, 5.5 and 5.6. For reference all figures include lines marking the expected arrival times of the energy

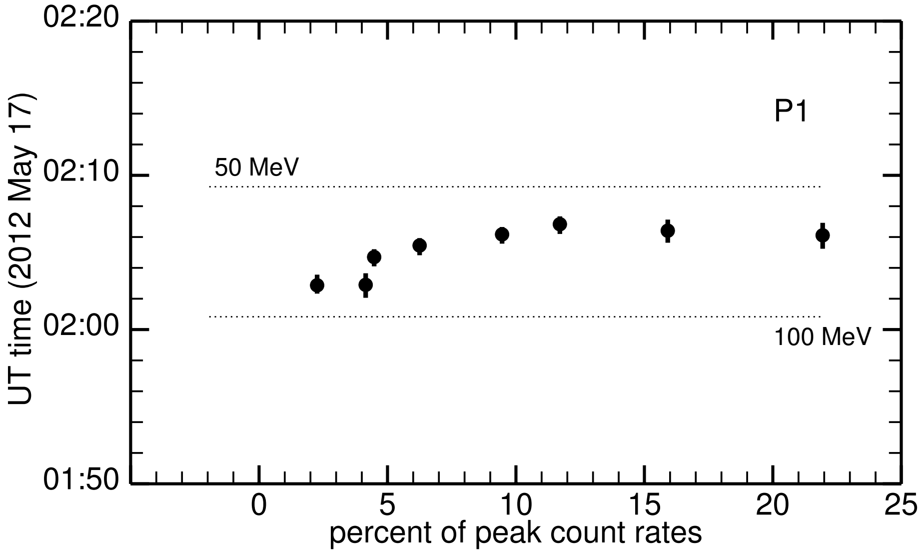

Figure 5.4: Computed onset times for threshold times corresponding to distinct fractions of the peak count rates for the P1 channel on EPEAD using only the period when penetrating protons dominate the count rates. The dashed lines mark the expected arrival times for the energy range of the spurious response.

range under consideration, assuming those particles had left the Sun at 01:37.7 UT as determined for GeV protons by Morgado et al. (2015).

We show in figure 5.4 the onset time as a function of starting threshold for channel P1. For this channel (and also P2 and P3, not shown here) the spurious response can be temporally separated from the FOV response. As such the maximum in peak counts we use as reference is the one for the penetrators, and not the peak corresponding to nominal energies seen later. The onset times estimates made at 2% and 20% thresholds of the peak vary by only 4 minutes, and are consistent with the expected arrival times for the documented spurious response. The temporal response from the P1 to P3 energy channels is thus relatively narrow; they are particularly adequate for timing studies.

As shown in figure 5.5 the range of inferred onset times for P5 data extends considerably as a function of the threshold used. This is expected since the counts from

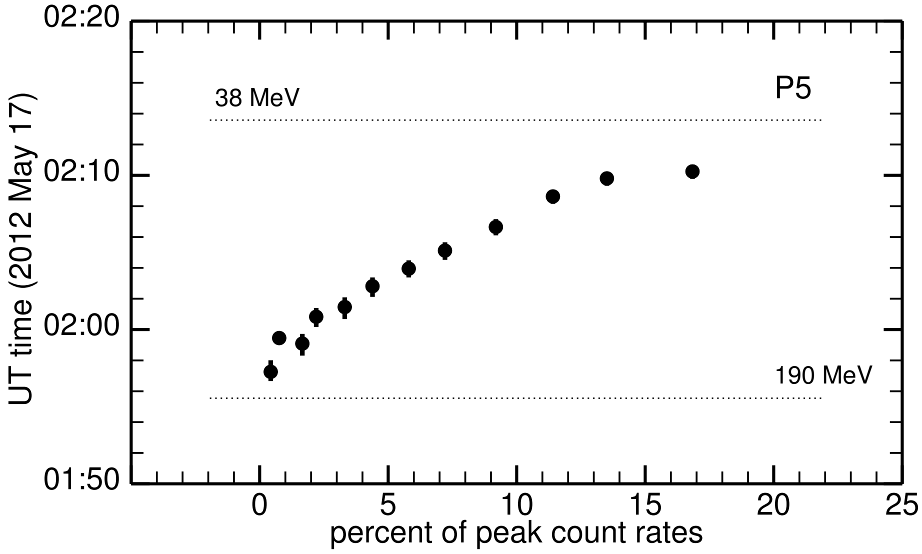

Figure 5.5: Computed onset times for threshold times corresponding to distinct fractions of the peak count rates P5 channel on EPEAD. The dashed lines mark the expected arrival times for the energy range of the channel, including both spurious and FOV response.

spurious particles are not easily distinguished from counts due to the FOV particles. In this event the signal is strong enough, when compared to pre-event background noise, that we seem to be very close to the high-energy expected onset, however for weaker events one should take into consideration that this channel (and also P4, not shown here) has a very broad response.

The range of inferred onset times for the P6 and P7 energy channels is shown in figure 5.6. The onset times computed from threshold times measured from 1 to 20% of peak show variation, but again the variation is bounded by the response in energy of the channels. At the P7 channel the onset time computed from the earliest threshold is considerably later than the expected time for 900 MeV protons, being consistent with the arrival of ≈ 300 MeV protons. As discussed before this is expected given the relatively large integration used and the relatively broad energy width of the channel. As expected figure 5.7 shows that the range of inferred onset times for E3 is very close to what is seen for the P7 energy channel.

The 2012 May 17 event is strong enough that in all EPEAD energy channels we are able to see the flux rising very close to the expected arrival of the particles of the high energy limit of the channel response, with the differences observed explained by bias associated with the integration time. As we progress to higher thresholds of the peak value our onset times are considerably biased towards the lower energy limit. Sandberg et al. (2014) give effective energies of 107 and 104 MeV for P6 and 153 and 148 MeV for P7, which are consistent with the tendency of the results in figure 5.6 for thresholds above 5% of the peak. They also state that the use of the effective energy value for the highest in energy EPS/P7 channel enables the derivation of reliable arrival times for the proton populations that first reach geostationary orbits, also leading to improved particle tracking backwards to their acceleration regions. Our results are consistent with Sandberg et al. (2014) results and recommendations yet go beyond them in considering all channels.

It is important to note the even though there is an obvious bias in figures 5.4, 5.5

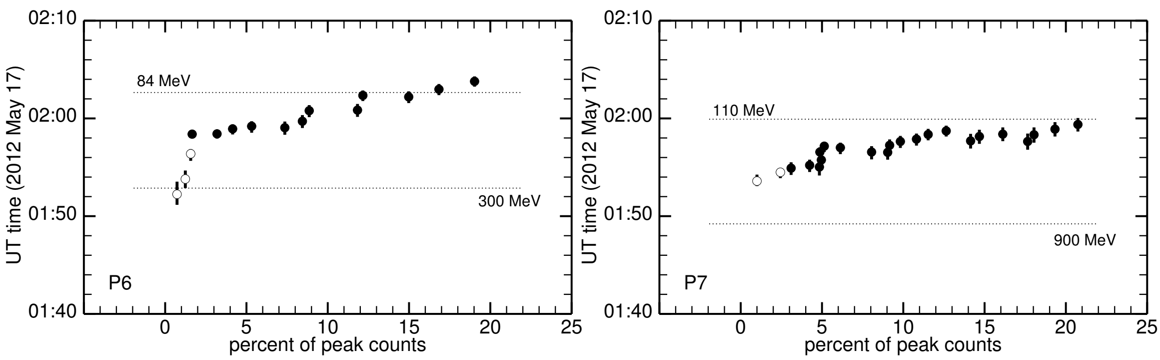

Figure 5.6: Computed onset times for threshold times corresponding to distinct fractions of the peak count rates for P6 and P7 channels on EPEAD. The dashed lines mark the expected arrival times for the energy ranges of the channels. Filled circles correspond to onset times computed from data integrated 65 seconds, while for open circles 192 second integrated data were used.

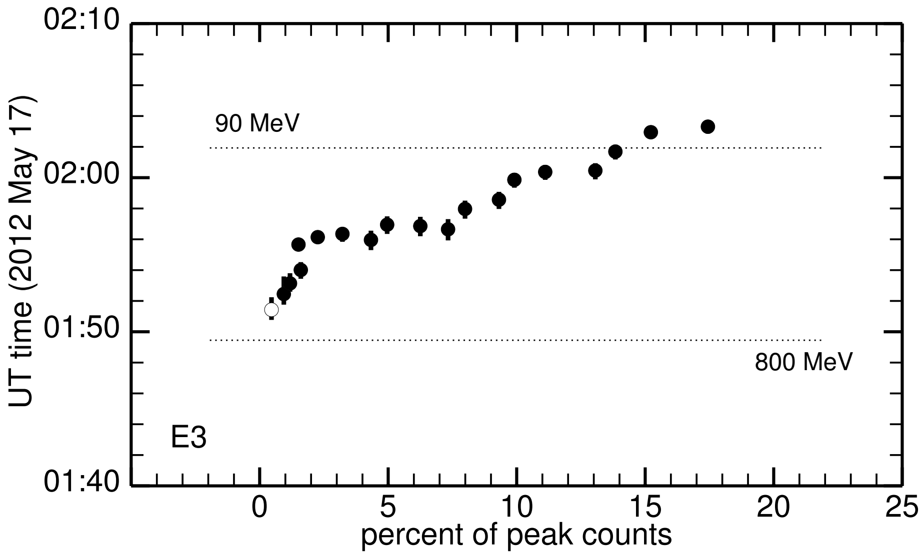

Figure 5.7: Computed onset times for threshold times corresponding to distinct fractions of the peak count rates E3 channel on EPEAD. The dashed lines mark the expected arrival times for the energy range of spurious protons entering the detector. Filled circles correspond to onset times computed from data integrated 49 seconds, while for open circles 192 second integrated data were used.

and 5.6 for the inferred onset times as a function of the threshold used, the values are generally bounded by the reference lines. This means that even for weaker events the onset time estimates are useful as long as they are understood as representing the full energy range and not only the upper, lower or average energy of the channel.

5.5 Solar release times

We show in figure 5.8 the onset time versus inverse velocity for the uncorrected proton data, using the earliest thresholds for each channel. The onset estimate for the P1 channel has much lower error bars than the onset estimates for P2 and P3, and since it mostly overlaps the other two channels we did not include P2 and P3 in figure 5.8. The straight line in figure 5.8 corresponds to the expected onset times for near scatter-free particle propagation along a 1.2 AU archimedian spiral, if those

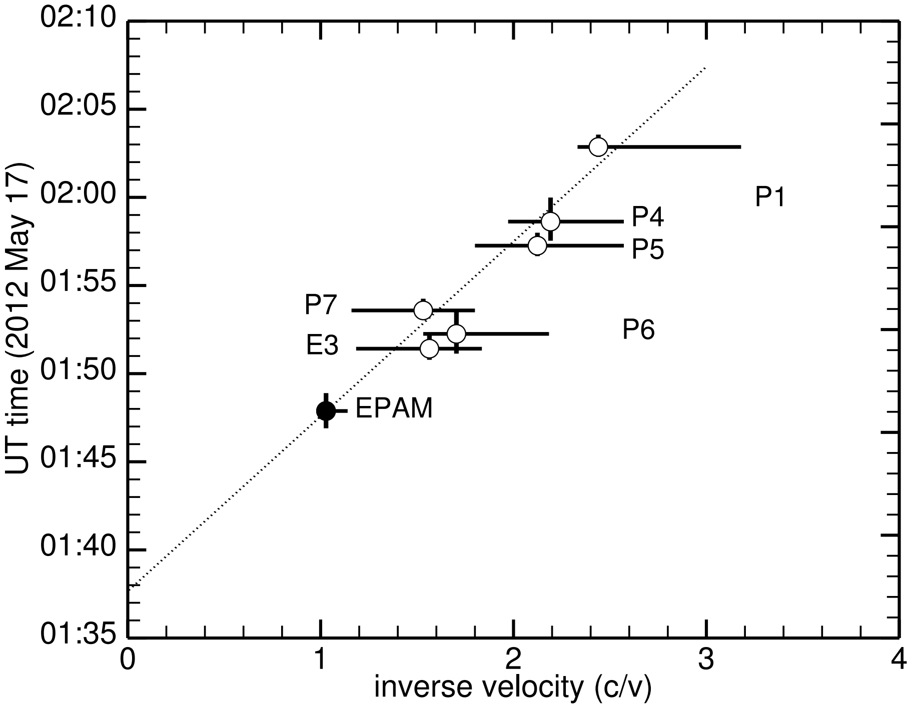

Figure 5.8: Arrival times versus inverse velocity for the EPEAD channels (open circles) and also for EPAM (filled circle). The straight line corresponds to the expected arrival times for particle propagation along a 1.2 AU archimedian spiral and a release time at the Sun at 01:37.7 UT. The open circles correspond to the representative energy for the channel taking into consideration the integration times.

particles had been released back at Sun at the time computed by Morgado et al. (2015) for higher than 1 GeV protons using data from the Electron Proton Alpha Monitor (EPAM) experiment (Gold et al., 1998). The agreement between the timing inferences from EPAM and EPEAD data is remarkable and fully consistent with the archimedian spiral length. The event is intense enough for the computed onsets to be bounded by the highest energy for the channel and the average energy estimated from the integration time. Given that 2012 May 17 GLE is a relatively modest GLE we expect that a similar behavior should be present in nearly all previous GLEs seen with EPEAD instrument.

Our analysis considering the spurious response is limited to the onset of protons higher than 100 MeV, however there is interest in including the corrected data to extend the timing analysis to nominal energy range of P1 to P4 channels. This is not a simple issue: given the very high levels of spurious counts in these channels even a residual contribution remaining after the correction can lead to assigning significance to a false threshold. We imposed the following conditions to determine the first threshold to be used: (i) the corrected counts should be at least two times higher than the spurious component that was subtracted, and (ii) the corrected counts at the threshold should not be larger than 20% of the peak counts (so we can assume a linear correction for propagation effects). Only the P2 and P4 channels met those conditions, with a threshold time computed at 18.5% of the peak for the P2 channel and at 15% of the peak for the P4 channel. We then adopted the same procedure as before: we determined the instant where the counts doubled from the first threshold time and corrected the threshold times accordingly to obtain the onset times. At the instants used to compute the onset (threshold and doubling time) particles from the whole energy range covered by the channel had enough time to propagate to the detector. To compute a representative energy for the channel we used the iterative procedure described in Hanser (2011) to determine the average energy of the channel. Figure 5.9 shows that the timing of these two channels is fully consistent with the timing from the spurious particles, assuming a 1.2 AU path length.

A question we also addressed is: what would happen if we had taken the corrected data ignoring the fact that a significant signal had been removed from it, and we also had not done the linear correction to the threshold times? The answer is given in figure 5.10. Although linear fits from P4 to P7, and also from P2 to P7 are visually consistent with the data, in both cases one retrieves a substantially higher path than the expected spiral length. The two fits give widely differing slopes implying widely

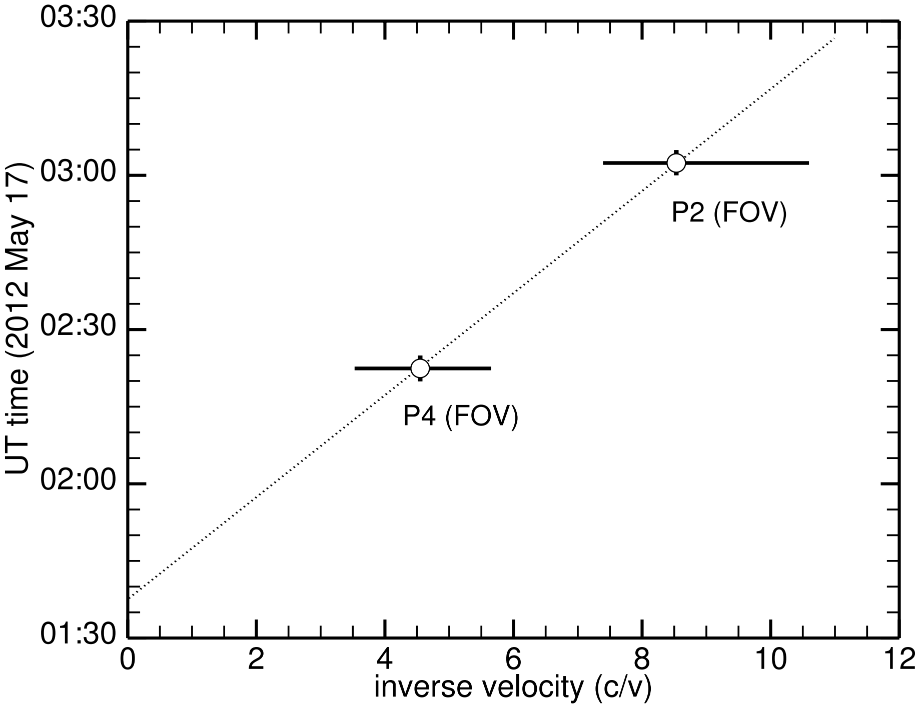

Figure 5.9: Arrival times versus inverse velocity for the EPEAD channels. The straight line corresponds to the expected arrival times for particle propagation along a 1.2 AU archimedian spiral and a release time at the Sun at 01:37.7 UT.

differing path lengths of 1.4 and 2.0 AU, respectively for the P4 to P7 fit, and for the P2 to P7 fit.

5.6 Discussion and conclusions

Raw data from GOES/EPEAD can be used to infer reliable and accurate release times for GLE events if one considers the spurious response associated with the channels. We expect most GLEs to follow the 2012 May 17 event in that we can track the arrival of the particles close to the high-energy limit of the channels with minimal corrections. For weaker SEP events one needs to be aware that the representative energy of the channel will most probably be biased towards the lower energy limit of the channel and as such the full response of the energy needs to be considered. Sandberg et al.

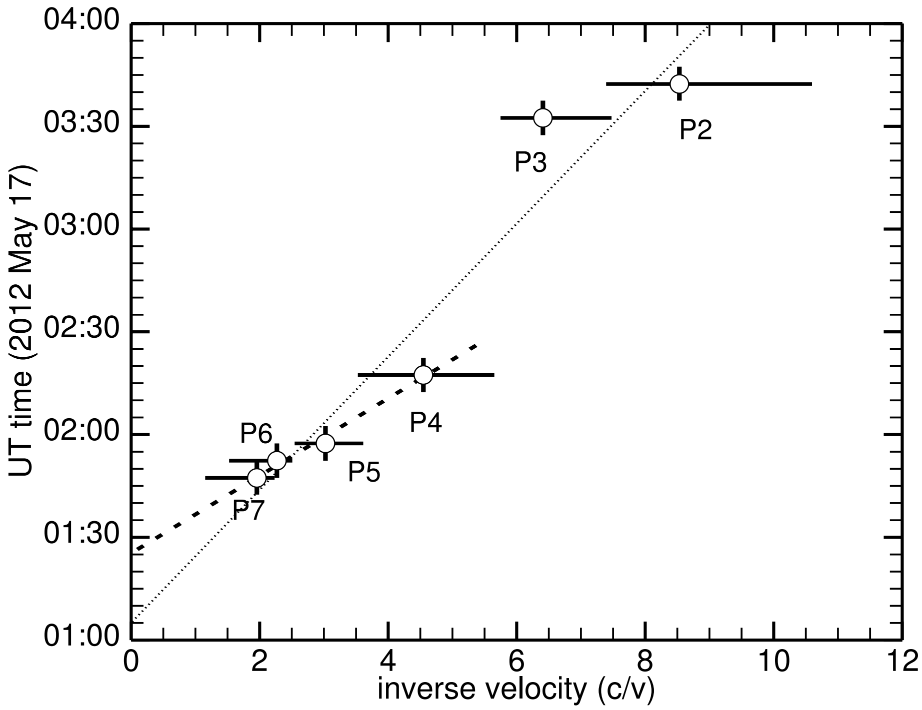

Figure 5.10: Arrival times versus inverse velocity for the EPEAD channels. The straight lines correspond to linear fits using least squares methods.

(2014) calculated the effective energies for all of the GOES EPS channels; their Table 3 though giving results for GOES-8 and GOES-11 also is relevant to GOES-13 by similarity.

For GOES/EPEAD data inverse velocity methods biases arise mainly from three sources: (i) residual contamination in corrected data after spurious count subtraction, (ii) the delay implicit in the threshold time in relation to the onset time, and (iii) uncertainty in the representative energy range for the channel. All of these effects were taken into consideration in our analysis, and they might also play a role in the inconsistencies encountered in timing studies based on other spacecraft data, although traditionally only (ii) is considered (e.g. Sáiz et al. (2005)). Another issue that might produce inconsistencies in inverse velocity methods is a prolonged injection at the source, particularly if the injection curve rises slowly or there is a marked evolution of the energy spectrum at the source.

The 2012 May 17 GLE was associated with an M5.1 flare peaking at 01:47 UT at the Earth, that is, with the photons leaving the Sun around 01:39 UT. The EPEAD data is consistent with a release time back at the Sun for protons above 4 .2 MeV around 01:38 UT, which nearly coincides with the peak in soft X-ray emission, a proxy for the end of hard X-ray emission and thus of the particle acceleration associated with the flare. This is consistent with what is found for most impulsive GLEs by Kurt et al. (2013); Kurt et al. (2013), and strong evidence that the particles observed at 1 AU are of flare origin. We note nonetheless that we can not exclude that the ion population detected in situ might include a later contribution with an origin other than the flare. Recent observations from the Large Area Telescope (Atwood et al., 2009) on the Fermi Gamma-Ray Space Telescope have shown that gamma-ray emission from solar flares is a relatively common occurrence: in the first 4 years of observations LAT has detected emission above 100 MeV in at least 18 flares (Ackermann et al., 2014) including the 2012 May 17 event.

We show in figure 5.11 the plot of gamma-ray emission for the LAT telescope during a period encompassing the 2012 May 17 GLE event. Unfortunately LAT was not pointed at the Sun during the early part of the 2012 May 17 event, so that it missed the period of the impulsive hard X-ray flare, however it detected gamma-ray emission during an observation window starting around 02:09 UT and lasting for about 40 minutes. There also is an increase above background emission seen in the following observation window, lasting until about 04:22 UT, however its statistical significance is not enough to warrant a true positive detection status. As discussed in Ackermann et al. (2014) the most likely explanation for these emissions are decay

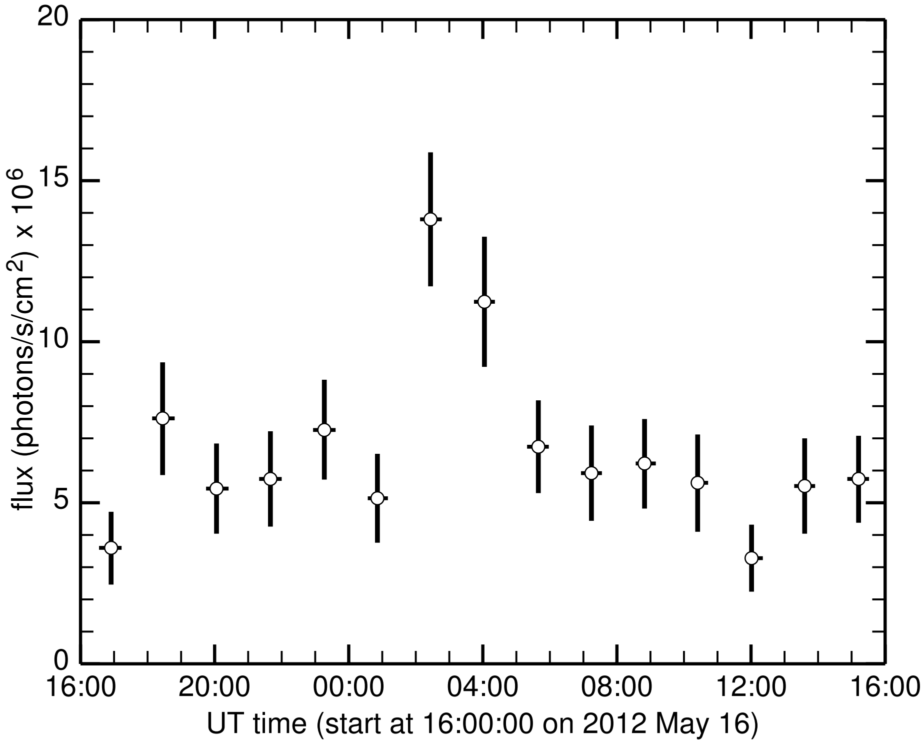

Figure 5.11: Gamma ray emissions from the Large Area Telescope on the Fermi Gamma-Ray Space Telescope.

processes associated with pions resulting from the interaction of hadronic primaries with the ambient ions in the solar atmosphere. There is thus evidence for this event that ions of energies comparable to those seen in situ were present low in the corona for a considerable time period, however a timing analysis like the one we presented can not elucidate if they contributed or not to the in situ event. An inversion of particle data like those presented by Maia et al. (2007); Bieber et al. (2004) would be necessary to retrieve the full injection profile back at the Sun.

Bibliography

Ackermann, M., Ajello, M., Albert, A., Allafort, A., Baldini, L., Barbiellini, G., Bastieri, D., Bechtol, K., Bellazzini, R., Bissaldi, E., et al. (2014). High-energy gamma-ray emission from solar flares: Summary of fermi large area telescope detections and analysis of two m-class flares. *The Astrophysical Journal*, 787(1):15.

Atwood, W., Abdo, A. A., Ackermann, M., Althouse, W., Anderson, B., Axelsson, M., Baldini, L., Ballet, J., Band, D., Barbiellini, G., et al. (2009). The large area telescope on the fermi gamma-ray space telescope mission. *The Astrophysical Journal*, 697(2):1071.

Bieber, J. W., Evenson, P., Pyle, R., Ruffolo, D., Rujiwarodom, M., Tooprakai, P., Khumlumlert, T., et al. (2004). Spaceship earth observations of the easter 2001 solar particle event. *The Astrophysical Journal Letters*, 601(1):L103.

Gold, R., Krimigis, S., Hawkins III, S., Haggerty, D., Lohr, D., Fiore, E., Armstrong, T., Holland, G., and Lanzerotti, L. (1998). Electron, proton, and alpha monitor on the advanced composition explorer spacecraft. *Space Science Reviews*, 86(1-4):541–562.

Hanser, F. (2011). Eps/hepad calibration and data handbook. Technical report, Tech. Rep. GOESN-ENG-048D.

Kühl, P., Banjac, S., Dresing, N., Goméz-Herrero, R., Heber, B., Klassen, A., and Terasa, C. (2015). Proton intensity spectra during the solar energetic particle events of May 17, 2012 and January 6, 2014. *A&A*, 576:A120.

Kurt, V., Kudela, K., Yushkov, B., and Galkin, V. (2013). On the onset time of several spe/gle events: Indications from high-energy gamma-ray and neutron measurements by coronas-f. *Advances in Astronomy*, 2013.

Kurt, V., Yushkov, B., Belov, A., Chertok, I., and Grechnev, V. (2013). Determination of Acceleration Time of Protons Responsible for the GLE Onset. *Journal of Physics Conference Series*, 409(1):012151.

Li, C., Firoz, K. A., Sun, L., and Miroshnichenko, L. (2013). Electron and proton acceleration during the first ground level enhancement event of solar cycle 24. *The Astrophysical Journal*, 770(1):34.

Maia, D. J. F., Gama, R., Mercier, C., Pick, M., Kerdraon, A., and Karlický, M. (2007). The radio-coronal mass ejection event on 2001 april 15. *The Astrophysical Journal*, 660(1):874.

Mewaldt, R., Cohen, C., Haggerty, D., Gold, R., Krimigis, S., Leske, R., Ogliore, R., Roelof, E., Stone, E., von Rosenvinge, T., et al. (2003). Heavy ion and electron release times in solar particle events. In *International Cosmic Ray Conference*, volume 6, page 3313.

Mishev, A., Kocharov, L., and Usoskin, I. (2014). Analysis of the ground level enhancement on 17 may 2012 using data from the global neutron monitor network. *Journal of Geophysical Research: Space Physics*, 119(2):670–679.

Morgado, B., Filipe Maia, D. J., Lanzerotti, L., Gonçalves, P., and Patterson, J. D. (2015). The low energy magnetic spectrometer on Ulysses and ACE response to near relativistic protons. *A&A*, 577:A61.

Onsager, T., Grubb, R., Kunches, J., Matheson, L., Speich, D., Zwickl, R. W., and Sauer, H. (1996). Operational uses of the goes energetic particle detectors. In *SPIE's 1996 International Symposium on Optical Science, Engineering, and Instrumentation*, pages 281–290. International Society for Optics and Photonics.

Roelof, E. (1969). Propagation of solar cosmic rays in the interplanetary magnetic field. In *Lectures in High-Energy Astrophysics*, volume 1, page 111.

Ruffolo, D. (1994). Effect of adiabatic deceleration on the focused transport of solar cosmic rays. *arXiv preprint astro-ph/9408056*.

Sáiz, A., Evenson, P., Ruffolo, D., and Bieber, J. W. (2005). On the estimation of solar energetic particle injection timing from onset times near earth. *The Astrophysical Journal*, 626(2):1131.

Sandberg, I., Jiggens, P., Heynderickx, D., and Daglis, I. (2014). Cross calibration of noaa goes solar proton detectors using corrected nasa imp-8/gme data. *Geophysical Research Letters*, 41(13):4435–4441.

Sellers, F. B. and Hanser, F. A. (1996). Design and calibration of the goes-8 particle sensors: the eps and hepad. In *SPIE's 1996 International Symposium on Optical Science, Engineering, and Instrumentation*, pages 353–364. International Society for Optics and Photonics.

Tan, L. C., Malandraki, O. E., Reames, D. V., Ng, C. K., Wang, L., Patsou, I., and Papaioannou, A. (2013). Comparison between path lengths traveled by solar electrons and ions in ground-level enhancement events. *The Astrophysical Journal*, 768(1):68.

Chapter 6

Analysis of GLE events based on the EPAM's near relativistic proton response findings

Contents

Probably the most interesting outcome of this thesis, was the way we were able to extract previously discarded data from GLE events using EPAM's near relativistic proton response and its success in determining the onset of GLE events in space as presented in Chapter 4 where that response is used to extend the energy range of the instrument for protons and calculate a more accurate arrival time for electrons and mainly protons. The success we had in analyzing the 2012, May 17 GLE event using this method and the fact that we could use that extra data for specific purposes regarding a GLE event convinced us that the potential of these findings can be extended much further and that this research can be extended to any of the GLE events seen by EPAM. In fact, we verified that other GLEs — including the particularly strong event on 2005 January 20 — show the same type of signatures. The prospect of being able to study near relativistic proton events also offers a reason to reexamine

GLE	Baseline Start	Baseline End	Onset	EPAM	Notes
55	1997–11–06 11:00:00	1997–11–06 12:00:00	1997–11–06 12:10:00	Y	
56	1998–05–02 12:00:00	1998–05–02 13:00:00	1998–05–02 13:55:00	Y	
57	1998–05–06 07:00:00	1998–05–06 08:00:00	1998–05–06 08:25:00	Y	
58	1998–08–24 20:00:00	1998–08–24 21:00:00	1998–08–24 22:50:00	Y	
59	2000–07–14 09:00:00	2000–07–14 10:00:00	2000–07–14 10:30:00	Y	
60	2001–04–15 12:00:00	2001–04–15 13:00:00	2001–04–15 14:00:00	Y	
61	2001–04–18 01:00:00	2001–04–18 02:00:00	2001–04–18 02:35:00	Y	O
62	2001–11–04 15:00:00	2001–11–04 16:00:00	2001–11–04 17:00:00	Y	
63	2001–12–26 04:00:00	2001–12–26 05:00:00	2001–12–26 05:30:00	Y	
64	2002–08–24 00:00:00	2002–08–24 01:00:00	2002–08–24 01:18:00	Y	
65	2003–10–28 10:00:00	2003–10–28 11:00:00	2003–10–28 11:22:00	Y	
66	2003–10–29 19:00:00	2003–10–29 20:00:00	2003–10–29 21:30:00	Y	O
67	2003–11–02 16:00:00	2003–11–02 17:00:00	2003–11–02 17:30:00	Y	
68	2005–01–17 06:00:00	2005–01–17 07:00:00	—	Y	$N_{P8'}$
69	2005–01–20 05:00:00	2005–01–20 06:00:00	2005–01–20 06:51:00	Y	$N_{P8'}$
70	2006–12–13 01:00:00	2006–12–13 02:00:00	2006–12–13 02:47:00	Y	
71	2012–05–17 00:00:00	2012–05–17 01:00:00	—	Y	

Table 6.1: List of GLE events that occurred since ACE was launched taken directly from the NMDB webpage. All the GLE events detected by the Neutron Monitor Network where also seen by the EPAM making them potential study subjects for future research. Events designated with note O occur during a period where they overlap with particles arriving from a previous event. This may make it impossible to successfully analyze this data for the purposes expressed in this chapter. Events designated with note $N_{P8'}$ don't show a statistically significant signal above the pre event in the higher energy channel P8'.

HISCALE data to look for GLE-like events that might have missed the Earth and are outside the ecliptic plane.

Until the present day, we have 16 GLE events that were detected both by the Neutron Monitor Network and the EPAM data (see table 6.1). All of these events are now candidates to go trough the process described mainly in Chapter 4. By doing so, we hope to get a greater insight into the origin of near relativistic ions of solar origin. The possible scientific interest of this work is twofold, we will be able to add some much needed statistics to our collection of GLE events' analysis and we will also be able to finally have a picture of GLE events that doesn't rely solely on data collected in the ecliptic plane.

Since there are no other GLE events in this solar cycle it was first tried to analyze the event from January 6th of 2014 that was seen by some NMS, but there was no response to GeV protons in EPAM proton channels. The January 6th of 2014 event was only seen at the high altitude NMS in South Pole and South Polar Bare which have a low effective cutoff rigidity of 300 MeV/nucleon but the event didn't have enough high energy protons to be detected in the out of nominal energy range (≈ 4 MeV) in LEMS120 detector.

Due to the low geometrical factor for the detection of out of nominal energy range protons that was discussed in Section 4.1 the most suitable candidates for this analysis are the GLE events that have an high number of counts in the GeV range and as such that can be seen in neutron monitor stations located at sea level. A prime candidate for using the analysis method proposed by this thesis is then the most massive GLE event that was detected since both ACE and Ulysses were first launched, the GLE 69 event that took place on January 20th of 2005.

6.1 GLE 69: January 20th of 2005

The 69th GLE event that took place on January 20th, 2005 was a massive event that was observed in several NMS attaining extremely high rates in several of them. The onset for the event at the NMS took place at 2005–01–20 06:51 UTC (Gopalswamy et al., 2005, 2012). GLE 69 was the second largest GLE event on record with up to 4200% count rate enhancement calculated at sea level.

The event — as seen in the NMS and in the vaster detector array of Spaceship Earth Network that supplements the NMS Network with other Neutron Monitor Detectors in order to increase the number of distinct asymptotic viewing directions —

is described in detail by Bieber et al. (2013). With special relevance for the analysis in this thesis, Bieber et al. (2013) notes the association of the GLE event with a very strong solar flare (location N14 W61, 1–8Å X-ray level X7.1 and onset 06:39 UT), an extreme anisotropy and an extremely fast rise from background to peak (6 minutes)

Figure 6.1 shows how massive this event was. The detection rates at the sea level station at Terre Adélie, Antarctica increased by nearly 4200%, the detection rates in South Pole reached a massive 5500% of the baseline at the peak of the event, although when corrected to sea level, the increase was “only” 2300% (Bieber et al., 2013).

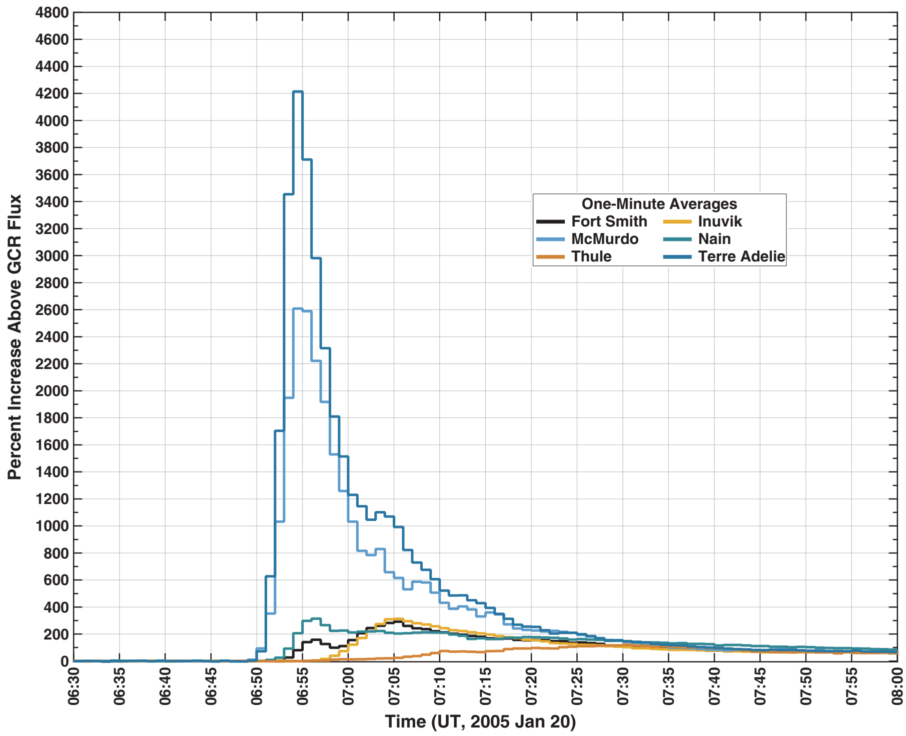

Figure 6.1: Percentage increases of relativistic solar ions above the Galactic cosmic ray (GCR) background for the giant GLE of 2005 January 20 at six polar, low-altitude neutron monitors, five of which belong to the global Spaceship Earth network. The two-pressure-coefficient procedure has been applied to normalize all stations to sea level. Because the neutron monitors view different directions in the sky, the major difference between the traces indicates an initially strong anisotropy in relativistic solar protons.
Source: Bieber et al. (2013)

On the EPAM we can see the simultaneous arrival of protons of various energies with a very steep rise in them, an indicator that we are indeed detecting high energy protons in the low energy ion channels of the LEMS120 telescope (figure 6.2). The event is also clearly seen in the electron channels of LEFS60 and other instruments onboard the ACE spacecraft.

Analysis of GLE 69 using EPAM data

We start by taking the data directly from the EPAM data repository, and removing the background using the interval from 05:40 to 06:40 UTC as the baseline for the rest of the event noting that the event raised almost 5 orders of magnitude over the pre event background in the P2' channel.

For this particular event, the count rates are so high that a small integration

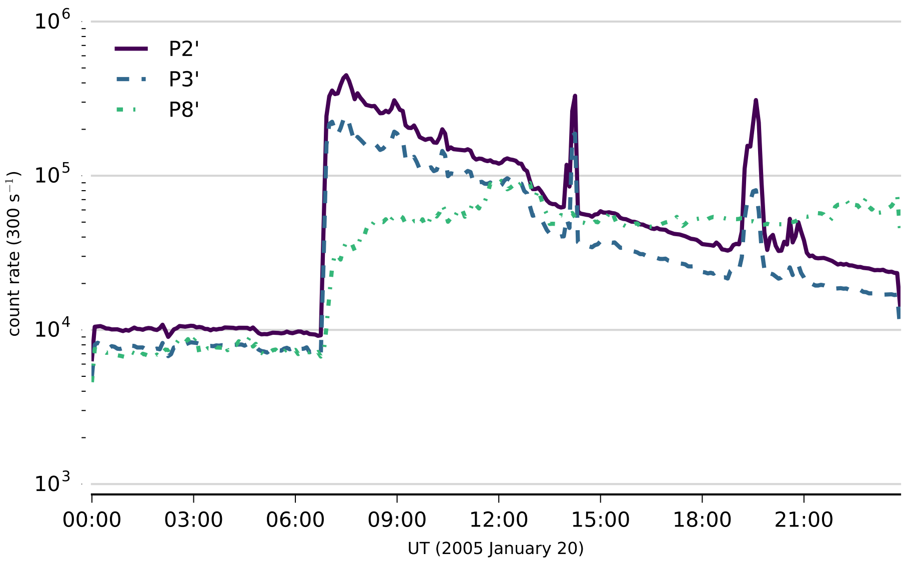

Figure 6.2: EPAM LEMS120 data for the full day of the 69th GLE event. The apparently simultaneous rise in P2', P3' and P8' is an indicator of detection of out of nominal energy protons. Also, readily apparent in the plot, we can see that although the event was massive the amount of background noise is so high that it is not possible to see the arrival of nominal energy protons in the P8' channel (≈ 4 MeV).

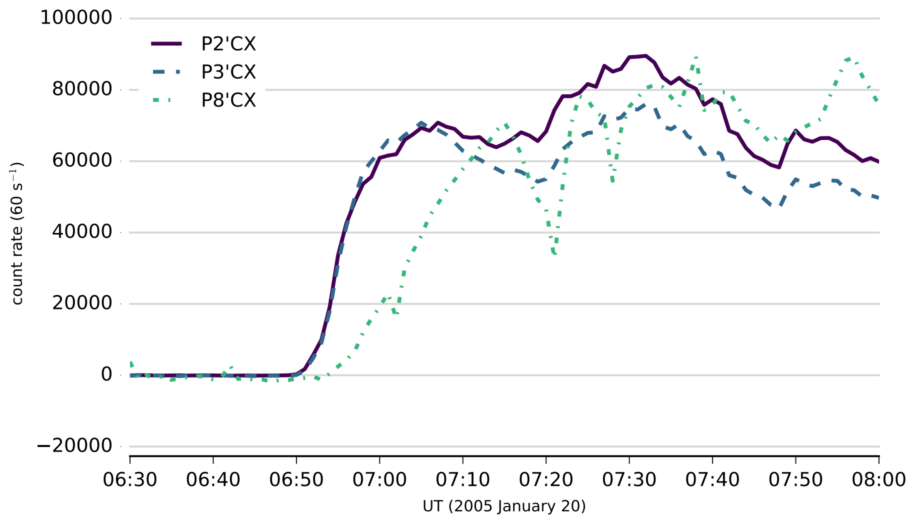

Figure 6.3: Counts over a 60 second integration window in the LEMS120. The C in the channel name denotes that the background rates were subtracted from the data and the X that the different channels were scaled to have the same counts at the peak.

time can be used and we can do without calculating the optimum integration time as explained in Subsection 4.4.1 and use a set 60 seconds integration for this analysis.

In figure 6.3 the channels rates were scaled so that they all reach the same peak counts showing the same striking behaviour already presented in Section 4.2. Once again we have the same simultaneous rise in channels P2' and P3' (that we know are more sensitive to higher energy penetrating ions) and a delayed rise in channel P8' (less sensitive to higher energy penetrating ions), again a very strong hint at the possibility that those counts in P2' and P3' are due to high energy protons. The scaling factor for P3' is 1.6 times that of P2', again exactly what was to be expected when observing the arrival of protons with energies exceeding 1 GeV (as detailed in Section 4.1).

As described in Section 4.2 another important aspect of the data that substantiates the arrival of high energy penetrating ions, is the angular response of the instrument that we can obtain from the PAD data that discriminates each sector.

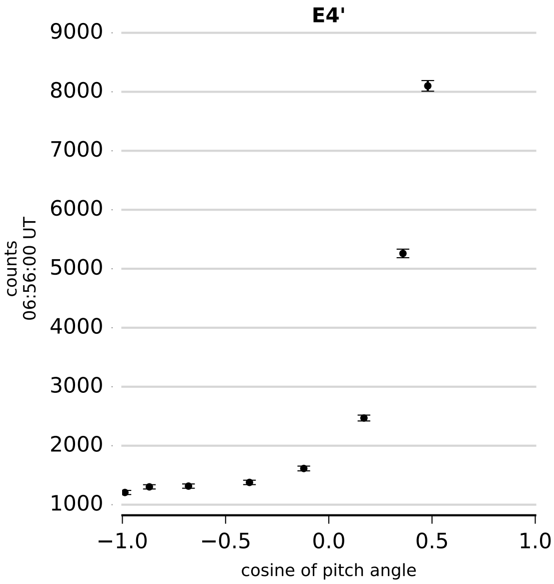

Figure 6.4: Pitch angle distribution for the event seen on the E4' channel in LEFS60 for electrons with energies about 300 keV showing a very beam-like pitch angle distribution. The counts were taken in a 2 minute integration interval immediately after the event threshold in the E4' channel.

As shown by Bieber et al. (2013) the onset for this event as seen in the various neutron monitors exhibits an extremely anisotropic behaviour. Something we can also observe in the electron channels of the LEFS60 detector onboard ACE presented in figure 6.4 that shows this same very markedly anisotropic behaviour in our data.

Now, as described in Section 4.2 we expect the curve of the pitch angle distribution for out of nominal range proton detection to be very different from the anisotropic behaviour seen in the neutron monitors or in the electron channels onboard the ACE. For out of nominal range protons the pitch angle distribution must be consistent with a curve with symmetry around the 0 cosine of pitch angle, with the characteristics discussed in Section 4.2 and as can be seen in figure 6.5 we have the same expected behaviour, even if without the data from LEMS30 — that was already nonoperational at the time of GLE 69 — it is not possible to fully reconstruct the pitch angle distribution curve of the event. Figure 6.5 (left) shows the expected behaviour in P2' with good statistics even when using a short interval for integration of out of nominal energy range protons. Figure 6.5 (right) shows that the response of P8' to out of

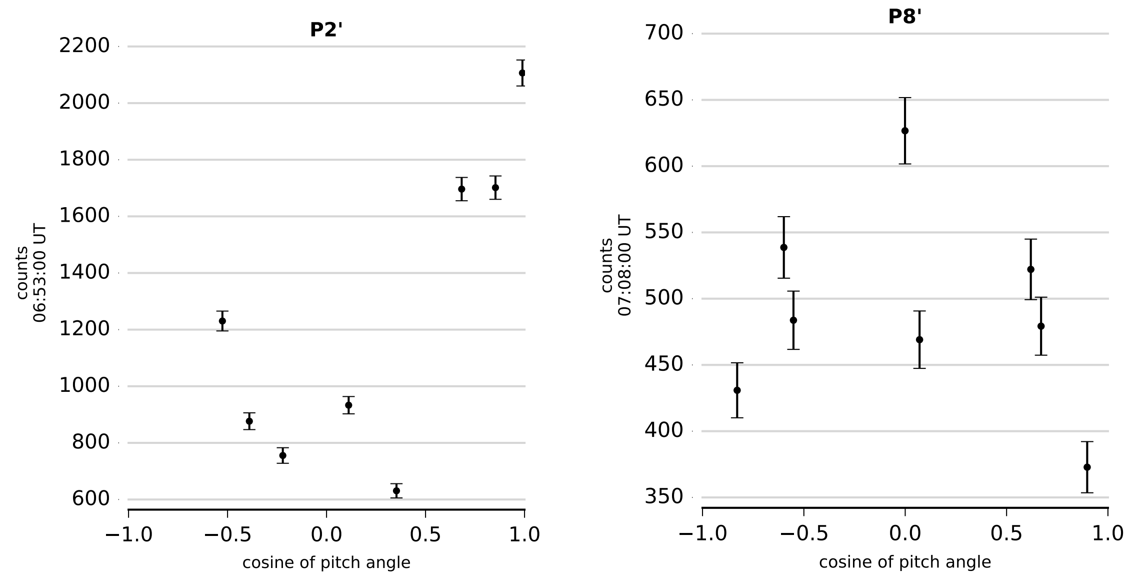

Figure 6.5: Pitch angle distribution for the event as seen in LEMS120 immediately after the event threshold in the respective channel showing a mirrored pitch angle distribution consistent with the early detection of out of nominal energy range protons. For P2' the counts were taken in a 2 minute integration interval while for P8' since the errors were much higher, a 10 minute integration interval had to be used.

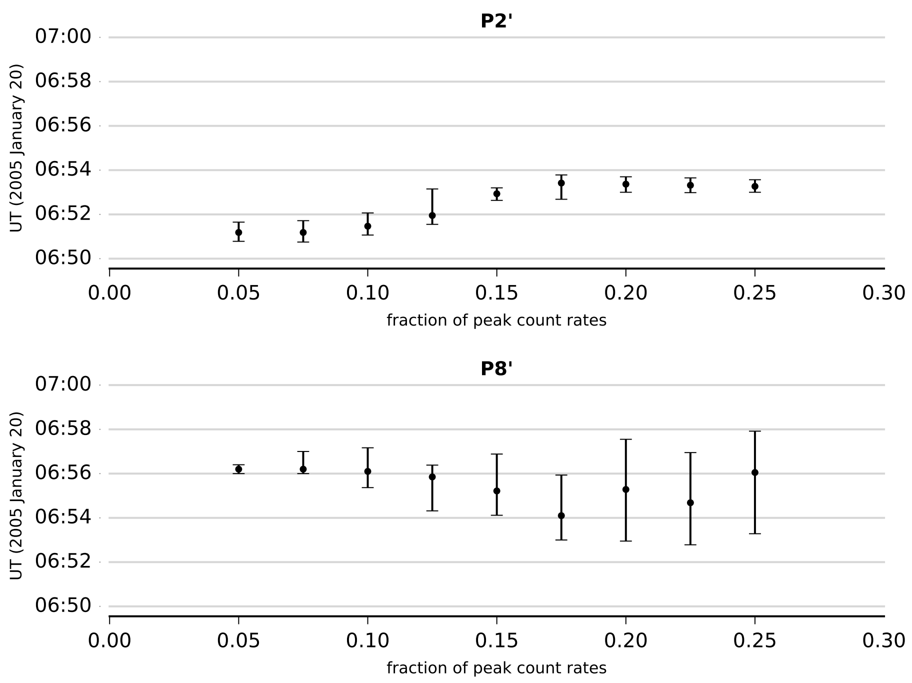

Figure 6.6: Onset times versus percentage of peak in LEMS120.

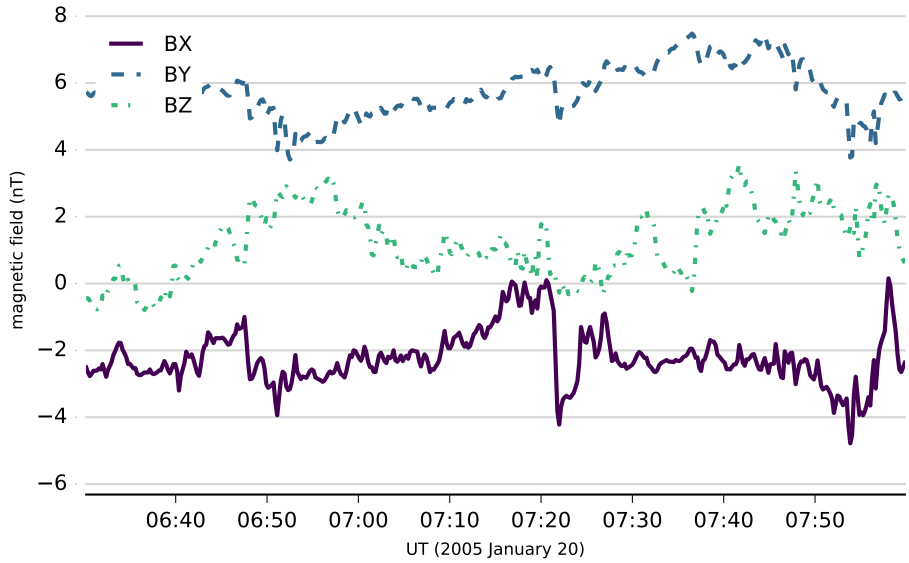

Figure 6.7: Magnetic field variation during the event. Although the magnetic field remains stable, the variation between negative and positive values along the X and Z axis can affect the rates for out of nominal energy range protons and be the explanation for the drops in the P8' channel during the event rise.

nominal energy range protons has — as explained in Section 4.1 and figure 4.3 — a much smaller geometrical factor and as such it can only be seen properly in really massive events like this one. When comparing to figure 4.6 we can see that figure 6.5 does indeed follows that same expected behaviour.

The onset times calculated for the event from the data are also in accordance with the values obtained by Gopalswamy et al. (2005) and the energies calculated by Bieber et al. (2013). The onset for channel P2' using 1 minute integration and a threshold above 4σ the background rate places the onset at 06:50 UTC (± 1 mn). The onset at P8' takes place at 06:56 UTC (± 2 mn).

Using a smaller integration time we can also see the progression of the onset times calculated as percentage of peak as presented in Subsection 4.4.2. For channel P2' figure 6.6 (top) shows a behaviour consistent with a linear rise and with remarkable

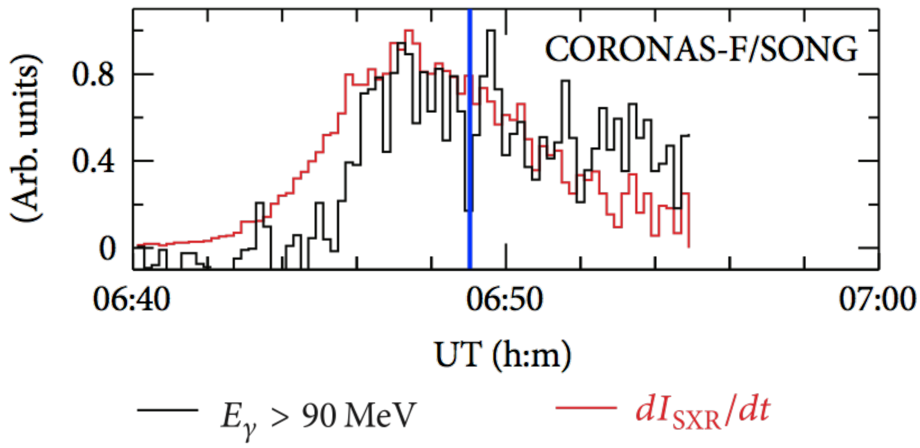

Figure 6.8: GLE 69, January 20, 2005. SONG gamma-rays (black curve) and the soft X-ray derivative (red curve). The horizontal blue line is the calculated arrival time at 1 AU for high energy protons of 1.5 GeV using the onset time of out of nominal channel energy range protons on the LEMS120 and the calculated path length traveled by charged particles for this event (6:49 UT with an uncertainty of about ± 1 mn).
Source: Kurt et al. (2013)

accordance with the onset in Gopalswamy et al. (2005) and energy values for the neutron monitor stations calculated by Bieber et al. (2013). For P8' figure 6.6 (bottom) shows a substantial increase in the error as the event progresses probably due to the drops in the channel P8' counts related to the variation of the magnetic field between negative and positive at the same time as the drops occur (figure 6.7).

Like referred at the beginning of this chapter and as can be seen in figure 6.2 it is not possible to see the arrival of protons in the nominal energy range in channel P8' (energy ≈ 4 MeV) due to the background of the event and as such we can't use P8' nominal response in order to further validate the inverse velocity curve as done in figure 4.15 for the analysis presented in Chapter 4. For GLE 69 we have a better way to validate the release time at the Sun using gamma ray and soft-X ray data from the SONG instrument onboard the CORONA-F satellite. Kurt et al. (2013) uses this data to calculate the onset of GLE events from high-energy gamma and neutron observations using the time profile of the soft X-ray derivative a a proxy of time behavior of the flare energy release. This profile differs by approximately 1 minute from the adjusted time of the detection of high energy protons with energies above 1.5 GeV on the LEMS120 (figure 6.8) calculated using the method presented in Chapter 4 and published in Morgado et al. (2015) which taking into account the constrains of LEMS120 in detecting out of nominal energy range protons with more that 1 GeV — something it was not originally designed to do — is an excellent result.

Bibliography

Bieber, J. W., Clem, J., Evenson, P., Pyle, R., Sáiz, A., and Ruffolo, D. (2013). Giant Ground Level Enhancement of Relativistic Solar Protons on 2005 January 20. I. Spaceship Earth Observations. *ApJ*, 771:92.

Gopalswamy, N., Xie, H., Yashiro, S., Akiyama, S., Mäkelä, P., and Usoskin, I. G. (2012). Properties of Ground Level Enhancement Events and the Associated Solar Eruptions During Solar Cycle 23. *Space Sci. Rev.*, 171:23–60.

Gopalswamy, N., Xie, H., Yashiro, S., and Usoskin, I. (2005). Coronal Mass Ejections and Ground Level Enhancements. *International Cosmic Ray Conference*, 1:169.

Kurt, V., Kudela, K., Yushkov, B., and Galkin, V. (2013). On the onset time of several spe/gle events: Indications from high-energy gamma-ray and neutron measurements by coronas-f. *Advances in Astronomy*, 2013.

Morgado, B., Filipe Maia, D. J., Lanzerotti, L., Gonçalves, P., and Patterson, J. D. (2015). The low energy magnetic spectrometer on Ulysses and ACE response to near relativistic protons. *A&A*, 577:A61.

Chapter 7

Conclusion

Contents

7.1 Discussion

By building and testing a virtual construct of the HISCALE/EPAM instruments in a Monte Carlo simulation system, it was possible to identify the spectral characteristics of spurious electrons and protons in the onset of SEP events by characterizing the response of the instrument under these conditions and with it, separate the spurious response from the nominal response of the instrument. It was then possible to use this added information to the in situ data collected by the instrument to better constrain release times back at the Sun for both electrons and protons.

On the electron side of the picture a method was developed that increases the timing accuracy for events with an high number of counts from high energy particles. In the 2012 May 17 GLE event, the method shown by Morgado and Maia (2014) allowed to obtain onset timings with a clearer trend in all the channels and with a lower uncertainty than the traditionally used methods. More so, the values calculated with this method are further validated by other detectors and also by onset timings calculated by Morgado et al. (2015) which provide an upper estimate for the onset time of the ions on the same event, being consistent with the ion analysis carried out by Gopalswamy et al. (2013); Li et al. (2013). There is a discrepancy with the electron onset times obtained by Li et al. (2013) for the event given as an example and published in the work for this thesis, but it should be noted that this discrepancy is also present with their own findings for ions, being inconsistent with the other data showing similar onset times for both ions and electrons and the fact that their timings agrees with an almost scatter free propagation of high energy particles which suggest that they are being accelerated and released by the same process.

On the proton side it was shown that it is possible to greatly extend the energy range of the instrument allowing much stronger confirmations of the onset timings. In the particular event shown by Morgado et al. (2015) the introduction of new "*spurious*" channels and their use in the calculation of the onset timings further validates the previously obtained results, being consistent with the Oulu monitor neutron data (Morgado et al., 2015), the GOES data (Maia and Morgado, 2014) and the previously mentioned works in the electron side of the story (Morgado and Maia, 2014). The onset times determined solely using the LEMS120 results gathered in this thesis work, can now greatly constrain the release times back at the Sun with great precision. In practice, the process developed effectively increases the energy range of P2' by 4 orders of magnitude, allowing us to detect energies of more than 1 GeV where before we could only accurately use energies only up to 100 keV. Presently no other instrument in orbit was originally built in order to measure such high energy protons and our best measurements for this energy range come from Neutron Monitor Stations which, like already discussed in Subsection 4.4.1, present several challenges when it comes to analyze the data obtained by them. This thesis work changes that picture allowing us access to data that is simpler to analyze with the added benefit of this data coming from an instrument that is completely outside Earth's magnetosphere influence.

Recently other authors have applied a similar method to other instruments in orbit. Kühl et al. (2015) discusses a similar method to the one presented in this thesis for the analysis of ion data using the Electron Proton Helium INstrument (EPHIN) on board SOHO. Kühl et al. (2015) also acknowledges the same challenges presented in this thesis when analyzing Neutron Monitor data, namely that data from a neutron monitor station is highly dependent both of the geographical location of a particular monitor site, of its altitude and — even more complex — of the atmospheric conditions at the site of each individual neutron monitor station occurring when the data is collected. Kühl et al. (2015) also takes the approach of using data from a radiation monitor in space — the EPHIN — to analyze GLE events, both as a less complicated source of GLE data, but also as a data source with an energy range that is very seldom possible to capture on Earth using neutron monitor stations. Kühl et al. (2015) follows a similar approach to the one presented in Chapter 4 for checking the energy range that can be used by EPHIN: starting with a full instrument simulation in Geant4; testing the response of the instrument for particles with energies much higher than those of the instrument nominal range; find consistent values for the energy deposited by those high energy particles on the detectors taking into account the anti-coincidence logic of the instrument; compare those measurements for a specific GLE event with the treated data from Neutron Monitor Stations. The findings are similar to the ones presented in Chapter 4 although the EPHIN poses technological challenges that are not present on the EPAM due to the fact that the electron monitors in EPHIN are also used as proton monitors meaning that unlike in the EPAM/Ulysses the electron data in EPHIN can't be totally accounted for when analyzing the proton side of the picture.

As long as the schematics for a given instrument are available, this method can be applied in other SST based instruments that rely on an anti coincidence logic between two or more silicon detectors and, preferably, that like Ulysses and ACE periodically rotate around an axis — in order to have PAD data. Applying the method itself, requires little modification beyond the construction of the virtual model of the instrument in a Monte Carlo particle simulation system such as Geant4. The specifics of the instrument must be analyzed on a case to case basis but it is expected that besides the corrections that must be made to the specific electronics of each instrument, the method will provide consistent results simply by building a virtual simulation of the instrument and carrying out the necessary simulations in order to measure the relevant quantities for the problem. The robustness of the method shouldn't be discarded since it allows to find consistent bias to the instrument response that could be otherwise disregarded. As an example it was shown in Section 3.3 the clear dependence of the Geometric Factor with energy for the electron channels on LEFS telescopes of the HISCALE/EPAM — first assumed as a constant quantity — but that the simulations showed to be a function of source energy — even without knowing first hand what caused that effect — which we could latter attribute to a slight angular deflection of electrons by the aluminized parylene foil, or the readings in the proton channels as reported in Section 3.4, coming from energies much higher than the channels nominal energy ranges, that were possible to determine with a sufficiently high degree of precision to use in the analysis of event properties.

7.2 On the construction of future instruments

Just like the bulk of this thesis, the future work proposed from its outcome follows two distinct paths. There is the purely scientific results we may get from going through Ulysses and ACE past data and by applying the data treatment methods shown and developed during this thesis work and there are the more technical proposals for new instruments that advise from the work carried out thought this thesis that allowed for a better understanding of the details involved in the construction of particle detectors for GeV energies protons that might influence the data gathered by silicon detectors during SEP events.

Throughout the analysis of the LEMS instrument presented in Chapter 4, the LEFS instrument presented in Chapter 4 and the EPEAD instrument presented in Chapter 5, a common issue arises in all of them: the instrument performance outside of nominal behavior due to particles entering from outside of the field of view of the detectors (Morgado et al., 2015; Maia and Morgado, 2014) and being detected by channels supposed to only detect particles with much lower energy than that of the particle.

From the results obtained, specifically when simulating the detectors that were part of EPAM (see Chapter 3) and also when analyzing the EPAM in situ data (see Chapter 4), is that the constrains imposed by present radiation detector technology make it impractical to put detectors in orbit that are capable of shielding high energy ions from reaching the detectors, on the other hand if we want to measure high energy GeV ions the direct approach that consists in having enough material in the detector so that is possible to fully absorb high energy ions and report their energy has identical constrains that make it very difficult to have this kind instrument in orbit. From the results presented in this thesis it became clear that we can use an alternative approach in order to study GeV energies ions: using a rotating set of two or more enclosed detectors we are able to obtain good statistic from high energy ions by the means of an anti-coincidence system. Basically we propose a system similar to the one used by the EPEAD detector onboard GOES that encases the detectors inside a dome, taking into account "*spurious*" counts of ions, but unlike in EPEAD we wouldn't be interested in fully absorbing the particle and instead we would have two or more detectors that would be thinner and wider than the ones used by the EPEAD. The reason we wouldn't be needing to fully absorb high energy ions, is that, since we can obtain a good estimate of their energy for the purpose of the timing of particle arrival calculations by using the method presented in Subsection 3.4.1 and in Section 4.1 — showing a clear signature for GeV ions, we could do away by using a considerably lighter detector or a detector that would have a considerably higher geometric factor according to our needs and mission specifications.

According to the mission at hand, different detector geometries could be used, but from the analysis and simulation done in Section 3.4 we can see that, although initially unintended for this purposes, the geometric configuration and the rotation axis of the LEMS detectors in EPAM/HISCALE already gives good results for this purpose. In this case a very simple modification would be to cover the LEMS detector in order to prevent low energy ions and electrons to reach that detector and to remove the rare earth magnets. This would allow to greatly diminish the background noise of the instrument, and prevent complications advising from the silicon layer degradation trough ion deposition as discussed in Section 3.2, in this scenario the LEFS detector could remain open if the instrument was also intended to detect electrons. All in all, the design could accommodate the needs of the mission as long as it maintains the basic principles described in the previous paragraph.

Bibliography

Gopalswamy, N., Xie, H., Akiyama, S., Yashiro, S., Usoskin, I., and Davila, J. (2013). The first ground level enhancement event of solar cycle 24: Direct observation of shock formation and particle release heights. *The Astrophysical Journal Letters*, 765(2):L30.

Kühl, P., Banjac, S., Dresing, N., Goméz-Herrero, R., Heber, B., Klassen, A., and Terasa, C. (2015). Proton intensity spectra during the solar energetic particle events of May 17, 2012 and January 6, 2014. *A&A*, 576:A120.

Li, C., Firoz, K. A., Sun, L., and Miroshnichenko, L. (2013). Electron and proton acceleration during the first ground level enhancement event of solar cycle 24. *The Astrophysical Journal*, 770(1):34.

Maia, D. and Morgado, B. (2014). Timing of the 2012 may 17 gle using goes13 epead data. *Astronomy and Astrophysics, in press.*

Morgado, B., Filipe Maia, D. J., Lanzerotti, L., Gonçalves, P., and Patterson, J. D. (2015). The low energy magnetic spectrometer on Ulysses and ACE response to near relativistic protons. *A&A*, 577:A61.

Morgado, B. and Maia, D. (2014). Electron scattering profile of the epam experiment on ace. analysis of the electron event associated with the 2012 may 17 gle. *Astronomy and Astrophysics, in press.*

Bibliography

Ackermann, M., Ajello, M., Albert, A., Allafort, A., Baldini, L., Barbiellini, G., Bastieri, D., Bechtol, K., Bellazzini, R., Bissaldi, E., et al. (2014). High-energy gamma-ray emission from solar flares: Summary of fermi large area telescope detections and analysis of two m-class flares. *The Astrophysical Journal*, 787(1):15.

Agostinelli, S., Allison, J., Amako, K. e., Apostolakis, J., Araujo, H., Arce, P., Asai, M., Axen, D., Banerjee, S., Barrand, G., et al. (2003). Geant4—a simulation toolkit. *Nuclear instruments and methods in physics research section A: Accelerators, Spectrometers, Detectors and Associated Equipment*, 506(3):250–303.

Allison, J., Amako, K., Apostolakis, J., Araujo, H., Dubois, P. A., Asai, M., Barrand, G., Capra, R., Chauvie, S., Chytracek, R., et al. (2006). Geant4 developments and applications. *Nuclear Science, IEEE Transactions on*, 53(1):270–278.

Armstrong, T. and Hunt-Ward, T. (1999). Ulysses hiscale data analysis handbook, internal document. *Fundamental Technologies*.

Atwood, W., Abdo, A. A., Ackermann, M., Althouse, W., Anderson, B., Axelsson, M., Baldini, L., Ballet, J., Band, D., Barbiellini, G., et al. (2009). The large area telescope on the fermi gamma-ray space telescope mission. *The Astrophysical Journal*, 697(2):1071.

Balogh, A., Gosling, J. T., Jokipii, J. R., Kallenbach, R., and Kunow, H. (1999). Introduction. *Space Sci. Rev.*, 89:1–3.

Barlow, W. (1849). On the spontaneous electrical currents observed in the wires of the electric telegraph. *Philosophical Transactions of the Royal Society of London*, 139:61–72.

Bieber, J. W., Clem, J., Evenson, P., Pyle, R., Sáiz, A., and Ruffolo, D. (2013). Giant Ground Level Enhancement of Relativistic Solar Protons on 2005 January 20. I. Spaceship Earth Observations. *ApJ*, 771:92.

Bieber, J. W., Evenson, P., Pyle, R., Ruffolo, D., Rujiwarodom, M., Tooprakai, P., Khumlumlert, T., et al. (2004). Spaceship earth observations of the easter 2001 solar particle event. *The Astrophysical Journal Letters*, 601(1):L103.

Brueckner, G. E., Howard, R. A., Koomen, M. J., Korendyke, C. M., Michels, D. J., Moses, J. D., Socker, D. G., Dere, K. P., Lamy, P. L., Llebaria, A., Bout, M. V., Schwenn, R., Simnett, G. M., Bedford, D. K., and Eyles, C. J. (1995). The Large Angle Spectroscopic Coronagraph (LASCO). *Sol. Phys.*, 162:357–402.

Burlaga, L. F., Ness, N. F., Gurnett, D. A., and Kurth, W. S. (2013). Evidence for a Shock in Interstellar Plasma: Voyager 1. *ApJ*, 778:L3.

Cane, H. V., McGuire, R. E., and von Rosenvinge, T. T. (1986). Two classes of solar energetic particle events associated with impulsive and long-duration soft X-ray flares. *ApJ*, 301:448–459.

Carrington, R. C. (1863). *Observations of the spots on the sun: from November 9, 1853, to March 24, 1861, made at Redhill.* Williams and Norgate.

Cliver, E. W. (1996). Solar flare gamma-ray emission and energetic particles in space. In Ramaty, R., Mandzhavidze, N., and Hua, X.-M., editors, *American Institute of Physics Conference Series*, volume 374 of *American Institute of Physics Conference Series*, pages 45–60.

Cliver, E. W., Webb, D. F., and Howard, R. A. (1999). On the origin of solar metric type II bursts. *Sol. Phys.*, 187:89–114.

Domingo, V., Fleck, B., and Poland, A. I. (1995). The SOHO Mission: an Overview. *Sol. Phys.*, 162:1–37.

Dröge, W. (2003). Acceleration and propagation of solar energetic particles. In *Energy Conversion and Particle Acceleration in the Solar Corona*, pages 193–212. Springer.

Dungey, J. W. (1953). The motion of magnetic fields. *MNRAS*, 113:679+.

Dungey, J. W. (1958). The neutral point discharge theory of solar flares. a reply to cowling's criticism. In *IAU Symp. 6: Electromagnetic Phenomena in Cosmical Physics*, volume 6, pages 135+.

Gold, R., Krimigis, S., Hawkins III, S., Haggerty, D., Lohr, D., Fiore, E., Armstrong, T., Holland, G., and Lanzerotti, L. (1998). Electron, proton, and alpha monitor on the advanced composition explorer spacecraft. *Space Science Reviews*, 86(1-4):541–562.

Goldman, M. V. (1983). Progress and problems in the theory of type III solar radio emission. *Sol. Phys.*, 89:403–442.

Gopalswamy, N., Xie, H., Akiyama, S., Yashiro, S., Usoskin, I., and Davila, J. (2013). The first ground level enhancement event of solar cycle 24: Direct observation of shock formation and particle release heights. *The Astrophysical Journal Letters*, 765(2):L30.

Gopalswamy, N., Xie, H., Yashiro, S., Akiyama, S., Mäkelä, P., and Usoskin, I. G. (2012). Properties of Ground Level Enhancement Events and the Associated Solar Eruptions During Solar Cycle 23. *Space Sci. Rev.*, 171:23–60.

Gopalswamy, N., Xie, H., Yashiro, S., and Usoskin, I. (2005). Coronal Mass Ejections and Ground Level Enhancements. *International Cosmic Ray Conference*, 1:169.

Gopalswamy, N., Yashiro, S., and Akiyama, S. (2007). Geoeffectiveness of halo coronal mass ejections. *Journal of Geophysical Research (Space Physics)*, 112:A06112.

Gopalswamy, N., Yashiro, S., Krucker, S., Stenborg, G., and Howard, R. A. (2004). Intensity variation of large solar energetic particle events associated with coronal mass ejections. *Journal of Geophysical Research (Space Physics)*, 109:A12105.

Gopalswamy, N., Yashiro, S., Lara, A., Kaiser, M. L., Thompson, B. J., Gallagher, P. T., and Howard, R. A. (2003). Large solar energetic particle events of cycle 23: A global view. *Geophys. Res. Lett.*, 30:8015.

Gopalswamy, N., Yashiro, S., Xie, H., Akiyama, S., and Mäkelä, P. (2015). Properties and geoeffectiveness of magnetic clouds during solar cycles 23 and 24. *Journal of Geophysical Research (Space Physics)*, 120:9221–9245.

Gosling, J. T. (1993). The solar flare myth. *J. Geophys. Res.*, 98:18937–18950.

Gringauz, K. I., Kurt, V. G., Moroz, V. I., and Shklovskii, I. S. (1961). Results of Observations of Charged Particles Observed Out to R = 100, 000 km, with the Aid of Charged-Particle Traps on Soviet Space Rockets. *Soviet Ast.*, 4:680.

Haggerty, D. and Roelof, E. (2003). Electron scattering in solid state detectors: Geant 4 simulations. *Advances in Space Research*, 32(3):423–428.

Haggerty, D., Roelof, E., Ho, G., and Gold, R. (2006). Qualitative comparison of ace/epam data from different detector heads: Implications for noaa rtsw users. *Advances in Space Research*, 38(5):995–1000.

Haggerty, D. K. and Roelof, E. C. (2006). Effectiveness of anti-coincidence in electron detectors: Implications for beam-like electron events. *Advances in Space Research*, 38(5):990–994.

Hanser, F. (2011). Eps/hepad calibration and data handbook. Technical report, Tech. Rep. GOESN-ENG-048D.

Hassler, D. M., Zeitlin, C., Wimmer-Schweingruber, R. F., Ehresmann, B., Rafkin, S., Eigenbrode, J. L., Brinza, D. E., Weigle, G., Böttcher, S., Böhm, E., and et al. (2014). Mars' Surface Radiation Environment Measured with the Mars Science Laboratory's Curiosity Rover. *Science*, 343:1244797.

Klein, K.-L., Masson, S., Bouratzis, C., Grechnev, V., Hillaris, A., and Preka-Papadema, P. (2014). The relativistic solar particle event of 2005 january 20: origin of delayed particle acceleration. *Astronomy & Astrophysics*, 572:A4.

Kocharov, L., Vainio, R., Kovaltsov, G., and Torsti, J. (1998). Adiabatic deceleration of solar energetic particles as deduced from monte carlo simulations of interplanetary transport. *Solar Physics*, 182(1):195–215.

Kühl, P., Banjac, S., Dresing, N., Goméz-Herrero, R., Heber, B., Klassen, A., and Terasa, C. (2015). Proton intensity spectra during the solar energetic particle events of May 17, 2012 and January 6, 2014. *A&A*, 576:A120.

Kurt, V., Kudela, K., Yushkov, B., and Galkin, V. (2013). On the onset time of several spe/gle events: Indications from high-energy gamma-ray and neutron measurements by coronas-f. *Advances in Astronomy*, 2013.

Kurt, V., Yushkov, B., Belov, A., Chertok, I., and Grechnev, V. (2013). Determination of Acceleration Time of Protons Responsible for the GLE Onset. *Journal of Physics Conference Series*, 409(1):012151.

Lanzerotti, L., Gold, R., Anderson, K., Armstrong, T., Lin, R., Krimigis, S., Pick, M., Roelof, E., Sarris, E., and Simnett, G. (1992). Heliosphere instrument for spectra, composition and anisotropy at low energies. *Astronomy and Astrophysics Supplement Series*, 92:349–363.

Lanzerotti, L. J. (2001). Space weather effects on communications. In *Space storms and space weather hazards*, pages 313–334. Springer.

Lara, A., Gopalswamy, N., Caballero-López, R. A., Yashiro, S., Xie, H., and Valdés-Galicia, J. F. (2005). Coronal Mass Ejections and Galactic Cosmic-Ray Modulation. *ApJ*, 625:441–450.

Li, C., Firoz, K. A., Sun, L., and Miroshnichenko, L. (2013). Electron and proton acceleration during the first ground level enhancement event of solar cycle 24. *The Astrophysical Journal*, 770(1):34.

Lindström, G. (2003). Radiation damage in silicon detectors. *Nuclear Instruments and Methods in Physics Research Section A: Accelerators, Spectrometers, Detectors and Associated Equipment*, 512(1):30–43.

Maia, D., Aulanier, G., Wang, S. J., Pick, M., Malherbe, J.-M., and Delaboudinière, J.-P. (2003). Interpretation of a complex CME event: Coupling of scales in multiple flux systems. *A&A*, 405:313–323.

Maia, D. and Morgado, B. (2014). Timing of the 2012 may 17 gle using goes13 epead data. *Astronomy and Astrophysics, in press.*

Maia, D., Vourlidas, A., Pick, M., Howard, R., Schwenn, R., and Magalhães, A. (1999). Radio signatures of a fast coronal mass ejection development on November 6, 1997. *J. Geophys. Res.*, 104:12507–12514.

Maia, D. J. F., Gama, R., Mercier, C., Pick, M., Kerdraon, A., and Karlickỳ, M. (2007). The radio-coronal mass ejection event on 2001 april 15. *The Astrophysical Journal*, 660(1):874.

Mason, G., Mazur, J., and Dwyer, J. (1999). 3he enhancements in large solar energetic particle events. *The Astrophysical Journal Letters*, 525(2):L133.

Mazur, J., Mason, G., Looper, M., Leske, R., and Mewaldt, R. (1999). Charge states of solar energetic particles using the geomagnetic cutoff technique: Sampex measurements in the 6 november 1997 solar particle event. *Geophysical research letters*, 26(2):173–176.

McKenna-Lawlor, S., Gonçalves, P., Keating, A., Reitz, G., and Matthiä, D. (2012). Overview of energetic particle hazards during prospective manned missions to Mars. *Planet. Space Sci.*, 63:123–132.

Mel'Nik, V. N. and Kontar, E. P. (2003). Plasma Radio Emission of Beam-Plasma Structures in the Solar Corona. *Sol. Phys.*, 215:335–341.

Melrose, D. B. (1980). *Plasma astrohysics. Nonthermal processes in diffuse magnetized plasmas - Vol.1: The emission, absorption and transfer of waves in plasmas; Vol.2: Astrophysical applications.*

Mewaldt, R., Cohen, C., Haggerty, D., Gold, R., Krimigis, S., Leske, R., Ogliore, R., Roelof, E., Stone, E., von Rosenvinge, T., et al. (2003). Heavy ion and electron release times in solar particle events. In *International Cosmic Ray Conference*, volume 6, page 3313.

Mishev, A., Kocharov, L., and Usoskin, I. (2014). Analysis of the ground level enhancement on 17 may 2012 using data from the global neutron monitor network. *Journal of Geophysical Research: Space Physics*, 119(2):670–679.

Möbius, E., Popecki, M., Klecker, B., Kistler, L., Bogdanov, A., Galvin, A., Heirtzler, D., Hovestadt, D., Lund, E., Morris, D., et al. (1999). Energy dependence of the ionic charge state distribution during the november 1997 solar energetic particle event. *Geophysical research letters*, 26(2):145–148.

Moebius, E. (1999). Variation of ionic charge states between solar energetic particle events as observed with ace sepica. In *International Cosmic Ray Conference*, volume 6, page 87.

Morgado, B., Filipe Maia, D. J., Lanzerotti, L., Gonçalves, P., and Patterson, J. D. (2015). The low energy magnetic spectrometer on Ulysses and ACE response to near relativistic protons. *A&A*, 577:A61.

Morgado, B. and Maia, D. (2014). Electron scattering profile of the epam experiment on ace. analysis of the electron event associated with the 2012 may 17 gle. *Astronomy and Astrophysics, in press.*

Nikitin, A. V., Davidchack, R. L., and Armstrong, T. P. (1997). Many-fold coincidence pileup in silicon detectors: Solar x-ray response of charged particle detector systems for space. *Nuclear Instruments and Methods in Physics Research Section A: Accelerators, Spectrometers, Detectors and Associated Equipment*, 386(2):431–438.

Onsager, T., Grubb, R., Kunches, J., Matheson, L., Speich, D., Zwickl, R. W., and Sauer, H. (1996). Operational uses of the goes energetic particle detectors. In *SPIE's 1996 International Symposium on Optical Science, Engineering, and Instrumentation*, pages 281–290. International Society for Optics and Photonics.

Parker, E. N. (1958). Dynamics of the Interplanetary Gas and Magnetic Fields. *Astrophysical Journal*, 128:664.

Parker, E. N. (1965). The passage of energetic charged particles through interplanetary space. *Planetary and Space Science*, 13(1):9–49.

Patterson, J. D. (2002). *An analysis of solar energetic particles throughout the inner heliosphere*. PhD thesis, UNIVERSITY OF KANSAS.

Peltola, T. (2014). Charge collection efficiency simulations of irradiated silicon strip detectors. *Journal of Instrumentation*, 9(12):C12010.

Pick, M., Forbes, T. G., Mann, G., Cane, H. V., Chen, J., Ciaravella, A., Cremades, H., Howard, R. A., Hudson, H. S., Klassen, A., Klein, K. L., Lee, M. A., Linker, J. A., Maia, D., Mikic, Z., Raymond, J. C., Reiner, M. J., Simnett, G. M., Srivastava, N., Tripathi, D., Vainio, R., Vourlidas, A., Zhang, J., Zurbuchen, T. H., Sheeley, N. R., and Marqué, C. (2006). Multi-Wavelength Observations of CMEs and Associated Phenomena. Report of Working Group F. *Space Sci. Rev.*, 123:341–382.

Pohjolainen, S., Maia, D., Pick, M., Vilmer, N., Khan, J. I., Otruba, W., Warmuth, A., Benz, A., Alissandrakis, C., and Thompson, B. J. (2001). On-the-Disk Development of the Halo Coronal Mass Ejection on 1998 May 2. *ApJ*, 556:421–431.

Priest, E. R. (1982). *Solar magneto-hydrodynamics*. Dordrecht, Holland ; Boston : D. Reidel Pub. Co. ; Hingham,.

Reames, D. V. (1993). Non-thermal particles in the interplanetary medium. *Advances in Space Research*, 13:331–339.

Reames, D. V. (1999). Particle acceleration at the Sun and in the heliosphere. *Space Sci. Rev.*, 90:413–491.

Reames, D. V. (2002). Solar energetic particles. *Adv. Sp. Res.*

Reames, D. V., Meyer, J., and Von Rosenvinge, T. (1994). Energetic-particle abundances in impulsive solar flare events. *The Astrophysical Journal Supplement Series*, 90:649–667.

Reiner, M. J. and Kaiser, M. L. (1999). High-frequency type ii radio emissions associated with shocks driven by coronal mass ejections. *J. Geophys. Res.*, 104:16979–16992.

Roelof, E. (1969). Propagation of solar cosmic rays in the interplanetary magnetic field. In *Lectures in High-Energy Astrophysics*, volume 1, page 111.

Ruffolo, D. (1994). Effect of adiabatic deceleration on the focused transport of solar cosmic rays. *arXiv preprint astro-ph/9408056*.

Ryan, J. M., Lockwood, J. A., and Debrunner, H. (2000). Solar energetic particles. *Space Science Reviews*, 93(1-2):35–53.

Sáiz, A., Evenson, P., Ruffolo, D., and Bieber, J. W. (2005). On the estimation of solar energetic particle injection timing from onset times near earth. *The Astrophysical Journal*, 626(2):1131.

Sandberg, I., Jiggens, P., Heynderickx, D., and Daglis, I. (2014). Cross calibration of noaa goes solar proton detectors using corrected nasa imp-8/gme data. *Geophysical Research Letters*, 41(13):4435–4441.

Schwabe, M. (1843). Die Sonne. Von Herrn Hofrath Schwabe. *Astronomische Nachrichten*, 20:283.

Schwenn, R., Raymond, J. C., Alexander, D., Ciaravella, A., Gopalswamy, N., Howard, R., Hudson, H., Kaufmann, P., Klassen, A., Maia, D., Munoz-Martinez, G., Pick, M., Reiner, M., Srivastava, N., Tripathi, D., Vourlidas, A., Wang, Y.-M., and Zhang, J. (2006). Coronal Observations of CMEs. Report of Working Group A. *Space Sci. Rev.*, 123:127–176.

Sellers, F. B. and Hanser, F. A. (1996). Design and calibration of the goes-8 particle sensors: the eps and hepad. In *SPIE's 1996 International Symposium on Optical Science, Engineering, and Instrumentation*, pages 353–364. International Society for Optics and Photonics.

Shen, C., Li, G., Kong, X., Hu, J., Sun, X., Ding, L., Chen, Y., Wang, Y., and Xia, L. (2013). Compound twin coronal mass ejections in the 2012 may 17 gle event. *The Astrophysical Journal*, 763(2):114.

Sturrock, P. A. (1964). Type III Solar Radio Bursts. *NASA Special Publication*, 50:357.

Sullivan, J. (1972). Erratum: Geometrical factor and directional response of single and multi-element particle telescopes, nucl. instr. and meth. 95 (1971) 5-11. *Nuclear Instruments and Methods*, 98:187.

Tan, L. C., Malandraki, O. E., Reames, D. V., Ng, C. K., Wang, L., Patsou, I., and Papaioannou, A. (2013). Comparison between path lengths traveled by solar electrons and ions in ground-level enhancement events. *The Astrophysical Journal*, 768(1):68.

Tousey, R., Bartoe, J. D. F., Bohlin, J. D., Brueckner, G. E., Purcell, J. D., Scherrer, V. E., Sheeley, N. R., Schumacher, R. J., and Vanhoosier, M. E. (1973). A preliminary study of the extreme ultraviolet spectroheliograms from skylab. *Sol. Phys.*, 33:265+.

Tsurutani, B. T., Gonzalez, W. D., Gonzalez, A. L. C., Guarnieri, F. L., Gopalswamy, N., Grande, M., Kamide, Y., Kasahara, Y., Lu, G., Mann, I., McPherron, R., Soraas, F., and Vasyliunas, V. (2006). Corotating solar wind streams and recurrent geomagnetic activity: A review. *Journal of Geophysical Research (Space Physics)*, 111:A07S01.

Vilmer, N. (2012). Solar flares and energetic particles. *Philosophical Transactions of the Royal Society of London Series A*, 370:3241–3268.

Vourlidas, A., Wu, S. T., Wang, A. H., Subramanian, P., and Howard, R. A. (2003). Direct Detection of a Coronal Mass Ejection-Associated Shock in Large Angle and Spectrometric Coronagraph Experiment White-Light Images. *ApJ*, 598:1392–1402.

Wenzel, K., Marsden, R., Page, D., and Smith, E. (1992). The ulysses mission. *Astronomy and Astrophysics Supplement Series*, 92:207.

Wild, J. P. and McCready, L. L. (1950). Observations of the Spectrum of High-Intensity Solar Radiation at Metre Wavelengths. I. The Apparatus and Spectral Types of Solar Burst Observed. *Australian Journal of Scientific Research A Physical Sciences*, 3:387.

Wüest, M., Evans, D. S., and von Steiger, R. (2007). *Calibration of particle instruments in space physics*. ISSI, The International Space Science Institute.